Analysis of the potential for coded excitation to improve the detection of tissue and blood motion in medical ultrasound.

Benjamin Lamboul

A thesis submitted for the degree of Doctor of Philosophy.
The University of Edinburgh.
November 2008

Abstract

Doppler ultrasound imaging modalities arguably represent one of the most complex task performed (usually in real time) by ultrasound scanners. At the heart of these techniques lies the ability to detect and estimate soft tissues or blood motion within the human body. As they have become an invaluable tool in a wide range of clinical applications, these techniques have fostered an intensive effort of research in the field of signal processing for more than thirty years, with a push towards more accurate velocity or displacement estimation. Coded excitation has recently received a growing interest in the medical ultrasound community. The use of these techniques, originally developed in the radar field, makes it possible to increase the depth of penetration in B-mode imaging, while complying with safety standards. These standards impose strict limits on the peak acoustic intensity which can be transmitted into the body. Similar solutions were proposed in the early developments of Doppler flow-meters to improve the resolution / sensitivity trade-off from which typical pulsed Doppler systems suffer.

This work discusses the potential improvements in resolution, sensitivity and accuracy achievable in the context of modern Doppler ultrasound imaging modalities (taken in its broadest sense, that is, all the techniques involving the estimation of displacements, or velocities). A theoretical framework is provided for discussing this potential improvements, along with simulations for a more quantitative assessment. Colour Flow Imaging (CFI) modalities are taken as the main reference technique for discussion, due to their historical importance, and their relevance in many clinical applications. The potential achievable improvement in accuracy is studied in the context of modern velocity estimation strategies, which can be broadly classified into narrowband estimators (such as the “Kasai” estimator still widely used in CFI) and time shift based wideband strategies (normalised crosscorrelation estimator used, for instance, in applications like strain or strain rate estimation, elastography, etc.). Finally, simulations and theoretical results are compared to experimental data obtained with a simple custom-designed experimental set-up, using a single-element transducer.

Declaration of originality

I hereby declare that the research recorded in this thesis and the thesis itself was composed and originated entirely by myself in the Department of Medical Physics at The University of Edinburgh.

Benjamin Lamboul

Acknowledgements

I should first thank Norman McDicken and Tom Anderson for giving me the opportunity to do this PhD in Medical Physics at Edinburgh University, and acknowledge EPSRC for funding this work and giving the opportunity to foreign students to do their PhD in the UK.

I want to thank my supervisors, Norman McDicken and Michael Bennett for their constant enthusiasm about my project, for reviewing this work, and especially, for Michael, for dealing with my “epic negativity” during three long years!

I want to thank my mentor Tom McGillivray, for his attentive ear and for his encouragements.

I want to thank Tom Anderson for his kindness, and for his precious help and patience during my different attempts to design a rotating phantom.

I want to thank Robin Steel for his thorough reviews, honest scientific criticisms, and his always stimulating inputs on many problems, these made me learn a lot!

I want to thank Leonidas Koutsompos for helping me going through the hard times with some Greek cuisine and Woody Allen movies... and for being the best flatmate ever!

I want to thank Panos and Susana, for playing music with me, and for having them as friends.

I want to thank all the people of Medical Physics, with, in particular, James (...for being James Blake!), Mairead (for always being around and for hosting me during one week when I arrived in Edinburgh!), the usual Friday pint crew (Antonios, Dave H. and Dave T., Padraig), Norman (again, for the nice Burn supper nights), Irene (for her help on the administrative side, and for asking if we are all “happy bunnies”), Vassilis (for his kindness, and for organising Firbush every time!) and Gavin (for his brave attempts to speak French to me!).

I also want to thank Gabriella for her smile everyday when I was taking a latte from downstairs!

I want to thank all the people who also contributed to make my scottish experience unforgettable (apologies, as I will inevitably forget some people): Marie, Maryse, mon bon vieux Sam, Hugo, Monica, Barbara, Inma, the two Yorgos, Susana and Jon, Katherine, Kate and Chris, Marta, Yue, Katherina, Natassa, Lucile , Maro, Ioana, Dave F....

Contents

List of figures

List of tables

Acronyms and abbreviations

AWG	Arbitrary Waveform Generator
CF	Continuous Frequency
CFI	Colour Flow Imaging
CW	Continuous Wave
DR	Dynamic Range
DTI	Doppler Tissue Imaging
FWHM	Full Width at Half Maximum
GSNR	Gain in Signal-to-Noise Ratio
I/Q	In-phase and Quadrature signal components
MI	Mechanical Index
NXC	Normalised crosscorrelation
PRF	Pulse Repetition Frequency
PRP	Pulse Repetion Period
PW	Pulsed Wave
PSD	Power Spectral Density
RF	Radio-Frequency
SAD	Sum of Absolute Differences
SNR	Signal-To-Noise Ratio
SSD	Sum of Squared Differences

Main nomenclature

A	Signal amplitude
B	Bandwidth [Hz]
B_{conv}	Bandwidth of the conventional pulse [Hz]
B_{coded}	Bandwidth of the coded pulse [Hz]
B_D	Doppler bandwith [Hz]
B_f	Fractional bandwidth [Hz]
BW	Lateral beam width
c	Speed of sound in the propagating medium [m.s^{-1}]
e	Excitation signal
E	Energy of a signal
f	Frequency [Hz]
f_D	Doppler shift [Hz]
f_0	Centre frequency [Hz]
h	Linear filter impulse response
h_{trans}	Transducer impulse response
$H(f)$	Filter frequency response
I	In-phase component of quadrature amplitude demodulated signals
N	Noise power [W]
N_0	Noise power spectral density [W/Hz]
N_b	Number of bits of the Barker code
N_p	Packet size
Q	Quadrature component of quadrature amplitude demodulated signals
r	Received signal
s	Transmitted signal
$S(f)$	Fourier transform of the transmitted signal
S	Signal power [W]
$R(\tau)$	Crosscorrelation function of two signals
$P(f)$	Power spectral density

t	Time instant or time variable
t_s	Sampling period (fast time signal)
T_p	Pulse duration
T_s	Pulse repetition period (PRP) or slow time signal sampling period
v	Axial velocity of scatterers
z	Depth of return of signals
$\underline{Z}$	Complex baseband signals

β	Attenuation in [dB.$\mathrm{cm}^{-1}\mathrm{Mhz}^{-1}$]
δ	Axial displacement of scatterers
Δt	Time shift
ϕ	Phase shift
λ	Wavelength of the ultrasonic wave
ρ	Correlation coefficient
θ	Angle between the trajectory of scatterers and axis of the transducer
τ	Time delay
ω	Angular frequency
ω_0	Centre angular frequency of an ultrasonic pulse

Chapter 1
Introduction

This introduction chapter presents all the background notions necessary to understand this PhD work and highlights the objectives of this thesis in the context of current research. The first section starts with a very general description of Doppler medical applications and then focuses on signal processing techniques of velocity / displacement estimation. The second section introduces the basic concepts of coded excitation techniques with illustrated examples, and briefly discusses its use in the context of medical ultrasound applications. Finally, the last section of this chapter introduces more in detail this PhD work, with the objectives, approaches used, and the overall structure of the thesis.

1.1 Introduction to medical ultrasound Doppler techniques

1.1.1 Background

Ultrasound imaging is currently a major medical imaging modality used on an every day basis in many clinical applications. Its relative low cost, portability, and ability to deliver real-time, non-invasive images make it a very valuable diagnostic tool in obstetrics or in the assessment of cardiovascular diseases, for instance. Besides providing structural images, Doppler ultrasound techniques can also be used to detect and retrieve some information about the movement of blood or soft tissues in the human body. The origin of these techniques can be traced back to the work of Satomura in the late 50s [2]. Kaneko [3] reports that Samotura planned to use ultrasound to detect some small movements of the heart and the wall vessels and found a high frequency Doppler "noise" that he correctly attributed to the movement of blood. Interestingly, it seems that soon after Samotura's discovery the research was essentially driven by the development of techniques to detect and measure blood flow, and gave birth to the first Doppler flow-meters [4]. The application of Doppler ultrasound to echocardiography, (and for instance the application to the tracking of the myocardium's wall) only gained a widespread clinical use quite recently (from the 90's, [5]) although some earlier studies can be found. Today, most of

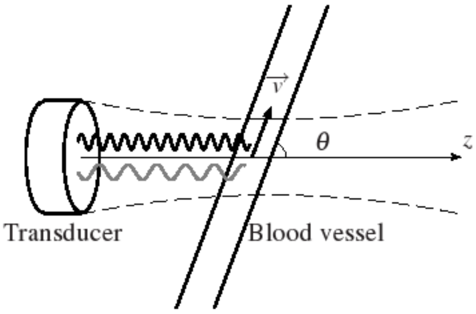

Figure 1.1: Illustration of the principle of the first CW Doppler flow-meters, the returned signal (in gray) is frequency shifted compared to the emission in black. The amplitude of the shift depends on the velocity of the flow.

modern scanners have Doppler imaging capabilities for blood flow (CFI, for Colour Flow Imaging) and echocardiography (Doppler Tissue Imaging, or DTI), although the acronyms may vary according to the manufacturer. More advanced techniques involve the computation of strain or strain rate in the tissues. Strain rate imaging has been recently applied to echocardiography (for instance [6]) to monitor the heart muscle (myocardium) condition after heart attack, for instance. A similar technique in principle, and called “elastography” or “strain imaging”([7]) images the stiffness of tissues based on an estimation of the displacement of tissues in response to a compression force. Some of these techniques are still at a research stage, but are quickly moving into clinical use.

1.1.2 From CW to PW medical Doppler device

The first Doppler flow-meters were Continuous Wave (CW) Doppler systems. Transducers were designed with two active areas, one for the transmission of an ultrasound wave in the range of MHz, the other for the reception of the backscattered signals from blood. The difference in frequency f_D of the returned signal frequency from the centre transmitted frequency f_0 is the Doppler shift due to the movement of the red blood cells and is proportional to the axial velocity component of the flow. The situation is depicted in Fig.1.1. The Doppler shift f_D and velocity are then related by the Doppler equation:

$$f_D = f_0 \frac{2v\cos\theta}{c}, \tag{1.1}$$

where θ is the angle of the blood flow with the axis of the transducer, and c is the speed of sound in the propagating medium. The velocities to be estimated in the human body rarely exceed 1.5 m/s, so assuming a speed of sound of 1500 m/s in the human body yields a coarse estimation of the maximum Doppler shift, which does not exceed 0.2 % of the centre frequency. Since the clinical range of frequency is the MHz, the associated range of Doppler shifts is the kHz. It can also be noticed from this equation that CW systems were only sensitive to the velocity component of the scatterers along the transmit direction. In fact, this is still the case in most Doppler techniques, although vector Doppler exists, which enables retrieval of the full velocity vector.

The relatively simple CW systems offer a very valuable diagnostic tool, but suffer from a lack of range resolution. In the example depicted in Fig.1.1, for instance, the system would only give an average of the velocity present in the blood vessel. Fine velocity variations across the vessel (for instance, typical parabolic velocity distributions) can not be measured. This problem was circumvented with the advent of coherent pulsed wave (PW) Doppler systems [8][9]. The principle consists of transmitting sinusoidal bursts of ultrasound periodically. The frequency at which these pulses are emitted is referred to as the Pulse Repetition Frequency (PRF), or equivalently the inverse of this quantity is called Pulse Repetition Period (PRP). In an idealised situation, the $(n+1)^{th}$ returned signals may be thought as a time-shifted version of the previous signal following the n^{th} transmit, due to the movement of scatterers. The shift in time associated with the movement is:

$$\Delta t = \frac{2\delta_{axial}}{c} \tag{1.2}$$

where δ_{axial} is the axial shift of scatterers. Alternatively, if $v_{axial} = v\cos\theta$ denotes the axial velocity component :

$$\Delta t = \frac{2v_{axial}T_s}{c} \tag{1.3}$$

For simplicity of notation in the remainder of this thesis, the notation v and δ will often be used in place of the axial component of velocity and displacement respectively. Fig.1.2 shows the received signals recorded after each burst transmit in this idealised situation (the signals were obtained with simulations). The gradual shift in time of the signal's patterns can be observed over the successive returned signals. From a mathematical point of view, if T_s denotes the PRP, and assuming that the scatterers have a constant axial velocity, the 2D received signals data can

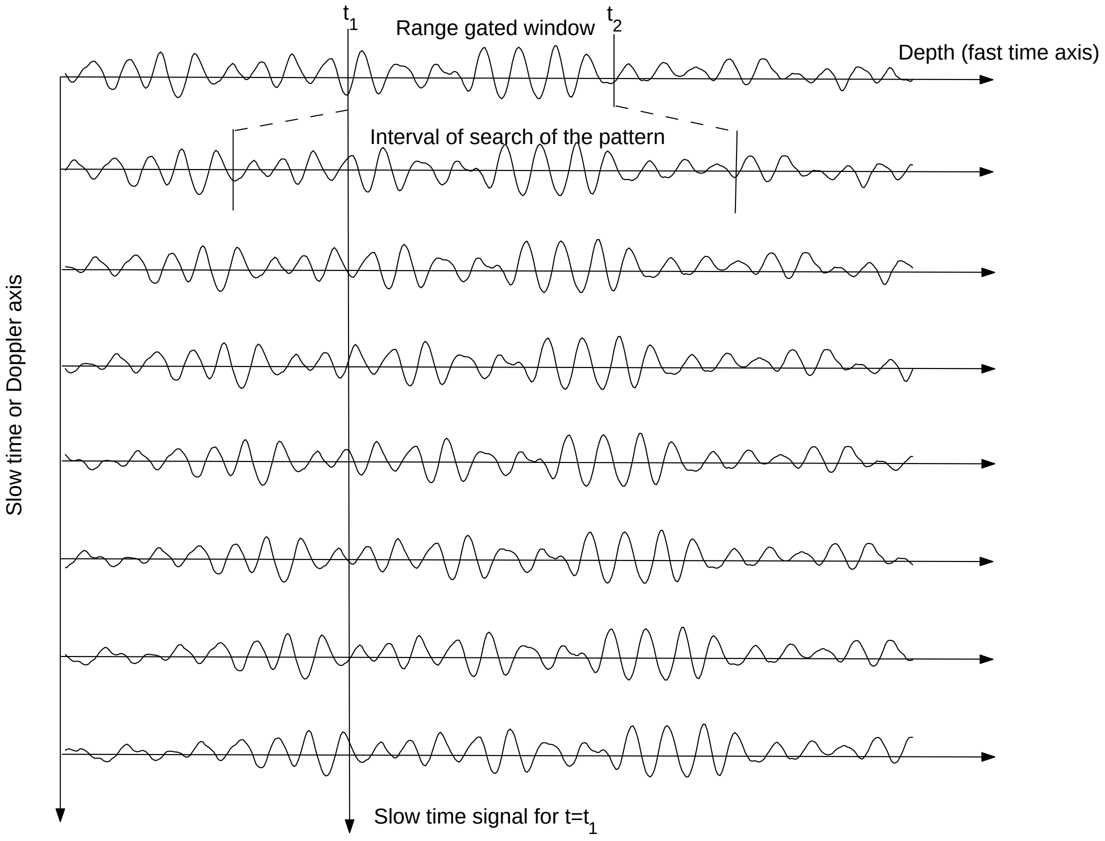

Figure 1.2: Successive returned signals in a PW Doppler system. Illustration of the “slow time” and “fast time” axis as well as the operation of range gating.

be described as:

$$r(t, nT_s) = r(t - n\Delta t, 0), \tag{1.4}$$

where $r(t, 0)$ is the signal received after the first pulse transmit and Δt is the time delay the signals undergo due to the displacement of scatterer. In this equation, n indexes the pulse/transmit cycles number. For a given time t_1, $r(t_1, nT_s)$ can also be interpreted as signal samples along the slow time axis, sampled at frequency $1/T_s$. The time of arrival t also called “fast time axis”, corresponds to the two way travel time from a given depth of return, or range. With this approach, its also possible to use the same transducer for transmit and receive, the receiver is only blind for a short time period corresponding to the pulse transmit. This is possible because the burst are usually short (a few wavelengths at the centre frequency in the MHz range, that is, approximately 1 mm) compared to the distance of propagation (a few centimetres). The next subsection will describe how the returned signals received can be used to perform velocity or displacement estimation.

1.1.3 Estimation strategies in a PW Doppler system

The use of pulsed "Doppler" instruments raised some new questions about whether the Doppler effect is actually used. Since the emitted pulses have a finite duration, they do not contain a single frequency, but rather, have a finite bandwidth, and each of the frequencies in the bandwidth can be thought of as having its own Doppler shift. The shift in the centre frequency of the pulse could still in theory be linked to the velocity of the backscattering particles. However, the frequency dependence of tissue attenuation also effectively shifts the centre frequency of a finite duration pulse as it propagates to and from the blood vessel(downshift). Rayleigh scattering is another effect that may also have a significant impact on the reflected pulse centre frequency (upshift), when considering backscattering from the red blood cells (see [10], for instance). The difference between the received signal centre frequency $\overline{f}$ and the transmitted centre frequency f_0 may then be written as:

$$\overline{f} - f_0 = f_D + \Delta f_{att} + \Delta f_R, \tag{1.5}$$

where Δf_{att} is the shift in frequency due solely to frequency dependent attenuation, and Δf_R is the shift in frequency due to Rayleigh scattering. In many practical situations, the overall shift can actually exceed the Doppler shift f_D by one order of magnitude. A direct application of the Doppler equation in this case would thus yield an error in the velocity estimate by one order of magnitude. In PW Doppler techniques, the velocity can thus not be estimated by measuring the shift in centre frequency over a single pulse/transmit receive cycle. Different estimation strategies can be adopted, which rely on several (at least two) transmit/receive cycles. The principle of estimation in PW Doppler system can be broadly classified into wideband and narrowband estimation strategies.

1.1.3.1 Wideband estimation techniques

Wideband techniques, or time-shift based techniques, rely on tracking the signal patterns in gated range windows to estimate the time shift Δt the signal has undergone over two successive received signals. The principle is depicted in Fig.1.2. A measure of similarity (usually crosscorrelation) is used to match the range gated window signal pattern between instants t_1 and t_2 with a segment of the successive returned signal of the same time duration, taken in a predefined interval of search. Extraction of a range gated portion of the signal is equivalent to isolate a finite volume in space in which scatterers contribute to the signal during the instant t_1 and t_2. Fig.1.3 shows a simplified representation of a single element focused ultrasound trans-

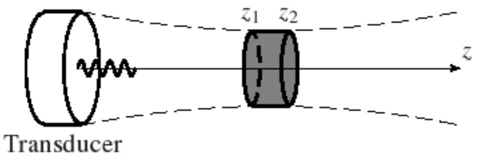

Figure 1.3: Schematic representation of the contributing volume of scatterers in a PW system.

ducer with its axis z. As the ultrasound burst propagates, it approximately insofinies a cylinder of axial length cT_p, where c is the speed of sound in the considered propagation medium and T_p is the time duration of the emitted ultrasonic burst. The contributing volume to the pulse echo received signal between the instant t_1 and t_2 is then:

$$z_2 - z_1 \approx c(T_p + t_2 - t_1)/2 \quad \text{and} \quad z_1 = c(t_1 - T_p)/2 \tag{1.6}$$

Following this approach, it is possible to break the signals into adjacent successive range gated windows, perform velocity estimation in each of these windows, and obtain a velocity (displacement) profile with depth.

1.1.3.2 Narrowband phase domain estimation

Although the interpretation in terms of a Doppler effect is not obvious for PW Doppler systems, a similar approach of estimation can be taken in terms of frequency estimation. In fact, it can be shown that the frequency content of the slow time signals is equivalent to a Doppler shifted spectrum version of the received signal along the fast time axis. Considering the previous model of Eq.1.4, and neglecting finite window effects (due to range gating and a limited number of pulse transmit-receive cycles in practice), it can be shown that the 2D PSD (Power Spectral Density) of the ideal received signal is [11]:

$$P(f, F) = \left| R(f)\delta(F - \frac{2v}{c}f) \right|^2 \tag{1.7}$$

Where $|R(f)|^2$ is the PSD of $r(t, 0)$, f denotes frequencies along the fast-time axis, and F, frequencies along the slow-time axis. This equation shows that the spectral content of the slow-time signal is a compressed, (with compression coefficient $\frac{2v}{c}$, depends on the axial velocity), of the fast time axis signal PSD. In particular, this relationship shows that if the centre frequency

$\overline{F}$ of the slow time signal can be estimated, the velocity can be estimated with the fast time signal centre frequency $\overline{f}$ by:

$$v = \frac{c}{2}\frac{\overline{F}}{\overline{f}}, \tag{1.8}$$

This is equivalent to a Doppler equation with Doppler shift $f_D = \overline{F}$. An important aspect is that when range gating is performed on the received signals, $\overline{F}$ "tracks" the change in the mean frequency $\overline{f}$ as it varies with the range gate so that their ratio is always equal to $\frac{2v}{c}$. Note that this is an idealised model of the spectrum of the slow time signals or so-called Doppler spectrum. In practice, the finite windows of observation need obviously to be taken into account, as well as a set of "spectral broadening" effects [12, p134-140]).

A variety of mean frequency estimators can be used to estimate the mean frequency $\overline{F}$ of the slow-time signal. In practice, the so-called "Kasai" algorithm or "1D autocorrelator" is the most used due to its computational efficiency and robustness in relatively high noise conditions. This estimator relies on the complex samples at given time (depth) $t = t_1$ of the baseband slow time signals obtained after coherent quadrature amplitude demodulation. This type of estimation is also often referred to as "phase domain estimation" and is a narrowband strategy of estimation. Its relationship with the phase shift the signals experience over several successive pulse transmits and the underlying narrowband approximation will be further detailed in Chapter 4. Without any additional filter at the receiver, this estimator is ideally sensitive to the the movement of scatterers present in the elementary "sample volume" of the system, which ideally only depends on the time duration of the pulse. The axial length of the sample volume is simply given by:

$$z_2 - z_1 \approx cT_p/2 \quad \text{and} \quad z_1 = c(t_1 - T_p)/2 \tag{1.9}$$

Two clear limitations in this estimation scheme can be pointed out. As stated in the beginning of this section, $\overline{f}$ changes with depth due to frequency attenuation and is unknown. This quantity is often assumed to be equal to f_0. This impacts the accuracy of estimation, but not as much as with a "true" Doppler shift direct approach, if the Doppler shift was directly estimated from a single received signal, as the difference between $\overline{f}$ and f_0. To illustrate this point, consider that the actual centre frequency in the gated range window is $\overline{f} = f_0(1-x)$ due both to frequency dependent attenuation and Doppler shift (for instance, $x = 5$ %). Assimilating $\overline{f}$ to f_0 yields:

$$v = \frac{c}{2}\frac{\overline{F}}{f_0} = \frac{c}{2}\frac{\overline{F}(1-x)}{\overline{f}} = \frac{c}{2}\frac{\overline{F}}{\overline{f}} - x\frac{c}{2}\frac{\overline{F}}{\overline{f}} \tag{1.10}$$

And the estimated velocity differs by $x = 5$ % from the true value, which is not ideal but yet acceptable. Another limitation of the preceding estimation scheme comes from the Nyquist criterion. For an unambiguous velocity estimation, the maximum frequency $\overline{F}$ present in the slow time signal should not exceed half the sampling frequency, or PRF ($1/T_s$). This means that:

$$F_{max} < \frac{1}{2T_s}, \tag{1.11}$$

and in terms of velocity,

$$v_{max} < \frac{c}{4T_s f_0} = \frac{\lambda}{4T_s} = \frac{\lambda}{4}\mathrm{PRF}, \tag{1.12}$$

where λ is the wavelength at the corresponding centre frequency. For an average value for the PRF of 5 kHz, and a centre frequency of 2.5 MHz ($\lambda \approx$ 0.6 mm) this yields a maximum velocity of 0.75 m/s. Doubling the frequency divides this maximum value by two. The maximum velocity estimated without any ambiguity and the corresponding displacement of $\lambda/4$ will be referred to as “Nyquist velocity” and “Nyquist displacement”. Similarly to what happens with spectra if the Nyquist limit is exceeded, a phenomenon of aliasing occurs with the estimated displacements or velocities.

1.1.4 Colour Flow Imaging

Modern scanners now use the full power of arrays of transducer elements to perform beam steering. The ultrasound beam can be quickly steered in different directions to acquire several lines of data. The same operations as described on a single line can be repeated over several lines, the 2D data set of velocity estimate is then encoded into a colour code yielding a velocity image in a region of interest. The resulting image is usually overlaid onto a grey-scale image (so-called B-mode image) to observe the axial velocity field distribution in relation to anatomic details. Fig.1.4 is an excerpt of the CFI display of a scanner in our lab, and illustrates the principle. The region of interest selected manually by the user corresponds to a stenosis in an artery flow phantom. The colour image corresponds to the velocity measured in this area. This image also gives a good idea of the resolution of the method. The diameter of the artery is 6 mm, it can be clearly seen that in the region of the stenosis, the colour code overlaps the boundaries of the vessel in the grey-scale image.

At the receiver, the signals are amplified with a radio-frequency amplifier, and then mixed with the signal of a local oscillator to remove the carrier. A lowpass filter is then applied to remove

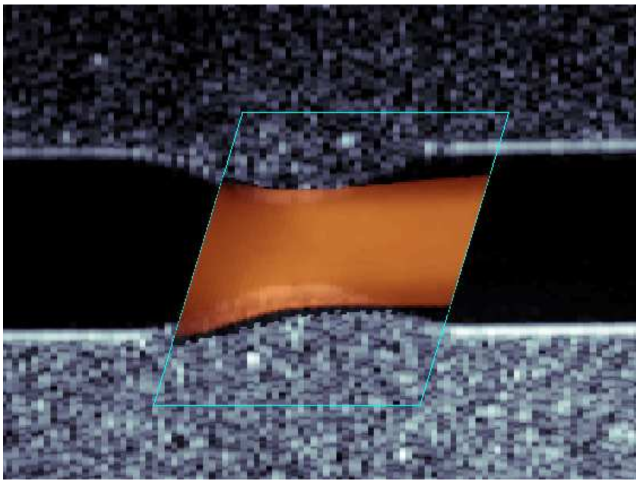

Figure 1.4: Excerpt from the CFI display of a modern scanner working on a femoral artery stenosis phantom in our lab. The velocity colour code image is overlaid onto a B-mode grey-scale image providing structural details.

noise (and harmonics from the demodulation process) and a clutter rejection filter is used to remove the strong stationary (or slowly moving) signals from the blood vessels and surrounding tissues (the difference in the backscattering power between blood and tissue is between 20 and 40 dB [13]). The obtained baseband signals may then be used to perform velocity estimation, usually using the 1D autocorrelator algorithm. The PRF used in practice is usually between 4 and 12 kHz [14], this parameter is limited at high depth, because obviously sufficient time needs to be allowed so that the signals arrive before a new pulse is emitted, if a maximum depth z_{max} needs to be investigated, we have:

$$\frac{1}{PRF} > 2\frac{z_{max}}{c} \tag{1.13}$$

Combining this equation with the previous limitation concerning aliasing yields the range-velocity limitation:

$$z_{max}v_{max} < \frac{c\lambda}{8} \tag{1.14}$$

The total frame rate of the system is limited by the number of transmit/received cycle N_p (usually between 6-12), the number of lines in a image, and the PRF used. Frame rate of 20 Hz and more are achievable but this figure also obviously decreases for high depth.

1.2 Introduction to coded excitation techniques

1.2.1 Definition and basic principles

The technique of coded excitation was introduced during the rapid development of radar technologies in the mid-50s [15]. It is now used in many engineering applications, including digital communications, sonar systems, and medical ultrasound. A coded waveform is essentially a waveform for which the time duration - bandwidth product T_pB is superior to one. The benefits of such waveforms can be understood in relation to the severe resolution-sensitivity trade-off associated with conventional Continuous Frequency (CF) pulses (sinusoidal bursts described in the previous section), for which the time-bandwidth product is approximately one. The sensitivity in the context of this work is the amount of signal received relative to a given level of noise at the receiver stage, which is quantified using the Signal to Noise Ratio (SNR). Taking the example of the returned signal from a single target, it is known that in the presence of white stationary noise, the maximum SNR achievable depends on the energy E_{echo} of the received echo:

$$\mathrm{SNR}_{max} = \frac{\text{Peak signal power}}{\text{Average noise power}} = \frac{2E_{echo}}{N_0}, \tag{1.15}$$

where N_0 is the noise power density in W/Hz of the receiver system. The energy of the received echo is proportional to the transmitted signal energy E, this coefficient is assumed to be one for simplicity. In the case of a conventional CF pulse (a square envelope amplitude is also assumed for simplicity), the energy is given by:

$$E = \frac{1}{2}A^2T_p \tag{1.16}$$

which yields:

$$\mathrm{SNR}_{max} = \frac{A^2T_p}{N_0} \tag{1.17}$$

where A is the amplitude of the pulse, T_p its time duration. For medical ultrasound applications, safety standards impose a strict limitation on the maximum peak pressure intensity, the energy of the transmitted pulse can thus not be increased beyond a certain threshold by increasing the amplitude A. Increasing the time duration T_p is possible but the limitation in the time-bandwidth product $T_pB \approx 1$ implies a proportional decrease of the conventional CF pulse bandwidth and thus, of the spatial axial resolution of the system. This trade-off is illustrated schematically in Fig.1.5. If we now consider the case of coded waveform with $T_pB = 10$, for example, this means that the time duration can be increased by 10 compared to a conventional

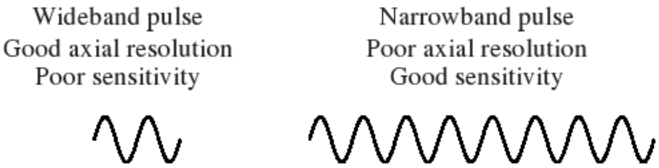

Figure 1.5: Illustration of the sensitivity/resolution for a conventional CF pulse.

pulse for an equivalent bandwidth B. As a consequence, the energy of the imaging pulse is multiplied by 10 (and thus a gain in SNR equal to the time-bandwidth product if the SNR of Eq.1.15 is achieved), without increasing the peak amplitude of the signals and without compromising the axial spatial resolution.

1.2.2 Decoding of the waveform, example of Linear Frequency Modulated (LFM) chirp

A way to increase the time duration-bandwidth product of a waveform is to introduce a frequency modulation in the signal. So-called linear frequency modulated (LFM) chirp are commonly used coded waveforms. The instantaneous frequency of these signals varies linearly with the time duration of the waveform. In terms of its centre frequency f_0 and its fractional bandwidth ($B_f = B/f_0$), this waveform can be put in the form:

$$e(t) = \sin\left(2\pi f_0\left[\left(1-\frac{B_f}{2}\right)t+\frac{B_f}{2T_p}t^2\right]\right) \quad t\in[0,T_p]. \tag{1.18}$$

Fig.1.6 (top, left) shows an example of an LFM chirp waveform with parameters $B_f = 0.5$, $f_0 = 5$ MHz and $T_p = 8$ μs, the time-bandwidth product achieved in this case is $T_pB = 20$. The same figure (top, right) shows an apodised conventional CF pulse with approximately the same bandwidth. The gain in time duration achieved through coding is visible. Clearly, the chirp waveform would have a very limited axial resolution if used as such, due to its long duration.

An essential step in the use of coded excitation involves a decoding filter stage, or also called compression stage at the receiver. The aim of the decoding filter is to restore the resolution of the pulse to approximately $1/B$. A common way to achieve compression is to use a matched filter, that is to filter the received signal by a time reversed version of the echo signal. In other

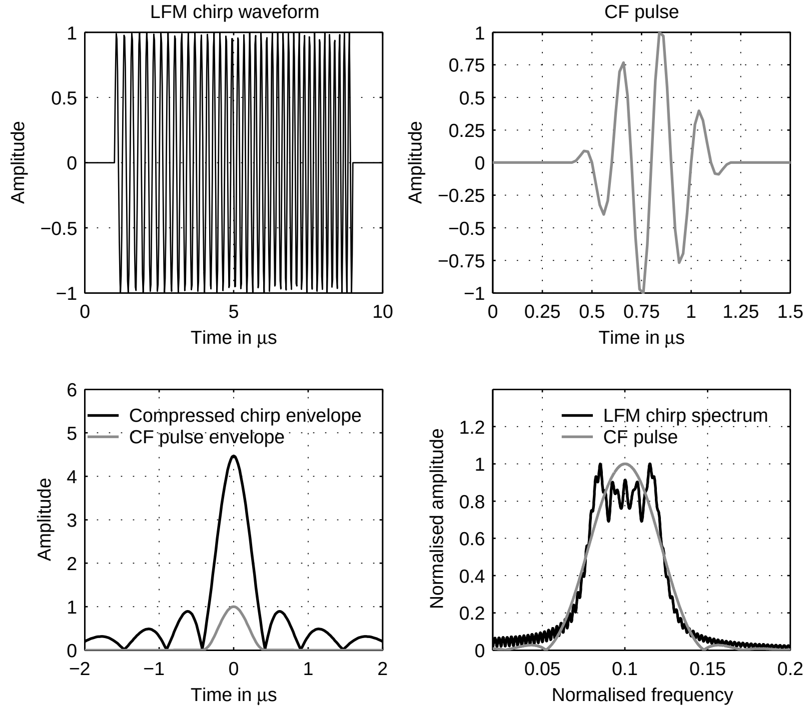

Figure 1.6: Top: (left) LFM chirp waveform with parameters: $B_f = 0.5$, $f_0 = 5$MHz and $T_p = 8$ μs, (right) conventional CF 4 cycles pulse. Bottom: (left) Comparison between the compressed chirp envelope and the CF pulse envelope, (right) Comparison between the spectra of the LFM chirp and the CF pulse

words, if we assume that the echo of the signal from a target is an exact delayed replica of the transmitted signal $s(t)$, the compression of the signal can be achieved using the filter of impulse response :

$$h_{matched\,filter}(t) = s(\tau_d - t) \tag{1.19}$$

where τ_d is a constant delay to make the filter causal. It is known as a result that the matched filter achieves the maximal SNR of Eq.1.15 [16]. Note that the result of filtering $s(t)$ by a matched filter is mathematically equivalent to the autocorrelation function of $s(t)$. Fig.1.6 (bottom,left) shows the envelope of the output of the matched filter for the chirp and compares it with the envelope of the conventional apodised CF pulse. As the gain in SNR is equal to the time-bandwidth product ($T_pB = 20$), the resulting compressed pulse amplitude is increased by a factor of $\sqrt{T_pB} = 4.5$, with the parameters chosen for example. After compression the duration of the pulse is clearly restored to approximately $1/B$ but an adverse effect of compression is the introduction of range sidelobes which are potentially a problem for imaging applications. Finally, the spectra of the waveforms are also represented in Fig.1.6 (bottom, right). The two waveforms have different spectra, but a similar bandwidth.

1.2.3 Pseudo-random binary sequences and the specific case of Barker codes

Another particular type of coded excitation are pseudo-random binary sequences. These baseband sequences are easily generated as sequences of “1” or “-1”. Each code is then characterised by its length in bit (a bit of these codes in this case is also referred to as a ‘chip’ in communication signal processing, as several chips may be used to encode one bit of information). Among all the possible binary sequences, Barker codes are sequences that achieve the best autocorrelation properties in terms of sidelobes level. The autocorrelation function of a Barker sequence of length N_b has the following property:

- the peak of the autocorrelation function is equal to N_b
- the sideblobes all have the same relative height of $1/N_b$

The gain in SNR achieved is also equal to N_b, or $10.\log(N_b)$, in dB. Unfortunately, the maximum length of a Barker sequence is $N_b = 13$ (which yields a maximum gain of approximately 11.1 dB). Sub-optimal long sequences with larger gains can however be obtained (so-called “M-sequences”). For transmission through an ultrasound transducer these sequences need to

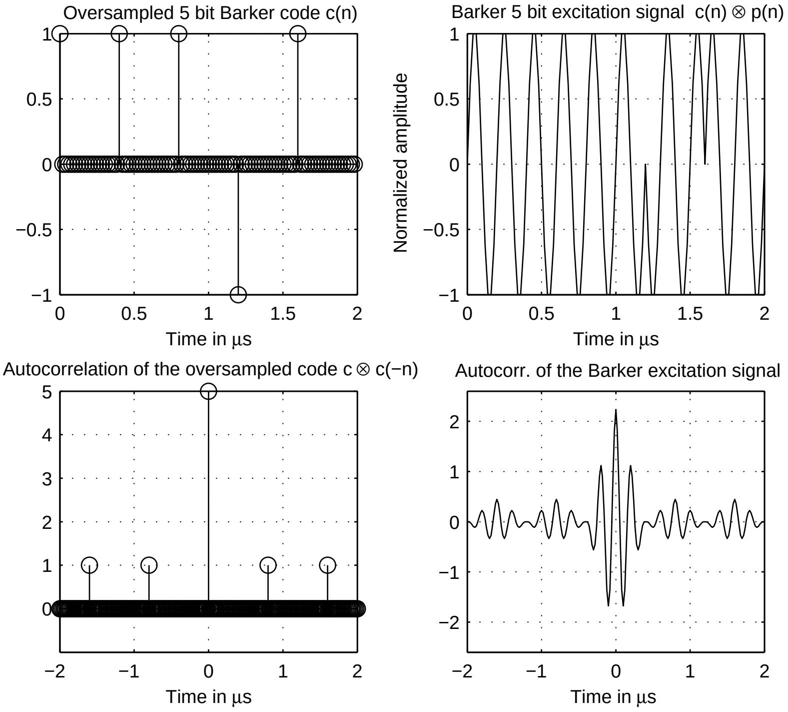

Figure 1.7: Left: (top) Oversampled Barker 5 bit sequence to be used with a 2 cycles CF base pulse, (bottom) autocorrelation of the oversampled Barker sequence. Right:(top) Barker coded excitation signal (Bottom) Autocorrelation of the Barker coded excitation signal

be modulated at the carrier frequency (centre frequency) of the transducer. Following the approach given in [17] the process can be seen as convolving an “oversampled” Barker sequence, that is, the Barker code chips are interleaved with a number of zero corresponding to an integer number of period at the centre frequency, with a CF base pulse of the same number of cycles. Fig.1.7 illustrates this process with an oversampled 5 bit Barker sequence ($N_b = 5$). The original baseband 5 bit Barker sequence is given by (1 1 1 -1 1). A 2 cycles CF base pulse was used, with centre frequency $f_0 = 5$ MHz (0.2 μs period) , and the sampling frequency was set to 50 MHz. As can be seen from the Barker coded excitation signal obtained, the coding achieved can be interpreted as a phase modulation of a 10 cycles long sinusoidal burst (with jumps of 180 degrees in phase corresponding to switches between 1 and -1 in the original Barker sequence). The obtained waveform has the same energy as a 10 cycles CF pulse but an equivalent bandwidth to a 2 cycles CF pulse. This translates into a gain of SNR of $N_b = 5$ compared to the CF base pulse after a matched filter (with Eq.1.15). The compressed pulse after a matched filter (autocorrelation of the Barker coded excitation signal) is shown in Fig.1.7 (bottom,right). Fig.1.8 also shows the spectra of the different waveforms involved. The original baseband se-

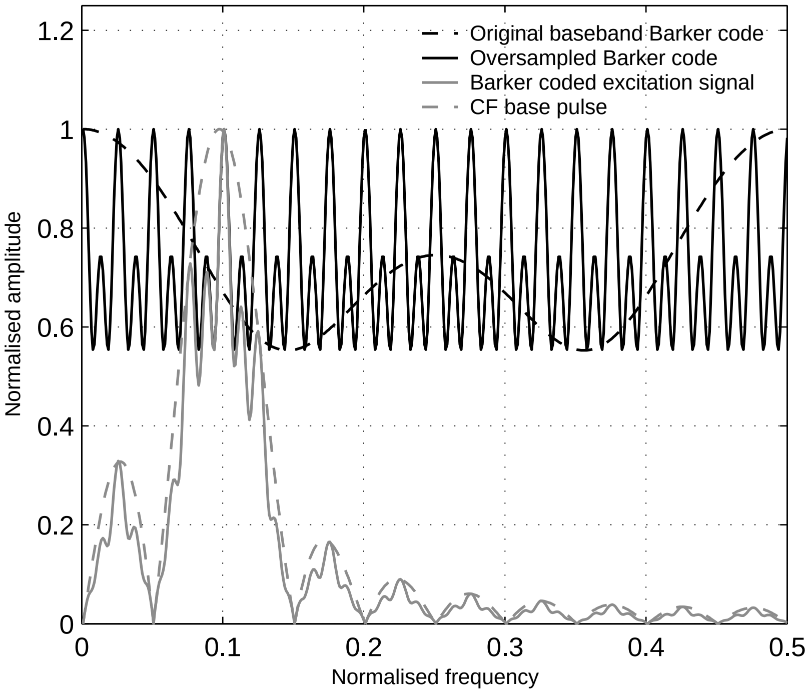

Figure 1.8: Left: (top) Oversampled Barker 5 bit sequence to be used with a 2 cycles base pulse, (bottom) autocorrelation of the oversampled Barker sequence. Right:(top) Barker coded excitation signal (Bottom) Autocorrelation of the Barker coded excitation signal

quence is very wideband, the "oversampled" spectrum is a periodised, compressed version of this sequence, and the final excitation signal is centered around the normalised frequency 0.1 (corresponding to a centre frequency of 5 MHz), with a similar bandwidth to the base CF pulse. Writing the excitation signal e and the "oversampled" sequence c and the base pulse p, the Barker coded excitation signal is thus obtained as:

$$e(n) = c(n) \otimes p(n) \tag{1.20}$$

This mathematical description also can be used to emphasise the difference in role of a decoding filter (to restore the pulse duration back to $1/B$) and a noise filter, which removes the noise from outside the useful bandwidth of the signal. The Barker excitation signal may be decoded using a time reversed oversampled sequence c(-n), the resulting waveform would be:

$$e(n) \otimes c(-n) = (c(n) \otimes c(-n)) \otimes p(n) \tag{1.21}$$

This effectively compresses the waveform at the receiver stage, but performs poorly in terms of noise rejection due to the broadband nature of the oversampled sequence $c(n)$ (see Fig.1.8). To obtain the expected gain in SNR, an additional bandpass filter would be necessary. Note that the matched filter achieves both pulse decoding and optimal filtering by using the base pulse as an additional bandpass filter:

$$e(n) \otimes e(-n) = \underbrace{(c(n) \otimes c(-n)) \otimes p(n)}_{\text{compressed pulse}} \otimes \underbrace{p(-n)}_{\text{bandpass filter}} \tag{1.22}$$

1.2.4 Coded excitation in the context of medical ultrasound

Although early systems description of Doppler flow-meters using coded excitation can be found (a specific litterature review for Doppler applications will be done in Chapter 3), the use of coded excitation in medical ultrasound had a slow uptake, and only gained a real interest quite recently (in the last decade). In one of the early descriptions of a coded system by Takeuchi in 1979 [18][19] the time-bandwidth restrictions imposed by the relatively small bandwidth of ultrasound transducers were pointed out. This may have impeded the development of these techniques in medical ultrasound , until significant progress was made with transducers materials and technologies, enabling larger bandwidths. In 1992, O'Donnell [20] described the implementation of a coded excitation ultrasound imaging system working with linear arrays. O'Donnell showed the SNR improvement coded excitation could provide for B-mode imaging, considering the most fundamental limit in noise source (thermal noise) and taking into account the maximum peak power intensity required for patient safety. His results showed a potential gain of 15-20 dB in SNR. One year later, Rao [21] described a system using a linear chirp that was able to improve the SNR by a factor of 20 and that offered similar resolution to a conventional short-pulse system, despite having a pulse length of 20 μs.

Coded excitation is nowadays a well-established technique for grey-scale B-mode imaging. Recent studies have focused in more detail on pulse compression and specific problems associated with ultrasound imaging, in particular, the problems of range sidelobes reduction, and issues associated with non-linear propagation and frequency-dependent attenuation in tissues. Misaridis et al recently reviewed the potential of coded excitation in ultrasound [22], and the theory underlying the use of LFM chirps, based on radar literature [23] [24]. The same authors were also able to design a system based on a modified commercial scanner, using a pre-distorted linear chirp, and demonstrated a gain in depth of penetration with this technique [25]. Other coded excitation schemes like pseudo-random binary sequences were also investigated in a number of studies, a good review of these works along with practical implementation considerations can be found in [17].

1.3 Presentation of this thesis work

1.3.1 Aim of the thesis

Doppler imaging modalities (this expression is used here in its broadest sense, and embraces all the techniques dealing with the estimation of displacements or velocities) are arguably the most complex task performed by clinical scanners, and have sustained a considerable effort of research in terms of signal processing for the last 40 years. It was quite natural, that, after coded excitation techniques were successfully applied recently to B-mode grey-scale imaging, similar improvements were sought for applications involving the estimation of blood flows or tissue movements. In fact, as will be more developed in Chapter 3, similar techniques had already been considered from the seventies with the design of the first Doppler flow-meters. This work is an investigation on the potential of coded excitation techniques to improve the performance of velocity and/or displacement estimation in medical ultrasound, in the context of modern estimation schemes and applications. Given the diversity of techniques and possibilities of implementations, some choices needed to be made. The notion of performance improvement itself may be quite application dependent and thus difficult to quantify from a general perspective. A possible approach would probably have been to implement some coded excitation schemes in a commercial scanner, test the new system for a specific clinical application on some physiological phantoms or on some patients in a clinical study, and then discuss the potential improvement in terms of image quality, in terms of any performance index relevant to the technique, and eventually, in terms of diagnostic value. This work however voluntarily takes a much more general approach, with, most of the time, a very general signal processing point of view on the potential of coded excitation. The overall goal of the thesis is thus to provide a general framework for understanding in which conditions and why coded excitation may lead to some improvements in the detection and estimation of motion for medical ultrasound applications. Two general aspects of performance improvement are investigated:

- the first aspect is the improvement in sensitivity and spatial resolution: sensitivity is a fundamental performance aspect of practical importance for blood flow estimation, for instance, because obviously, before discussing any other performance aspect, Doppler signals from the region of interest need first to be detected. Sensitivity improvements potentially lead to the ability to measure blood flow deeper in the body, or to yield better diagnostic data in the case of "technically difficult" patients. Another key aspect linked with sensitivity, is spatial resolution. It is known, from the first pulsed Doppler system implementations, that there is a trade-off between the spatial resolution of the transmitted pulse and the sensitivity: short pulses have inherently a good resolution but the energy transmitted is in turn limited, and thus the SNR conditions are poor. Two studies [17][26] have recently pointed out that coded excitation could be successful in improving this sensitivity/resolution trade-off for CFI applications. These aspects were already introduced in a previous section. There is a real need, however, to assess and study this potential improvement more quantitatively. Specific differences in terms of pulsing strategies, SNR conditions, safety requirements from B-mode imaging techniques need in particular to be taken into account to yield a relevant discussion.

- the second aspect is the statistical performance of the velocity estimates (bias, relative error), and the possibility to improve the reliability of the estimates with coded excitation. Again, a signal processing point of view is adopted, with the claim that robust estimates with good statistical properties will yield enhanced diagnoses.

1.3.2 Approaches chosen for this PhD work

The work carried out follows a classical path, with whenever possible, a theoretical approach, followed by some simulation studies. A comparison with some experimental data is also presented in the last chapter. A basic requirement for a simulation signal processing study is to understand the basic statistical properties and spectral characteristics of the signals involved and to be able to model these properties. The choices made in this work are towards simplicity, generality, and computational efficiency for simulations. Rather than trying to grasp or model the full complexity of signals in some specific situations, a simple signal model is used for all the simulations (which can yet be justified within certain physical approximations). The goal is to render some fundamental behaviour of the velocity/ displacement estimators, with parameters like the bandwidth of the transmitted signal or the SNR conditions. Some choices also had to be made concerning the estimators to be tested, which were categorised into phase shift based estimators and time shift based estimators. These types of estimators are relevant to a lot of applications in practice, although a lot of more advanced algorithms could also have been studied. This relatively simple classification of estimators is of particular relevance for the use of coded excitation, as will be seen, because it also corresponds in general to narrowband estimation strategies and wideband strategies. Specific focus will be put in this thesis to critically review and adapt previous works concerning the theoretical aspects of statistical performance for these two types of estimation. Indeed, if it is known on a theoretical basis how the performance of these estimators is affected, it is then easier to understand how and in which situations coded excitation might be beneficial. Finally, the experimental work is based on a relatively simple system with a single element transducer and a custom-designed receiver, to obtain a full control of the signal processing chain. The test object used for the experiments is a rotating phantom, which was chosen again for its ease of implementation and flexibility rather than to reproduce a specific physiological motion.

1.3.3 Structure of the thesis

Chapter 2 studies experimentally some aspects of the transmission and the compression properties of different coded waveforms with an ultrasound transducer, and in particular the impact of coded excitation on the sample volume of systems. The goal of this chapter is also to present the equipment which was used for data acquisition in Chapter 6. Chapter 3 provides a theoretical framework and some simulations to understand the potential improvements in resolution and sensitivity improvement with coded excitation for velocity estimation applications. These aspects are studied in the context of CFI applications, due to the historical importance of this technique and its clinical relevance. This chapter also discusses and reviews a model of signals that will be adopted in the rest of the thesis. As a complement, this chapter also addresses some practical considerations in the implementation of a CFI system working with coded waveforms. Two types of coded excitation, Barker codes and LFM chirps, are compared both on their potential to improve the resolution / sensitivity trade-off and ease of implementation. Chapter 4 studies the potential impact of using a phase shift based estimators with some relatively wideband coded waveforms, in terms of statistical performance. It starts with a theoretical detailed analysis of this type of estimator (namely the “1D autocorrelator” or “Kasai” algorithm). It also reviews and adapts a theoretical expression for the statistical performance of the estimator, and concludes with an extensive simulations study. Chapter 5 is dedicated to time shift based estimators. The importance of this type of estimator in the context of current applications is emphasised. The statistical performance of this type of estimator is thoroughly investigated, and a simulation study concludes on potential improvements with coded excitation. Finally, chapter 6 compares the findings of the simulation data with some experimental data acquired with the custom designed rotating phantom. Each chapter can be read independently, although some results from other chapters might be needed. For instance, the model of signals adopted and the relatively simple simulation scheme used in Chapter 3, 4 and 5 are not repeated every time. Chapter 3 and 4, along with the experimental results concerning the statistical performance of phase shift based estimators in Chapter 6 can also be read together as a feasibility study of the implementation of coded excitation in a CFI system. Chapter 5 is a more stand-alone, general chapter about the performance of time shift based estimation with coded excitation which could be applied to a lot of applications.

Chapter 2

Transmission of coded waveforms through an ultrasonic transducer

Due to the limited bandwidth available, ultrasonic transducers play a significant role in the transmission of relatively wideband coded signals. This chapter has a double objective: first, to present the material and equipment used for the collection of experimental data; second, to study pulse-echo fields obtained when transmitting coded waveforms with a single element transducer. The same transducer will be used in Chapter 6 for velocity data acquisition experiments. The first section presents the material and equipment used to collect data. Experimental data are presented in the second section comparing the uncompressed and compressed pulse-echo on-axis fields. Values for the gain in SNR are compared and discussed for different LFM chirp waveforms and Barker codes. The third section focuses on the compression properties of the coded waveforms at the acoustic focus. The axial resolution and level of range sidelobes after compression are examined. Finally experimental points spread functions at the focus are obtained and compared along with the lateral resolution for the different excitation signals.

2.1 Material and equipment for data collection

2.1.1 Acquisition set-up

The basic acquisition set-up is presented in Fig.2.1 and consists of :

- an arbitrary waveform generator (AWG) Agilent 33250A that is used to generate all the excitation signals.
- a power amplifier ENI 240L providing a gain of 50 dB necessary to generate the voltages required to excite the transducer (typically $\approx$ 100V).
- an "expander-limiter" protection circuit that protects the receiver during the transmission of the relatively high voltages transmission voltages.

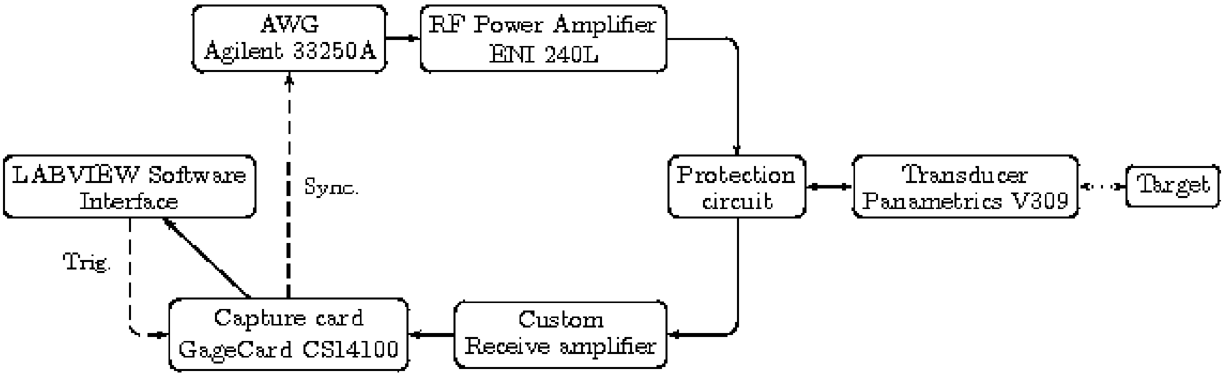

Figure 2.1: Basic experimental set-up for data acquisition

- a custom receiver amplifier, based on two integrated circuits by Analog Devices (a preamplifier AD8331 and an amplifier AD605) providing a maximum gain of 89 dB.

- a 14 bit capture card GageCard CS 14100, with a maximum sampling frequency of 100 MHz.

A LabView (National Instruments) interface was developed to control the acquisition settings of the capture card. A software trigger solution was implemented, which showed good jitter performance (this aspect will developed more fully in Chapter 6). The LabView interface also provides a means to independently set the gain of the preamplifier and the amplifier. Fig. 2.2 reports the frequency response of the power amplifier ENI 240L, measured with an oscilloscope set on a 50 Ω input impedance. The obtained gain is relatively constant around 49 dB for the range 100 kHz to 8 MHz, the -6 dB cut-off frequency is approximately 10 MHz. Fig.2.3 shows the total gain of the custom receiver amplifier for the particular settings used in all experiments yielding a gain of about 50 dB. The custom receiver amplifier exhibits a massive bandwidth (the -6 dB bandwidth is approximately 150 kHz- 20 MHz), but the obtained dynamic range is in turn a bit limited, and was measured to be around 44 dB for this particular setting (noise level of 20 mV peak to peak of noise for a maximum swing of the output signal of 3.3 V peak to peak). In addition to this instrumentation chain, an X-Y test rig system driven again through a Labview interface allowed to position the transducer in a water tank, the set-up is illustrated by a picture in Fig.2.4.

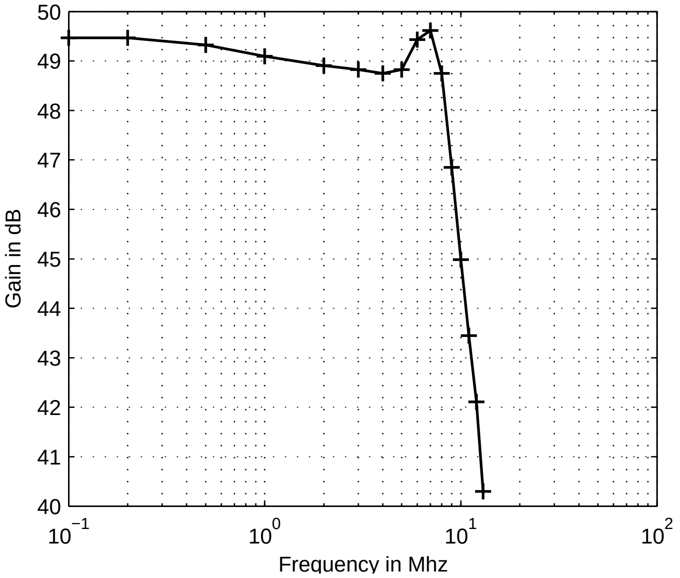

Figure 2.2: Gain of the RF power amplifier ENI 240L against frequency.

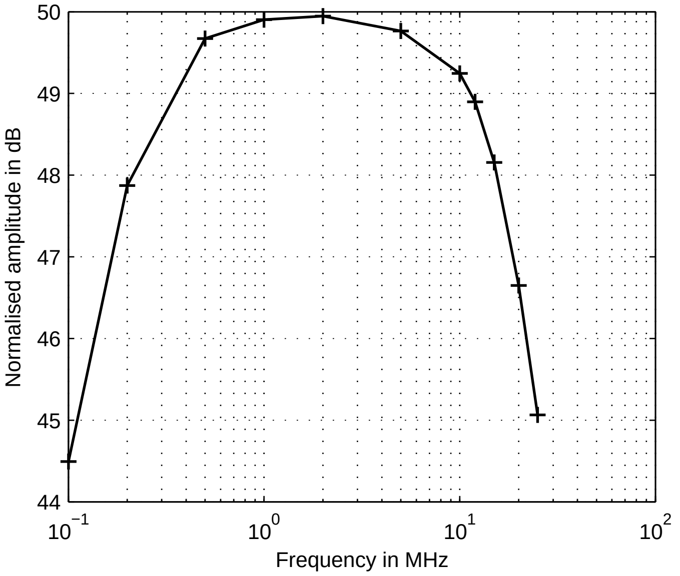

Figure 2.3: Gain of the custom receiver amplifier for a particular setting against frequency.

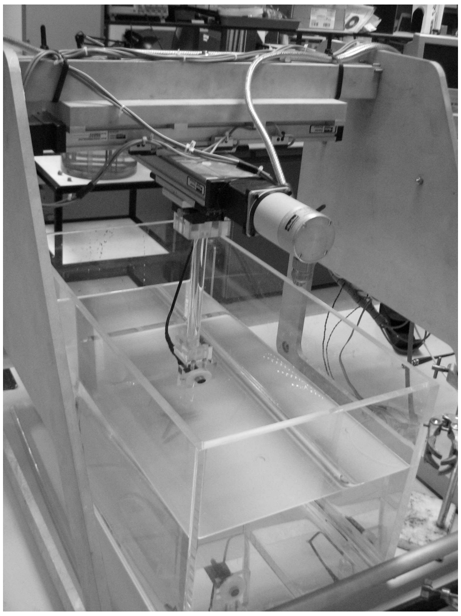

Figure 2.4: Picture showing the transducer mounted on a rod attached to an X-Y test rig system.

2.1.2 Transducer specifications

For all experiments, a Panametrics V309 single element transducer was used (which is primarily intended for non destructive testing applications). This is a circular, concave (focused) transducer, with the following specifications, as given by the manufacturers, measured with the ASTM standards [27]:

- diameter: 0.5 inch
- acoustic focus: 50.9 mm
- centre frequency: 5.6 MHz
- fractional bandwidth: 79.6%

2.1.3 Acoustical calibration of the transducer

The acoustical pressures at the focus of the transducer were measured for different excitation voltages. A PVDF membrane hydrophone (Precision acoustics Ltd., Hampton Farm, Dorchester, UK) was positioned at the focus of the single element transducer (50 mm in depth), the measurements were taken in degassed water, at ambient temperature (20°C). A 4 cycles Continuous Frequency (CF) pulse with centre frequency set at the centre frequency of the transducer

(5.6 MHz) was transmitted at different excitation voltages from 10V to 150 V and the positive and negative peak amplitudes of signals at the output of the hydrophone preamplifier were measured on an oscilloscope. The measured amplitudes could then be converted into an acoustic pressure using the sensitivity calibration curve of the hydrophone provided by the National Physical Laboratory (Teddington, Middlesex, UK). Figure 2.5 reports the measurements. As can be seen, the transducer used for experiments is able to deliver 4.5 MPa acoustic positive peak pressure amplitude at the focus, for the maximum excitation voltage tested (150V). The effect of non linear propagation in water, which translates into a very different behaviour of the positive peak pressure and the negative peak pressure at high excitation voltages is clearly seen on the figure. The maximum negative peak pressure measured was approximately of 1.8 MPa for the highest tested voltage. The corresponding Mechanical Index (MI)(which is used to characterise the risks of mechanical damage due to exposure to ultrasound) can be readily computed as [28, p516]:

$$\mathrm{MI} = \frac{e^{-0.0345 f_0 z} p-}{\mathrm{CMI}\sqrt{f_0}} \approx 0.3 \tag{2.1}$$

where in this equation $p-$ is peak negative pressure in MPa, derated with the exponential term (according to [12, p370], for an attenuation of 0.3 dB/cm/MHz), z is the focus depth (5 cm) CMI is worth 1.0 MPa/ MHz$^{\frac{1}{2}}$, and f_0 is the centre frequency. In our case, this yields an MI of 0.3, which is a moderate value compared to the maximum values found in diagnostic equipment for Colour Flow Imaging (up to 1.5, according to [29, p334]).

2.2 Study of on-axis coded pulse-echo fields

2.2.1 Acoustical fields with coded excitation: a brief review

It appears that very few authors have studied in depth the properties of ultrasonic fields at the output of a transducer excited by coded waveforms experimentally. These aspects were recently studied by Nowicki et al. in two papers. In [30], the sound fields generated by different coded excitation schemes were compared. It was logically observed that the uncompressed fields obtained with the long coded transmitted waveforms exhibited directivity patterns characteristics similar to those observed for long sinusoidal excitation. In contrast, the patterns observed after compression were similar to those produced by brief wideband sinusoisal bursts. Interestingly, Nowicki et al. also observed that the maximum peak pressure after compression was shifted towards the surface of the transducer by 15 mm for the Barker codes.

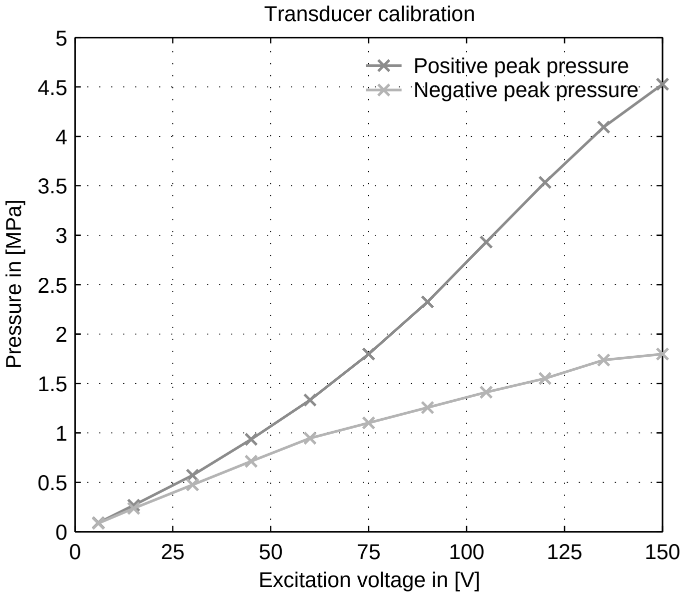

Figure 2.5: Peak pressures recorded at the output of a hydrophone as a function of the transducer's excitation voltage.

The study also reported some values for the gain in SNR measured after compression. However, the values reported appear to be excessively high compared to theory: 19.5 dB of gain for an 8 μs LFM chirp and 15.2 dB for a 13 bit Barker code. For the centre frequency used in the study (f_0= 2 MHz) one would expect a maximum gain in SNR (GSNR) for the chirp, (assuming a 100% fractional bandwidth B_f for the transducer):

$$\mathrm{GSNR} = 10.\log(TB_f f_0) = 10.\log(8\mathrm{E}-6 * 1 * 2\mathrm{E}6) \approx 12\,\mathrm{dB} \tag{2.2}$$

And for the Barker codes, the expected gain in SNR is:

$$\mathrm{GSNR} = 10.\log(13) \approx 11.1\,\mathrm{dB} \tag{2.3}$$

In [31], the same authors studied the compression properties of coded waveforms after propagation through some pork tissue and beef liver. They were able to demonstrate that despite non linear propagation and frequency dependent attenuation effects, which substantially affected the beam properties, the coded waveforms maintained good compression properties, which translated into an increase of the dynamic range of the received signals compared to conventional CF sinusoidal burst pulses.

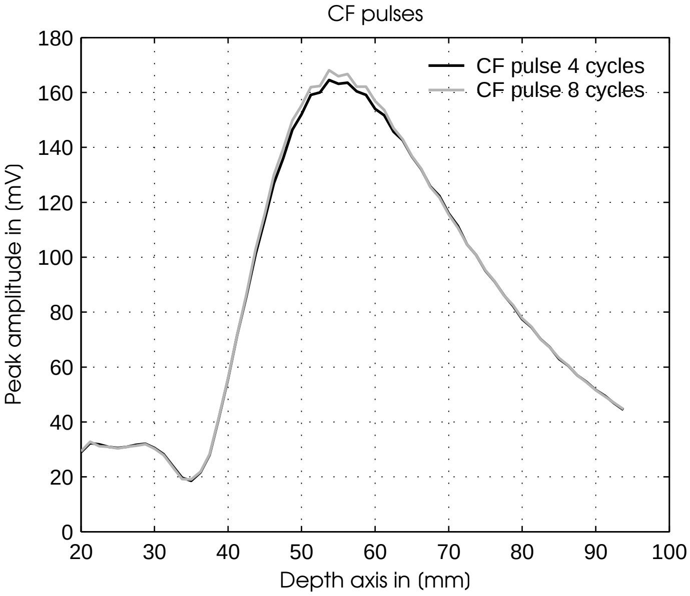

Figure 2.6: Pulse-echo peak amplitude against on-axis depth for CF pulses of length 4 cycles and 8 cycles.

The preceding studies were restricted to the transmit field (i.e. as measured by a hydrophone). We here propose to study the compression properties of LFM chirps and Barker codes in a pulse-echo experiment. We also report experimentally obtained point spread functions for these coded waveforms at the focus in the last section.

2.2.2 Study of on-axis uncompressed fields

The on-axis uncompressed coded acoustical fields emitted by the transducer were studied in a pulse-echo experiment using a $100\mu\mathrm{m}$ wire target. The wire target was set perpendicularly to the depth axis of the transducer using the X-Y rig system and the received signals from different excitation waveforms were recorded along depth. All the experiments were carried out with the same excitation voltage 30V, with the same centre frequency for all signals (5.6 MHz) and the waveforms were averaged 16 times to provide a good SNR. Fig.2.6 reports the measured peak amplitudes along depth with two CF pulses of length 4 cycles and 8 cycles. The following figures (2.7 and 2.8) report the measurements for 3 chirps of length $10\mu\mathrm{s}$, and fractional bandwidths $B_f = 0.15$, $B_f = 0.5$, $B_f = 1.0$ and three different Barker codes: a 5 bit code modulated by a 1 cycle pulse, 5 bit code modulated by a 4 cycle pulse and 13 bit code modulated by a 1 cycle pulse.

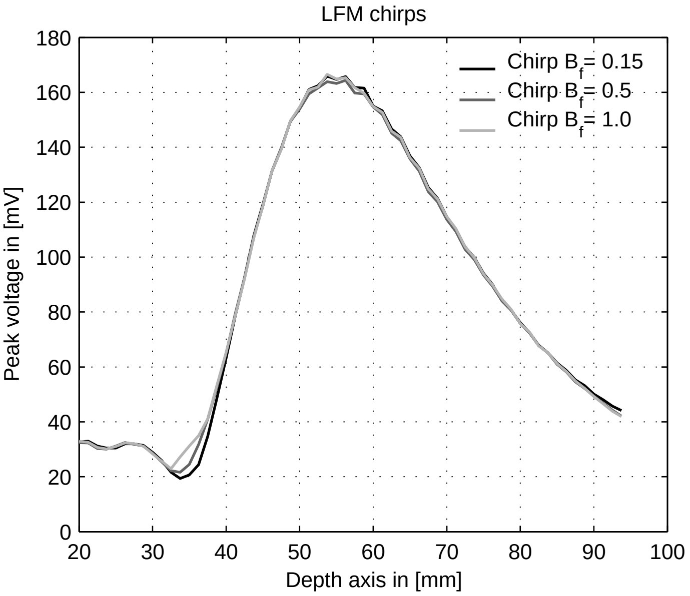

Figure 2.7: Pulse-echo peak amplitude against on-axis depth for LFM chirps of length 10 μs and fractional bandwidths B_f = 0.15, B_f = 0.5, B_f = 1.0.

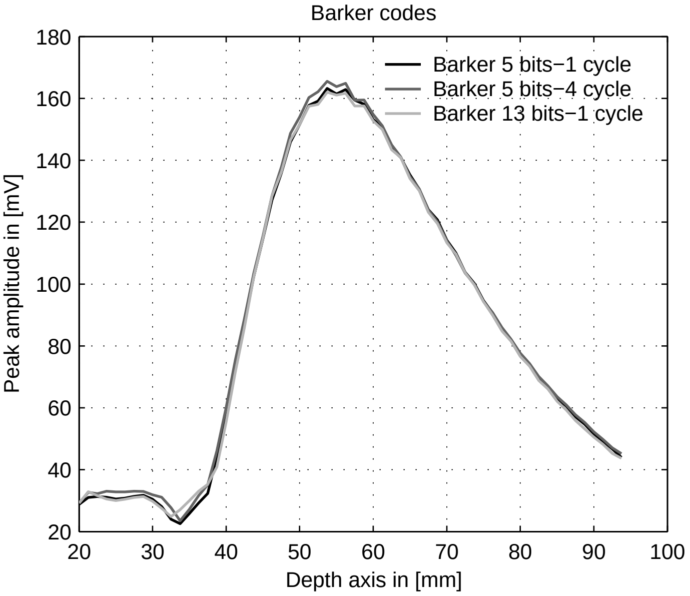

Figure 2.8: Pulse-echo peak amplitude against on-axis depth on a wire target for three different Barker codes (5 bits with a 1 cycle base pulse, 5 bits with a 4 cycles base pulse and 13 bits with a 1 cycle base pulse.

As can be seen, all the excitation signals tested yielded a very similar field profile with depth, with the same maximum peak amplitude voltage at the receiver. This maximum is located at a distance of approximately 55mm from the transducer's surface.

2.2.3 Compressed fields

The preceding received signals were compressed using a matched filter and the obtained gains in SNR were computed by measuring the peak amplitude level gain at each depth. The results are reported for each of the preceding tested coded waveforms, the amplitudes were normalised to the peak voltage amplitude of the uncompressed fields, and the measured gains were converted into dB. The following figures Fig.2.9, 2.10, 2.11, and 2.12,2.13, 2.14 report the results obtained for the tested chirp waveforms and Barker codes, respectively. As can be noticed, the obtained compressed fields are very similar to the uncompressed fields, with simply a gain in amplitude. This translates into a relatively constant gain in SNR with depth, apart from some fluctuations in the near field.

Tables 2.1 and 2.2 also report the gain in SNR measured at the focus, along with the theoretical expected value. The theoretical values were computed as:

$$\mathrm{GSNR} = 10.\log(N_b), \tag{2.4}$$

for the Barker codes, where N_b is the length of the baseband Barker code used (5 or 13 bit). For the chirps, the theoretical gain in SNR was computed using the time-bandwidth product of the waveform:

$$\mathrm{GSNR} = 10.\log(T_p B_f f_0). \tag{2.5}$$

The results clearly show that for wideband waveforms (chirp B_f = 1.0, and Barker codes with 1 cycle base pulse) the measured gains in SNR are significantly lower than the predicted theoretical values (by 4 to 5 dB). As the excitation waveforms become more narrowband, the gain in SNR measured gets closer to the expected values (5.4 dB vs 7 dB for the Barker 5 bit 4 cycles pulse and 8.6 dB vs. 8.75 dB for a chirp B_f = 0.15). This can be understood by considering the role of the transducer as a bandpass filter and recalling that after a matched filter the SNR only depends on the energy of the transmitted waveform: when trying to transmit a very wideband pulse, a significant fraction of the energy of the excitation signal is lost by the filtering process, and as a consequence, the obtained gain in SNR deviate significantly from the

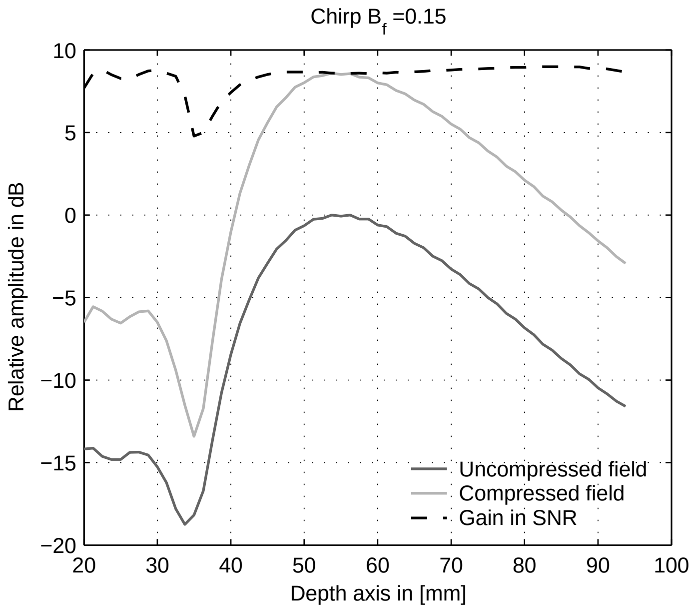

Figure 2.9: Peak amplitudes and gain in SNR in dB with depth for an LFM chirp of length 10 μs and fractional bandwidth $B_f = 0.15$

Chirp	Gain in SNR (dB)	Theoretical gain (dB)
$B_f = 1.00$	13.4	17
$B_f = 0.50$	12.8	14.5
$B_f = 0.15$	8.6	8.75

Table 2.1: Gain in SNR measured at the focus for three different chirps and comparison with the theoretical values. As the bandwidth of the chirp is increased, the difference with the theoretical predicted value becomes more important.

theoretical values. On the contrary, if the signal to be transmitted has a fractional bandwidth smaller than that of the transducer, the transducer acts as an allpass filter and all the energy of the excitation signal is effectively transmitted.

2.3 Study of the compression properties at focus

2.3.1 On-axis range sidelobes and axial resolution

This subsection studies the level of the range sidelobes and the axial resolution obtained after compression of the signals received when the wire target was positioned at the focus. The signals plotted in time domain in the upper graphs of Fig.2.15,2.16, and 2.17, clearly show the increased apodisation of the chirp excitations signals due to the transducer when increasing

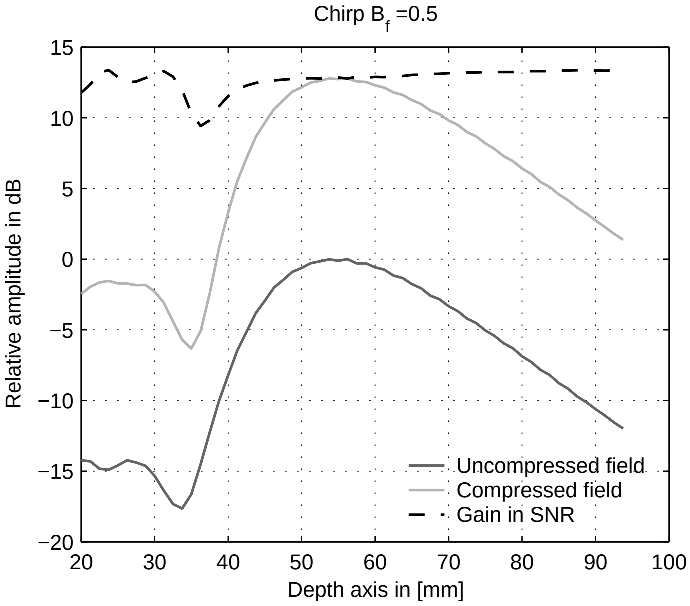

Figure 2.10: Peak amplitudes and gain in SNR in dB with depth for an LFM chirps of length 10 μs and fractional bandwidth $B_f = 0.5$.

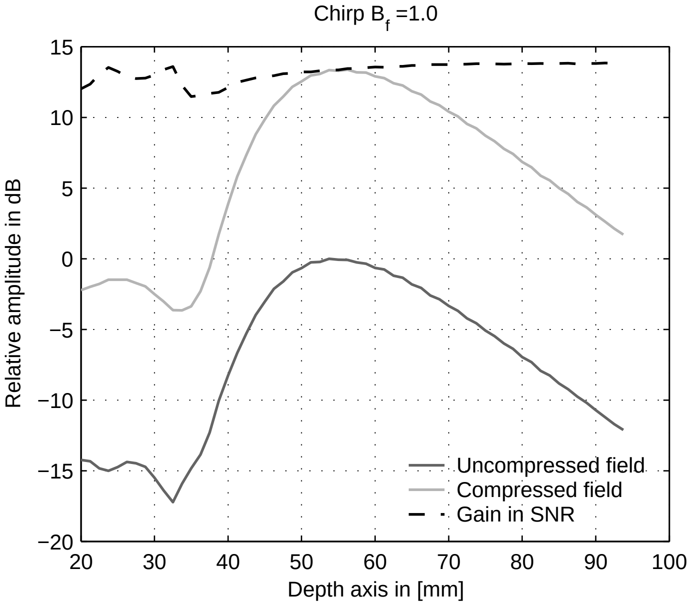

Figure 2.11: Peak amplitudes and gain in SNR in dB with depth for an LFM chirps of length 10 μs and fractional bandwidth B=1.0 .

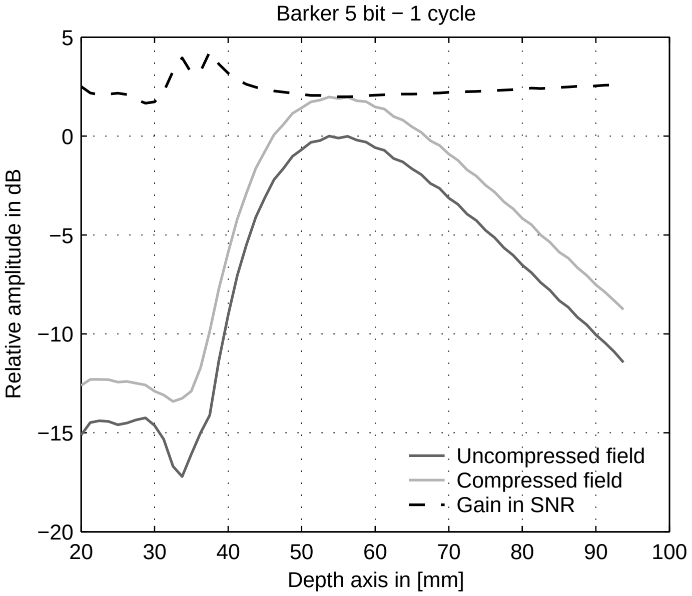

Figure 2.12: Peak amplitudes and gain in SNR in dB with depth for an Barker code 5 bits 1 cycle.

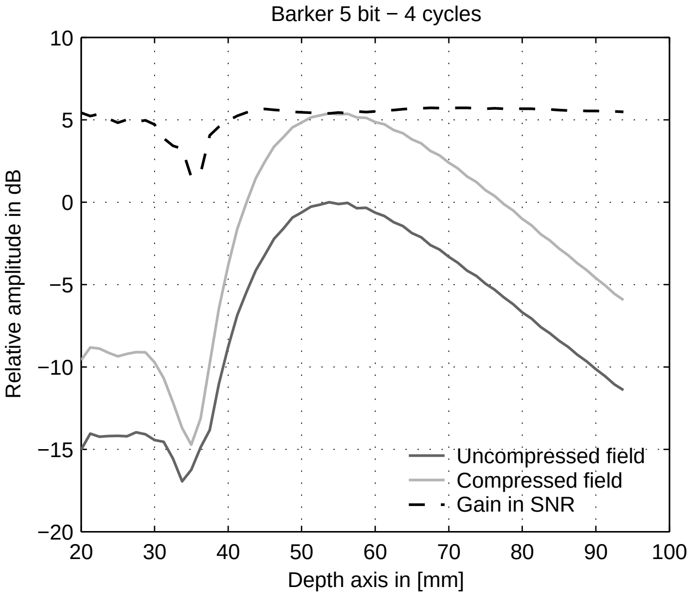

Figure 2.13: Peak amplitudes and gain in SNR in dB with depth for a Barker code 5 bits 4 cycles.

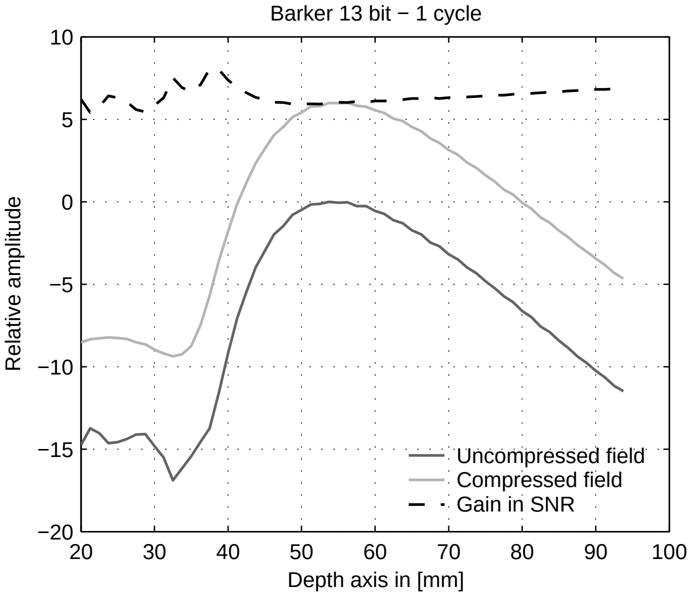

Figure 2.14: Peak amplitudes and gain in SNR in dB with depth for a Barker code 13 bits 1 cycle.

Barker code	Gain in SNR (dB)	Theoretical gain (dB)
5 bit 1 cycle	1.97	7.0
5 bit 4 cycles	5.40	7.0
13 bit 1 cycle	5.99	11.1

Table 2.2: Gain in SNR measured at the focus for three different Barker codes and comparison with the theoretical values. A significant difference is observed in the case of the wideband waveforms obtained with a 1 cycle base modulating pulse.

the fractional bandwidth of the chirp excitation signal. To understand the effect of the transducer on the compression properties, the lower graph of each of these figures compares the normalised amplitudes of the compressed experimental received signals with the compressed excitation signals. The horizontal axis of these graphs presents the axial distance from the peak of the compressed signal (essentially time delays were converted into distances, assuming a speed of sound in tissues of 1540 m/s). As can be easily understood, for narrow bandwidths, the sidelobes structure of the compressed experimental received signals is very similar to that observed when compressing the excitation signal (see 2.15 and 2.20). As the fractional bandwidth increases, the apodisation of the transducer has a beneficial impact on the level of the sidelobes, but the axial resolution is degraded compared to the case when the excitation signal is compressed (Fig.2.17). Fig.2.18 compares the three experimental compressed LFM chirp waveforms, the gain in axial resolution and the decrease in the levels of the primary sidelobes is clearly visible when increasing the fractional bandwidth of the chirp.

The following figures 2.19, 2.20 and 2.21 show that in the case of Barker codes, the transducer has little effect on the sidelobes level which remain close to their theoretical level ($20.\log(1/N_b)$, see section 1.2.3). As can be seen as well, the spatial axial resolution of the received signals is notably degraded compared to the ideal spatial axial resolution obtained when compressing the Barker coded excitation signal when the signals are wideband (2.19 and 2.21).

The following tables Table 2.3 and Table 2.4 give more insights into the spatial axial resolution of the compressed pulses, which was measured using the Full Width at Half Maximum (FWHM). These values can be compared with the wavelength λ at the centre frequency used (5.6 MHz), which is approximately of 0.26 mm. The axial resolutions obtained with the compressed received signals are thus excellent for the most wideband waveforms(0.84 λ for the chirp $B_f = 1$, 0.92 λ for the Barker code 5 bit 1 cycle, and 0.96 λ for the Barker 13 bit 1 cycle). It is clear, however, that these waveforms could not be used as such for imaging purposes, because of the relatively large range sidelobes obtained. These sidelobes should be reduced below the dynamic range of an image (typically 40 dB and more) to ensure that their presence does not create any artifact.

2.3.2 Experimental point spread functions

This subsection presents the obtained point spread function recorded at the acoustic focus of the transducer. From an imaging point view, point spread functions are important because they

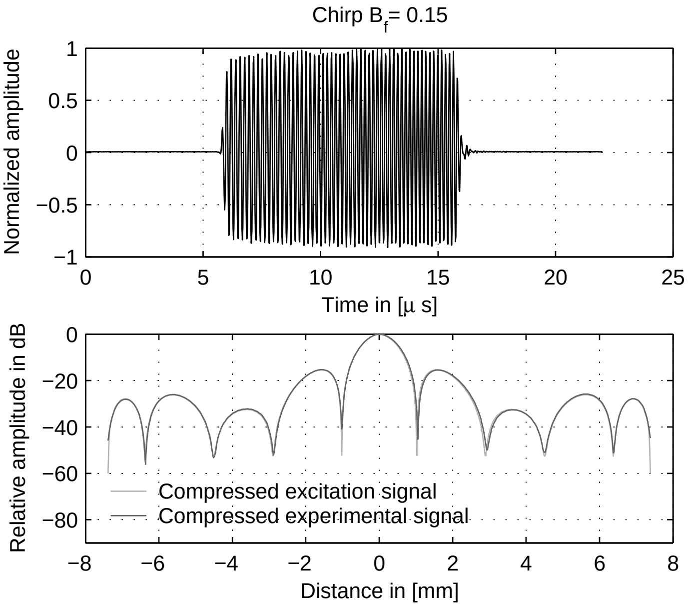

Figure 2.15: Top: Signal received from a wire target at focus for a chirp excitation signal with fractional bandwidth $B_f = 0.15$. Bottom: Compressed experimental signal and comparison with the compressed excitation signal.

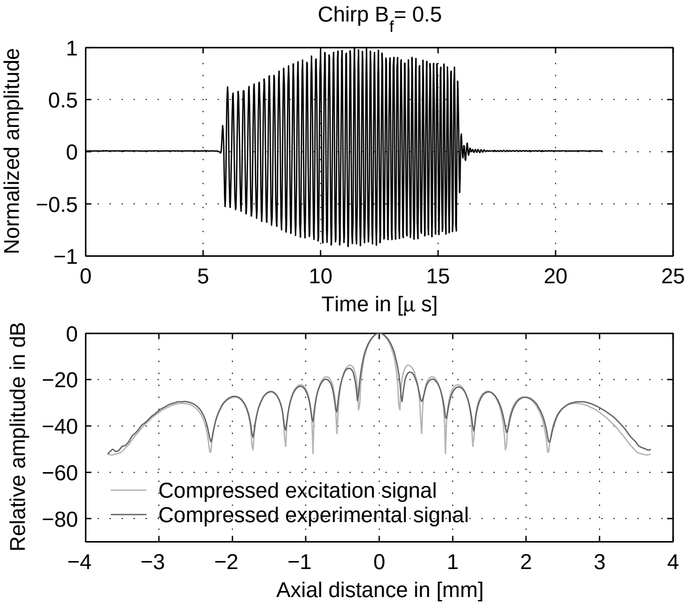

Figure 2.16: Top: Signal received from a wire target at focus for a chirp excitation signal with fractional bandwidth $B_f = 0.5$. Bottom: Compressed experimental signal and comparison with the compressed excitation signal.

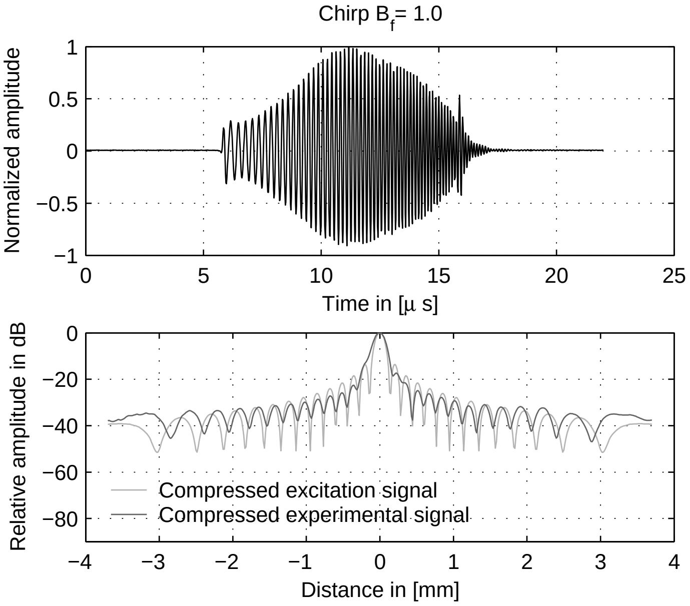

Figure 2.17: Top: Signal received from a wire target at focus for a chirp excitation signal with fractional bandwidth $B_f = 1.0$. Bottom: Compressed experimental signal and comparison with the compressed excitation signal.

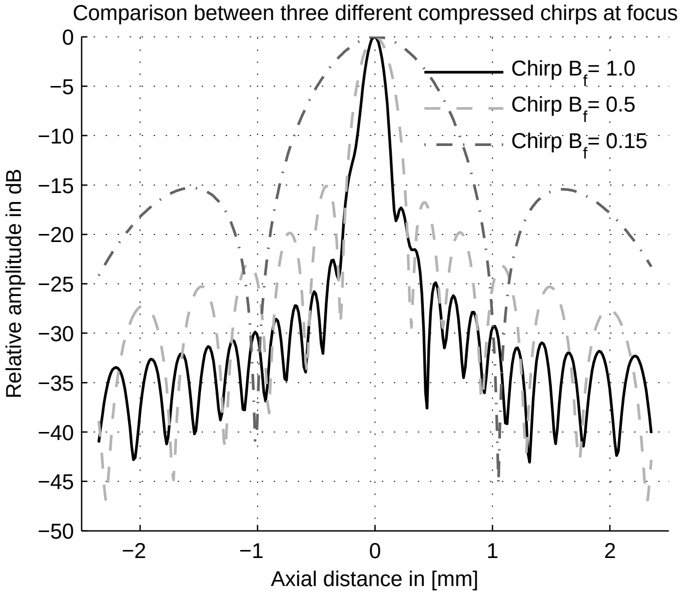

Figure 2.18: Comparison of the mainlobes and primary sidelobes for the three different chirps after compression (from the experimental data collected).

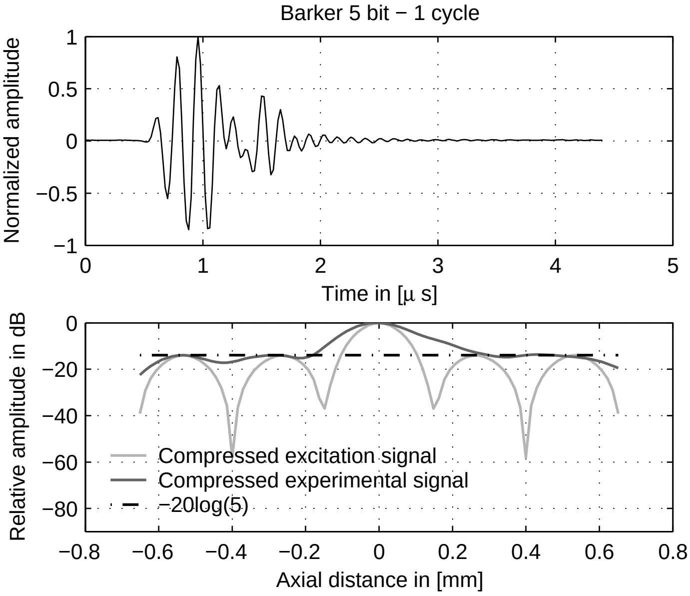

Figure 2.19: Top: Signal received from a wire target at focus for a Barker 5 bit 1 cycle excitation signal. Bottom: Compressed experimental signal and comparison with the compressed excitation signal.

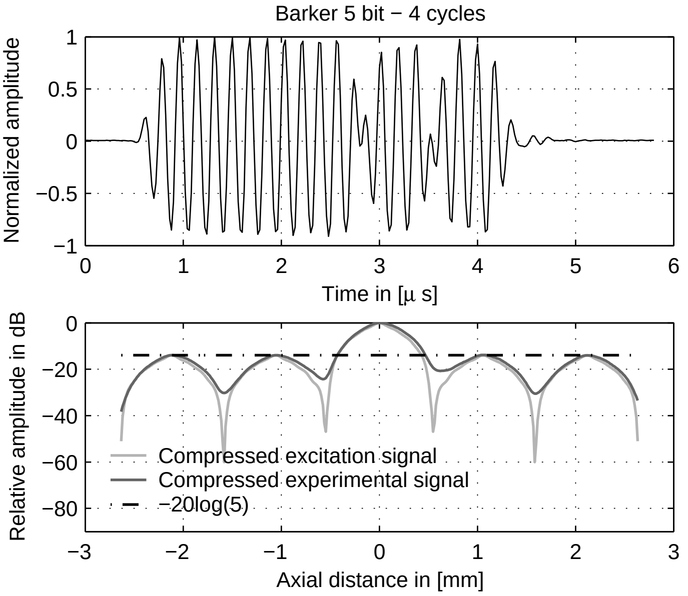

Figure 2.20: Top: Signal received from a wire target at focus for a Barker 5 bit 4 cycles excitation signal. Bottom: Compressed experimental signal and comparison with the compressed excitation signal.

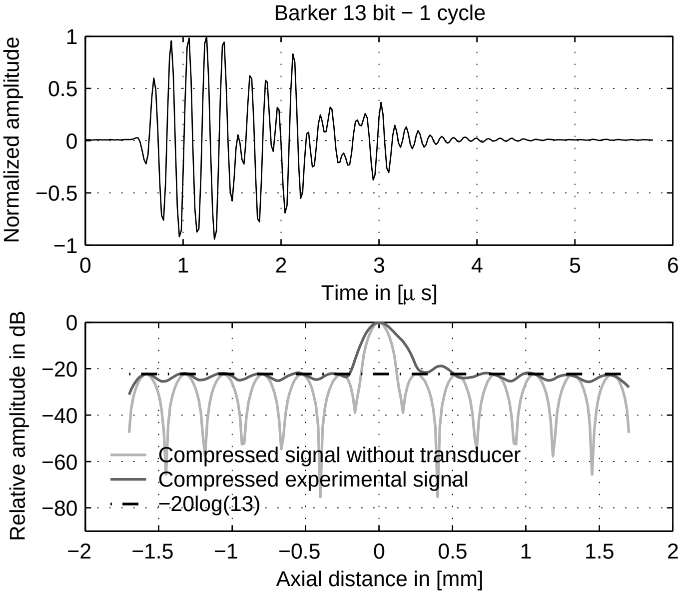

Figure 2.21: Top: Signal received from a wire target at focus for a Barker 13 bit 1 cycle excitation signal.Bottom: Compressed experimental signal and comparison with the compressed excitation signal.

Chirp	Resolution (mm)
$B_f = 1.00$	0.22
$B_f = 0.50$	0.35
$B_f = 0.15$	1.14

Table 2.3: Spatial resolution measured as the FWHM at the focus of the transducer for three different LFM chirps.

Barker code	Resolution (mm)
5 bit 1 cycle	0.25
5 bit 4 cycles	0.61
13 bit 1 cycle	0.24

Table 2.4: Spatial resolution measured as the FWHM at the focus of the transducer for three different Barker codes.

show how an ideal point scatterer can be resolved by a 2D imaging system. From a velocity estimation point of view, point spread functions are equally important because they give an idea of the sample volume, i.e. the insonified volume in which all the moving scatterers present will contribute to yield a single single velocity estimate. The point spread functions were obtained experimentally by scanning laterally the wire target (by steps of 12.5 μm) at the focus depth ($\simeq$ 50 mm) and recording the signal returned from each lateral position. This effectively gives a 2D amplitude distribution of the field at the depth of focus. Note that due to the geometry of the single element transducer used, the results can be easily translated into a 3D representation of the sample volume, by rotation around the depth axis.

Fig.2.22 shows the point spread function obtained for two conventional CF pulses of length 4 cycles and 8 cycles. The difference in axial resolution can be easily noticed, but in the transverse direction however, the two pulses yield a similar profile. Fig.2.23 shows the point spread function of the three considered compressed Barker codes. Fig. 2.24 shows the point spread functions obtained from the three different chirps. The 2D structure of the sidelobes is clearly visible. Because the chirps used in this study have a much longer duration, the structure of the sidelobes extends a lot more in the axial direction than for Barker codes. As can be seen as well by comparing Fig.2.24 and Fig.2.23, LFM chirps sidelobes can become slimmer at some points whereas in the case of Barker codes, the sidelobes structure is more regular with depth, and are much higher in amplitude. Finally, these results show that all the tested waveforms yield an equivalent lateral resolution at the focus after compression. This result is further confirmed by the following plot Fig.2.25 presenting the lateral peak amplitude pressure profile for three different waveforms. The lateral spatial resolution measured as the FWHM (-6 dB), was similar for the three different waveform (approximately 1.1 mm).

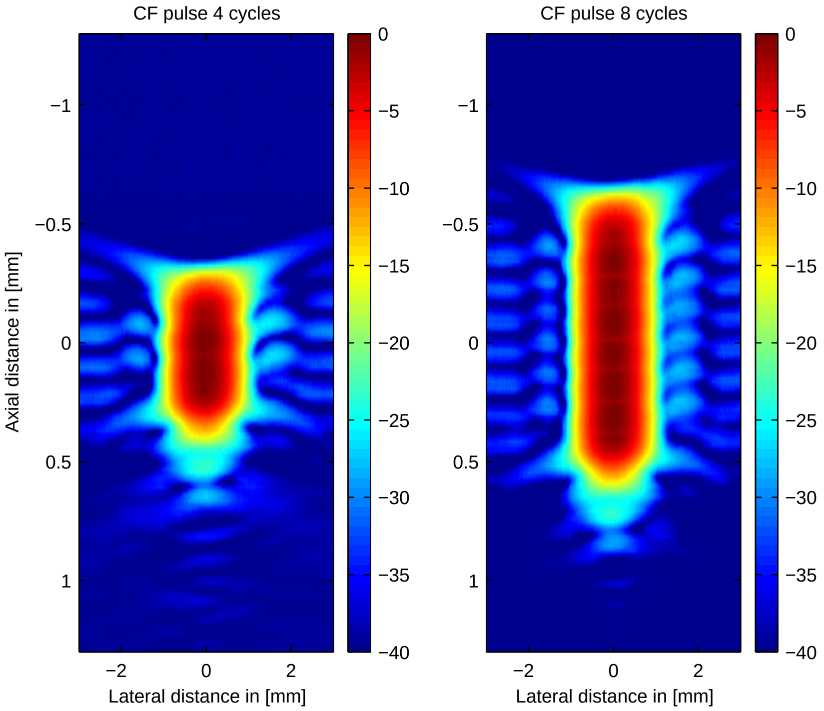

CF pulse 4 cycles

CF pulse 8 cycles

Figure 2.22: Comparison between the point spread functions of the 4 cycle and 8 cycle CF pulses. The colour scale corresponds to a relative amplitude in dB.

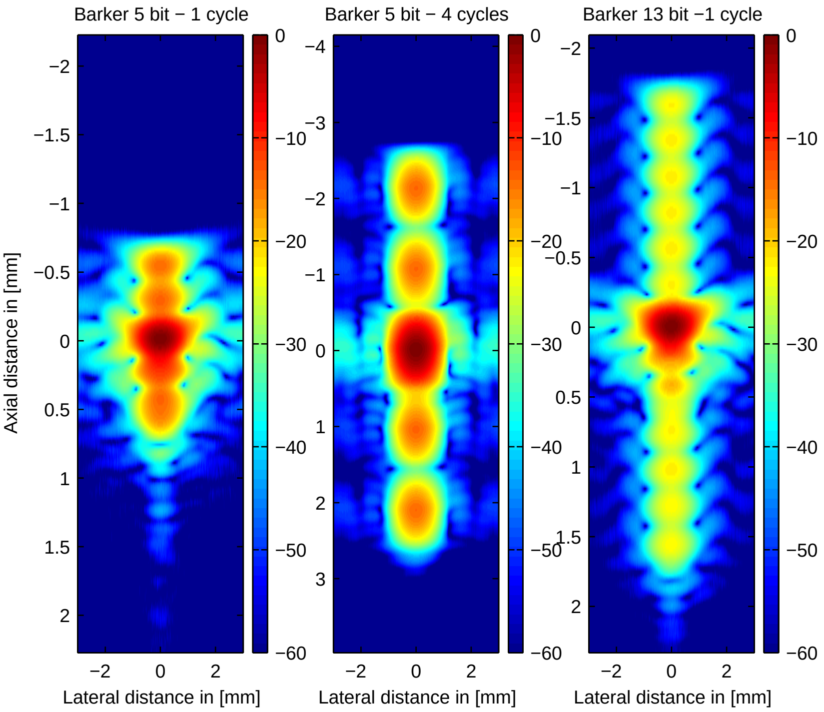

Barker 5 bit − 1 cycle

Barker 5 bit − 4 cycles

Barker 13 bit −1 cycle

Figure 2.23: Comparison between the point spread functions of the three different Barker codes.The colour scale corresponds to a relative amplitude in dB.

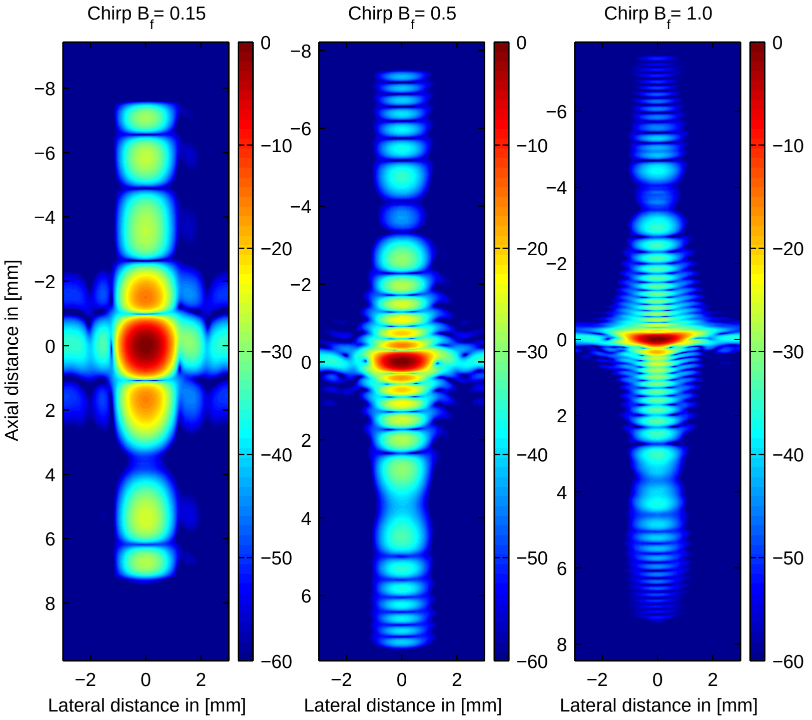

Figure 2.24: Comparison between the point spread functions of the three different chirps. The colour scale corresponds to a relative amplitude in dB.

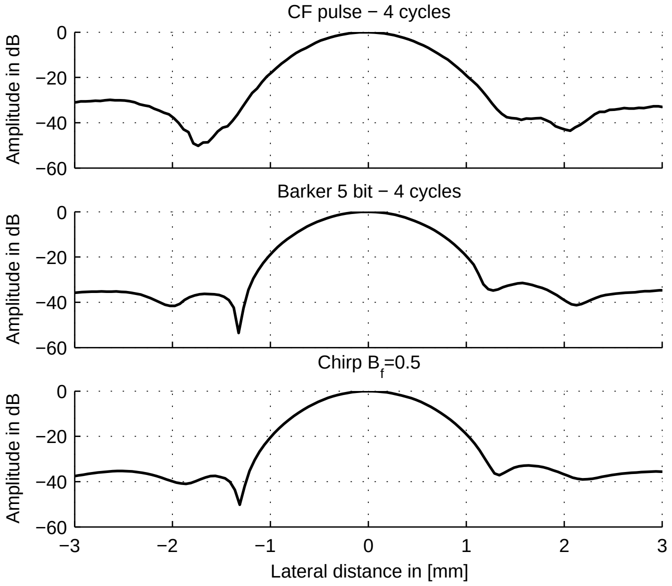

Figure 2.25: Peak amplitude in the transverse direction for a CF 4 cycles pulse, the compressed $B_f = 0.5$ chirp waveform and the compressed Barker code 5 bit 4 cycles waveforms.

2.4 Conclusion

This chapter has presented the experimental set-up and equipment used for the acquisition of signals. The impact of the transducer on the transmission of coded waveforms has been studied by pulse-echo measurements on a wire target. Three different chirp waveforms were tested (time duration of 10 μs and fractional bandwidths $B_f = 0.15$, $B_f = 0.5$, $B_f = 1.0$). The observed on-axis pulse-echo fields were very similar to those observed with conventional 4 cycles and 8 cycles CF pulses. The compressed waveforms yielded a relatively constant gain in SNR, and the values obtained were in qualitative agreement with the theoretical values for relatively narrowband waveforms (chirp $B_f = 0.15$, Barker code 5 bit 4 cycles). Some larger deviations were observed for the wideband coded waveforms (by 4 to 5 dB), which could be expected, because the transducer then transmits a less important fraction of the excitation signal energy. The compressed waveforms received at focus showed that in the case of LFM chirps, the apodisation of the excitation signals by the transducer was beneficial in terms of sidelobes level, as the fractional bandwidth of the chirp excitation signal is increased. On the contrary, for all Barker waveforms tested, the sidelobes level observed remained close to the theoretical values independently of the bandwidth of the waveform, and the length of Barker code used. The obtained axial resolutions, measured as the FWHM after compression, were correlated with the bandwidth of the transmitted waveforms (the more wideband the waveform, the better axial spatial resolution). Axial resolutions slightly below one wavelength at the centre frequency of the transducer were obtained for the most wideband waveforms. These very good figures have to be balanced with the level of the range sidelobes. In practical imaging applications, these sidelobes have to be reduced below the dynamic range of an image [24]. One of the simplest solution is to use an apodisation function on the envelope of the transmitted coded waveform. This will however reduce the axial resolution and generally, there is a well known trade-off between the level of these sidelobes and the axial resolution ([24], for instance). Finally, for all the coded waveforms tested, experimental point spread functions at the focus were obtained, which showed the 2D structure of the sidelobes for the different compressed waveforms. The 2D sidelobes pattern can largely differ for LFM chirps and Barker codes, but the lateral beam profiles of the compressed fields were observed to be very similar to that of the CF pulses, yielding a very similar lateral resolution of 1.1 mm (which is essentially governed by the transducer aperture and acoustic focus). After compression the sample volume is thus essentially modified axially, with the introduction of range sidelobes.

Chapter 3
Basic considerations in the use of coded excitation for CFI applications

The goal of this chapter is to investigate the potential improvements in spatial resolution and sensitivity that could be provided by coded excitation techniques in a typical CFI implementation. Specific differences from B-mode imaging applications in terms of pulsing strategy and safety requirements need to be taken into account. We also try to compare the relative advantages of using Barker coded signals and LFM chirps as coded excitation candidates with some quantitative figures, as well as with more qualitative aspects in terms of ease of implementation. This chapter first starts with a historical background and some general considerations on the coded excitation scheme selection. A simple model of signals for velocity estimation application is then reviewed. This model makes it possible to derive and compare the SNR conditions for conventional and coded excitation, and to discuss the potential improvement of the resolution-sensitivity trade-off. Significant differences from B-mode imaging applications will be emphasised to discuss the relevance of coded excitation for velocity estimation applications in the context of CFI. Some simulations are shown to support the statements made and to provide some quantitative figures of resolution and sensitivity improvements both for Barker codes and LFM chirps. Finally, some more practical aspects such as the additional system complexity and sidelobe reduction required by coded excitation techniques are discussed in the last section.

3.1 General considerations

3.1.1 Historical perspectives and literature review

The idea of using coded excitation schemes to improve the sensitivity of ultrasonic Doppler flowmeters can be traced back to the early seventies. Cobbold [28] reports two studies presented in conferences from a Japanese team in 1970, where the possibility of using binary sequences to monitor heart velocities is investigated [32, 33]. The same authors also published a journal paper on the same topic a bit later on [34]. In 1972, Waag demonstrated a prototype system measuring the cardiac chamber flow using pseudorandom binary sequences. A bit later on, a set of papers [35, 36, 37], reported systems for blood flow measurement based on the transmission of broadband random noise bursts. These techniques were similar in principle to coded excitation techniques. The authors provided a theoretical analysis of the systems, while pointing out the main advantages of the technique in the light of the limitations of conventional Doppler pulsed systems. These are essentially:

- the range resolution of a conventional pulse Doppler system is limited by the length of the transmitted pulse: a short pulse provides a good resolution but the average (temporal) transmitted intensity is then limited, which implies relatively poor SNR conditions. This loss in sensitivity can only be compensated by the transmission of larger peak intensities up to a certain limit, for safety reasons.
- pulse Doppler systems also have an inherent range/ maximum detectable velocity product limitation.

The studies demonstrated that with random signal flowmeters, the resolution is only constrained by the bandwidth of the transmitted pulse and not any more by their time duration which allows the transmission of long signals providing a good sensitivity. Moreover, it was shown that the proposed systems did not suffer from the range / velocity ambiguity observed with conventional sinusoidal bursts. It is here worthwhile to mention that these early coded excitation systems were introduced in their historical context a few years after the introduction of pulsed Doppler systems by Peronneau [8] and Baker [9]. The output of such devices at the time was still essentially Doppler spectra. Velocity profiles with multi-gate systems were only to appear a few years later [38] and real-time CFI systems even later [39]. Cathignol et al. developed a new approach in 1980 with the use of circular M-sequences [40], their pseudo-random signal Doppler flowmeter was commercialised. The authors claimed an increased of 20 dB in the SNR with their system. A few laters later, however, the same team of researchers published an article dealing with some limitations of their system due to clutter signals [41]. They also pointed out that in pseudo-random Doppler systems, the transmitted power is not limited by the peak power but by the heating effects, which limits the gain in SNR to 10 dB in practise.

In parallel to these works, McCarty [42] proposed a CW Doppler system with a repetitive linear frequency modulation of the transmitted signals, the underlining idea was to try to solve the lack of range resolution of a CW device by "encoding" depth with frequency. This approach was extended later on by Wilhjelm [43, 44] to yield a new velocity estimation approach based on LFM chirps. It seems that apart from the work of Wilhjelm, the use of coded excitation for Doppler application was not considered much further from the late eighties to the beginning of the 21st century. With the renewed interest for this technique in the late nineties, a few patents were published for the use of coded CFI systems. A patent was proposed for the use of single codes [45], two patents deal with CFI systems based on the use of Golay codes [46, 47]. Zhao [26] gave some practical and theoretical considerations for the design of a CFI system based on Barker codes. Some authors have also recently proposed new systems for CFI based on a more complex use of linear arrays, where different elements are used to transmit or receive simultaneously in different focus loci [47, 48], coded excitation is then used to compensate for the loss in SNR associated with using only a few elements on transmit. Finally, Cowe et al. discussed the compression properties of LFM chirps for Doppler applications, with a specific focus on Transcranial Colour Doppler (TCD) applications [49, 50].

3.1.2 Coded excitation scheme selection and scope of this study

Coded excitation is a technique derived from the radar field, where some similar tasks of imaging and velocity estimation are performed. It is interesting, however, to stress some differences in the two different fields. Radar waveforms are usually designed to yield good correlation properties to obtain a good resolution in both range and Doppler (this is formalised through the use of the so-called ”ambiguity function”, this notion is not introduced here, since it’s barely used in the field of medical ultrasound). In medical ultrasound modern Doppler techniques, although the movement of scatterers causes a frequency shift due to the Doppler effect, the effect of frequency dependent attenuation may produce an important shift in frequency (two orders of magnitude higher than the Doppler shift [23]) which will mask the Doppler shift, (this aspect was mentioned in the introduction chapter). In general, blood or even tissue velocity estimation can thus not be performed using a single measurement relying on the mean frequency shift. The estimators rely instead on the shift in time or in phase that the returned signals experience over several (at least two) pulse transmit-receive cycles. Misaridis pointed out in [24] that there is therefore *a priori* no need to retain a good resolution in the Doppler axis for the the selection of the transmitted coded waveform.

In this chapter, two types of waveforms will be investigated, the LFM chirps and Barker codes. LFM chirps have already proved to have interesting properties for imaging applications[22, 23, 24], but seem to have been less studied in the field of velocity estimation apart from the work of Wiljelhm [43, 44]. Misaridis suggested to use uncompressed LFM chirps for blood flow velocity estimation and noted that applying a phase-shift flow estimator on the uncompressed data could be theoretically possible, but the effect of the varying frequency of the signal on the estimator would have to be investigated [24]. In fact, as will be seen, compressing of the pulse at the receiver seems to be essential to restore the resolution of the pulse, long coded excitation pulses would otherwise yield extremely wide sample volumes. One of the problems that arises when compressing the waveforms at the receiver are the generated sidelobes, but the requirements for the sidelobes level may not be identical to those for imaging conditions, this will be discussed later in section 3.5.2. Zhao[26] has recently proposed an effective scheme to perform CFI with Barker codes with reduced sidelobes, and pointed out the relative simplicity of the use of these coded waveforms. It is interesting to note that the use of Golay codes could solve the problem of sidelobes in theory, but this technique requires some degree of stationarity between pulses transmits of the complementary codes for a good compression. This type of coded excitation thus requires some specific signal processing techniques if to be used for velocity estimation. As previously mentioned, schemes based on Golay codes to perform CFI were proposed in a patent [51]. Other pseudo-random binary sequences are also theoretically possible. We will however restrict our scope to the simpler cases of Barker codes and LFM chirps, and will try to compare the relative advantages of these two types of waveforms.

Finally, although advanced new CFI imaging approaches are possible using coded excitation (for instance, [48]), this chapter is primarily concerned with a “classical” CFI implementation, with a phase shift based estimator. The goal is to see what could be the potential advantages of using coded waveforms instead of CF pulses in a typical current scanner CFI implementation.

3.1.3 Model of the SNR conditions at the receiver and improvement by coded excitation

Carrying on with the comparison with radar applications, the useful received signals in a radar system usually consist of distinct echo signals from targets resolved by the imaging system (note however that in radar systems, an additional clutter signal component is often present and in weather radar, the clutter signal is the signal of interest). In these situations, it is known that the matched filter maximises the SNR at the receiver, in the presence of additive white stationary noise (see for instance, [16]). The SNR in this case is taken as the ratio of the peak power of the received echo with the average noise power:

$$\mathrm{SNR} = \frac{\mathrm{Target\ signal\ peak\ power}}{\mathrm{Average\ noise\ power}} \tag{3.1}$$

With the use of coded excitation, the SNR at the output of a matched filter can approximately be increased by a factor equal to the time duration-bandwidth product of the transmitted coded waveform, without sacrificing the spatial resolution or increasing the transmitted peak amplitude. This has been the basis for using coded excitation in B-mode imaging applications, to improve the depth of penetration, without compromising patients safety. In CFI applications, the received signals used to infer velocities are formed by incoherent scattering of ultrasound from a large number of randomly located scatterers which are not resolved by the system (so-called "speckle" signals). The SNR conditions can thus no longer be adequately described by Eq.3.1 and need to be treated with an adapted model. The next section reviews a simple signal model from which the SNR conditions will be derived and the possible improvements in sensitivity and resolution with coded excitation will be discussed.

3.2 Review of a model of the SNR conditions and influence of the filter at the receiver in the case of incoherent scattering

3.2.1 Review of a simple model of the backscattered signals from blood

The speckle signals used to infer the velocities of blood and tissues in medical ultrasound are likely to arise from a complex interaction between the ultrasound waves and the microscopic structure of the propagating medium. From a model point of view, speckle signals can be described by the summation of the individual backscattered signals from a large collection (at least, a large number in a cube of side length equal to a wavelength) of randomly located point-like scatterers. In a continuous description of the propagating medium, incoherent scattering arises from random fluctuations of the compressibility and density properties of the medium, with a correlation length much smaller than a wavelength. Several studies have dealt with the stochastic properties of the backscattered signals from blood, based either on a discrete or "continuum" approach (see for instance, [52, 53, 54, 55, 56]).

The amplitude of signals at the receiver may vary significantly with the depth of return because of the spatially variant point spread function of ultrasound transducers, and effects of propagation such as attenuation. The stochastic process to be modelled is thus *a priori* not stationary. However, the hypothesis of stationarity can be made if the signal is observed for a short period of time, like the duration of the typical gated range windows used for velocity estimation (of the order of one microsecond). For the purpose of analysis, the non-stationary process at the receiver can then be replaced by a stationary process having the same statistical properties (in particular same variance, or average power) as locally, in a range gated window at a given depth. A common approach to model the signals is to regard the stochastic process as the output of a linear filter excited by noise (the random fluctuations in compressibility and density from which backscattering arises), and impulse response, the transmitted signal. A theoretical justification was for instance given by Kristoffersen in [57], based on Angelsen's theory of blood backscattering [55].

The received signal process $x(t)$ from a given depth can then be modelled as:

$$x(t) = \int s(\tau) f_{scat}(t-\tau) d\tau, \tag{3.2}$$

where $s(t)$ is the transmitted signal, f_{scat} is a noise-like scattering function. In particular, we have the property:

$$< f_{scat}(t) f_{scat}(t+\tau) > \approx k_s \delta(t-\tau), \tag{3.3}$$

where $<>$ denotes time averaging, k_s is a constant characterising the transducer transmit/receive sensitivity function at a given depth, and the average backscattering power of blood. The process is then characterised by its autocorrelation function:

$$< x(t) x(t+\tau) > \approx k_s \int_{-\infty}^{+\infty} s(t) s(t+\tau) dt \tag{3.4}$$

Note that k_s has the dimensions of the inverse of a time in this expression. In particular, substituting $\tau = 0$ in Eq.3.4 shows that in the absence of filtering at the receiver, the average power received is proportional to the energy of the transmitted signal, through this coefficient:

$$< x(t)^2 >= k_s E, \tag{3.5}$$

where E is the energy of the transmitted signal. The power spectral density $P(f)$ of the stationary signal can also be found by taking the Fourier transform of Eq.3.4:

$$P(f) = k_s |S(f)|^2, \tag{3.6}$$

where $S(f)$ is the Fourier transform of the transmitted signal. In the following, we will use this stationary model to derive the SNR conditions at the receiver after a filter.

3.2.2 Influence of the receiving filter

The filter at the receiver has a major impact on the SNR conditions, since it aims at rejecting noise from the useful signal bandwidth. Denoting by h the impulse response of the filter, x the received signal process, and n, the system thermal noise process, the SNR conditions are given by:

$$\mathrm{SNR} = \frac{< (x \otimes h)^2 >}{< (n \otimes h)^2 >}, \tag{3.7}$$

A simple model of the SNR conditions at the receiver can equivalently be formulated in the Fourier domain. The thermal noise mainly arises from the transducer and the amplification system, and its spectrum can usually be considered as flat over the bandwidth of the signal. Let us assume a constant noise power density $N_0/2$ in (W/Hz). Let us further assume that the filter at the receiver has a frequency response $H(f)$. With the help of Eq.3.6, the SNR at the receiver is then characterised by:

$$\mathrm{SNR} = \frac{2\int P(f)|H(f)|^2 df}{\int N_0 |H(f)|^2 df} = \frac{2k_s \int |S(f)|^2 |H(f)|^2 df}{N_0 \int |H(f)|^2 df}. \tag{3.8}$$

This is essentially the expression obtained by Kristoffersen [57, (34)], with k_s normalised to one. This expression is hard to work with unless the spectral shape of the filter and the signal have a simple analytic form. In the next section, we will examine the specific case of a matched filter at the receiver.

The receiver filter also plays a major role in the spatial resolution of a system. The axial size of the sample volume of a pulsed Doppler system is determined by the shape of the received echo envelope from a point scatterer, as observed at the output of this filter. If $h(t)$ is the impulse response of the receiver filter, then the axial amplitude weighting of the sample volume $w(t)$ is given by [57]:

$$w(t) = Env\left\{\int s(\tau)h(t-\tau)d\tau\right\}, \tag{3.9}$$

where Env denotes the operation of extracting the envelope of a signal.

3.2.3 Case of a matched filter at the receiver

Let us first derive the SNR expression in the particular case when a matched filter is used at the receiver. The frequency domain expression of a matched filter is given by [16]:

$$H(f) = k.S^*(f)\mathrm{e}^{-j2\pi f\tau_d}, \tag{3.10}$$

where k is a constant amplitude factor and τ_d is a constant delay to make the filter causal. Substituting $H(f)$ in Eq.3.8 is straightforward and leads to:

$$\mathrm{SNR} = \frac{2k_s \int |S(f)|^4 df}{N_0 \int |S(f)|^2 df}. \tag{3.11}$$

In terms of spatial resolution, the weighting axial amplitude of the sample volume can be obtained with the time domain impulse response of the matched filter [16]:

$$h(\tau) = k.s(\tau_d - \tau). \tag{3.12}$$

Substituting in Eq.3.9 shows that in the case of a matched filter the axial weighting amplitude of the sample volume is the autocorrelation envelope of the transmitted pulse.

3.2.4 Optimality of the matched filter

The optimality of the matched filter in terms of SNR is not guaranteed from the previous expressions. The reader is referred to Kristoffersen' paper [57] for a discussion on the optimality of the receiving filter. In the context of coded excitation, it seems essential to use a matched filter (or any decoding filter combined with a bandpass filter to reject noise) to restore the axial length of the sample volume down to approximately the inverse of the bandwidth, (neglecting the sidelobes of the compressed waveform). The long coded signals would otherwise yield sample volumes with a very large axial length. In a conventional CFI implementation, the received signals are usually summed in a range gate of duration T_r after quadrature amplitude demodulation. This can be understood as applying a real pure averaging filter of impulse response:

$$h(t, T_r) = \begin{cases} 1 & t \in [0, T_r] \\ 0 & \text{elsewhere} \end{cases}, \tag{3.13}$$

on the complex demodulated data (and retaining only one value per gated range window). In the case of conventional pulses with a rectangular amplitude envelope, if T_r is chosen equal to T_p, the duration of the transmitted signal, the effects of the averaging filter on the baseband data and matched filter are identical in terms of SNR and resolution. In particular the obtained weighting (normalised) axial function of the sample volume is a triangular function given by:

$$w(t) = \begin{cases} 1 - |t/T_p| & |t| < T_p \\ 0 & \text{elsewhere.} \end{cases} \tag{3.14}$$

In this case again, the axial length of the sample volume, for instance taken as the full width at half maximum (FWHM) is equal to $T_p \approx 1/B$, that is, approximately to the inverse of the bandwidth of the conventional pulse used.

3.3 SNR conditions comparison for coded and conventional CF pulses after a matched filter

In this section, we compare the SNR conditions when a conventional and a coded pulse are used, with a matched filter at the receiver. For further simplification, the spectra of the transmitted pulses are assumed to be square. As such, the LFM is chirp a is good candidate for the coded pulse. For the conventional pulse, a sinc envelope CF pulse is used. The normalised sinc envelope function is given by:

$$\mathrm{sinc}(Bt) = \begin{cases} \dfrac{\sin(\pi Bt)}{\pi Bt} & t \in \mathbb{R}^* \\ 1 & t = 0 \end{cases}, \tag{3.15}$$

where B is the bandwidth of the pulse (in Hz). This waveform is not causal and is never used in practice but has the good spectrum property (rectangular spectrum of width B) and will be used here for discussion purposes only. We also use the fact that for a modulated waveform with a rectangular spectrum and centre frequency f_0, $|S(f)|^2$ is a constant in the bandpass and is equal to :

$$|S(f)|^2 = \begin{cases} \dfrac{E}{2B} & |f - f_0| < \dfrac{B}{2} \\ 0 & \text{elsewhere.} \end{cases}. \tag{3.16}$$

Substituting and integrating in Eq.3.11 yields:

$$\mathrm{SNR} = \frac{k_s E}{B N_0}. \tag{3.17}$$

3.3.1 Case of conventional CF pulses

For a conventional CF pulse the energy is given by:

$$E = \frac{1}{2} A^2 T_p, \tag{3.18}$$

where A is the amplitude of the CF pulse (assumed to be constant) and T_p is its time duration. We can further use the relationship $B \approx 1/T_p$ (the time-bandwidth product of a CF pulse is of the order of one) to obtain:

$$\mathrm{SNR} = \frac{k_s A^2 T_p}{2 B N_0} \approx \frac{k_s A^2}{2 B^2 N_0}. \tag{3.19}$$

Note that in the case of a sinc envelope pulse the relationship $E = \frac{A^2}{2B}$ holds exactly, so substituting in Eq.3.17 shows that Eq.3.19 is rigorous in this particular case. We thus see that the SNR conditions are heavily dependent on the bandwidth B of the pulse, as a function of $1/B^2$. This relationship also illustrates the severe trade-off between resolution and sensitivity for velocity estimation in ultrasound.

3.3.2 Case of coded excitation

In the case of an LFM chirp, the same analysis can be performed except that the time-bandwidth product of the waveform can be set to any arbitrary value greater than one. We thus obtain:

$$\mathrm{SNR} = \frac{k_s A^2 T_p}{2 B N_0}, \tag{3.20}$$

where this time, T_p is the time duration of the chirp and B is its bandwidth. This shows that in the case of coded excitation the SNR varies as $1/B$.

3.3.3 Improvement in SNR

If the coded signal and the CF pulse to be compared have the same peak amplitude A (yielding the same transmitted peak intensity) and the same bandwidth B, the improvement in SNR is obtained by the ratio of expression Eq.3.19 and expression Eq.3.20. The gain in SNR is thus equal to:

$$\mathrm{GSNR} = T_p B, \tag{3.21}$$

where T_p is the time duration of the chirp and B is the bandwidth of the chirp and the sinc pulse. We thus arrive to the classical result in radar theory that the improvement in SNR due to using coded excitation is equal to the time-bandwidth product of the coded waveform, re-derived here in the case of incoherent scattering.

3.3.4 Validation with simulations

Synthetic RF speckle signals modeling the statistical and spectral characteristics of the received signals in a given gated range window can be obtained by convolving an excitation signal e with a Gaussian white noise realization n_1, following the signal model of section 3.2.1. To model thermal noise at the receiver, a second independent white (all pass) Gaussian noise n_2 is then added:

$$r = e \otimes n_1 + n_2, \tag{3.22}$$

where $\otimes$ denotes convolution. For all the simulations presented in this thesis, the centre frequency f_0 used was set to 5 MHz, and the sampling frequency was set to 50 MHz. To validate the SNR models derived in section 3.3 Eq.3.20 and Eq.3.19 with the assumption of square spectral density functions, a synthetic speckle $r(t)$ signal was first generated according to Eq.3.22 using a sinc pulse excitation signal $e(t)$ with a given fractional bandwidth B_f:

$$e(t) = \mathrm{sinc}(B_f f_0 t)\sin(2\pi f_0 t). \tag{3.23}$$

This signal was sampled for $t \in \left[-\frac{10}{B_f f_0}, +\frac{10}{B_f f_0}\right]$. In the case of coded excitation, the LFM chirp excitation signal is given by:

$$e(t) = \sin\left(2\pi f_0 \left[\left(1 - \frac{B_f}{2}\right)t + \frac{B_f}{2T_p}t^2\right]\right) \quad t \in [0, T_p]. \tag{3.24}$$

The SNR at the output of a matched filter were computed in time domain, as:

$$\mathrm{SNR} = \frac{<(e \otimes n_1 \otimes h_{matched\,filter})^2>}{<(n_2 \otimes h_{matched\,filter})^2>}, \tag{3.25}$$

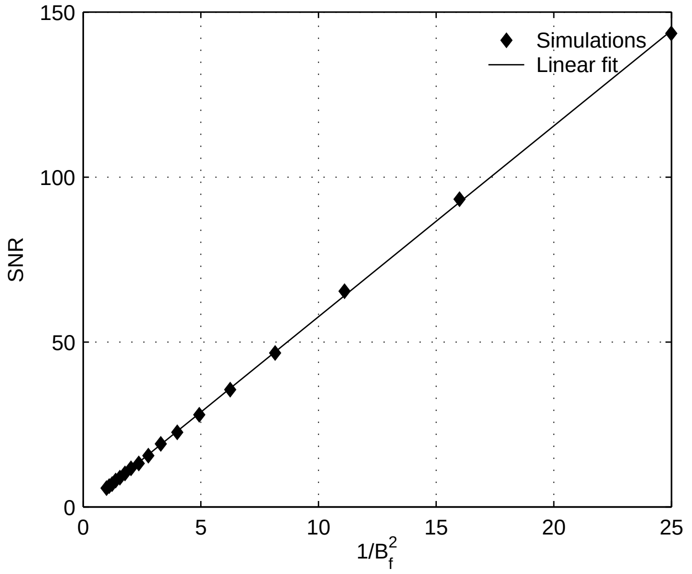

Figure 3.1: Plot of the SNR conditions after a matched filter as a function of the squared inverse of the fractional bandwidth for a sinc envelope CF pulse.

where $h_{matched\,filter}$ is the impulse response of the matched filter associated with either the sinc pulse or the chirp ($h_{matched\,filter} = e(\tau_d - t)$). The operation was repeated while varying the fractional bandwidth of the pulse from 0.2 to 1. All the signals generated to compute the SNR values were 100 000 samples long (chosen to obtain statistically reliable results. The results obtained are plotted in Fig.3.1 and Fig.3.2 (the SNR range conditions on the y-axis were chosen arbitrarily). There is a very good agreement with the expected relationship between the SNR conditions and the bandwidth. The graph in Fig.3.3 also shows the resulting gain in SNR and the theoretical curve Eq.3.21, again a very good agreement is shown.

3.4 Potential improvement in sensitivity and resolution

3.4.1 Improvement in the SNR conditions

The preceding equations show that an improvement in SNR is possible for velocity estimation applications provided a coded waveform with a significant time-bandwidth product can be achieved. The obvious potential benefits of such of an improvement is to increase the threshold of detectability of flows in deep-lying regions or for “technically difficult” patients. However, the situation differs significantly from normal imaging conditions. Coded excitation is an attractive solution for B-mode imaging applications because the rarefaction peak pressure intensity

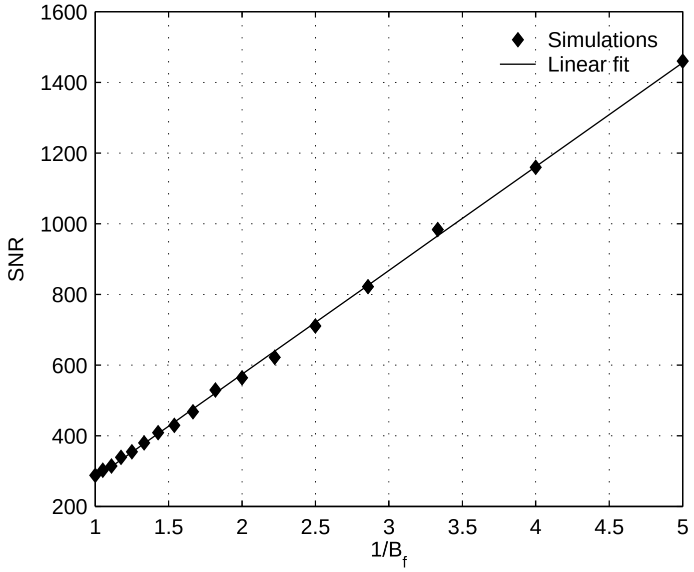

Figure 3.2: Plot of the SNR conditions after a matched filter as a function of the inverse of the fractional bandwidth in the case of coded excitation (chirp of duration $T_p = 10\ \mu\text{s}$).

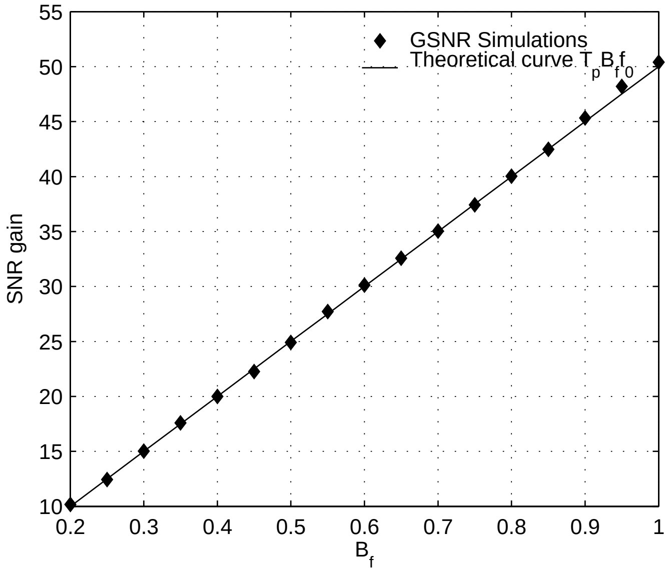

Figure 3.3: Simulated gain in SNR (GSNR) of chirps of duration $T_p = 10\ \mu\text{s}$ over sinc envelope CF pulses of the same amplitude, as a function of the fractional bandwidth, and the corresponding theoretical improvement ($T_p B_f f_0$).

is the limiting factor to achieve a better SNR for patients' safety. For typical CFI implementations using phase domain velocity estimation, long (narrowband) pulses are transmitted which already provide a relatively good SNR. The margin of improvement with coded excitation is thus limited compared to the case of the high resolution pulses used for imaging. Moreover, as large packet size (number of pulses transmitted in the same direction) are transmitted in a rapid interval (the pulse repetition frequencies required for velocity estimation are at least one order higher in magnitude than a typical B-mode imaging frame rate), heating effects may be the major limitation to increasing the sensitivity for these applications, rather than peak intensity limitations. In terms of acoustic output, this means that the average transmitted intensity may often be bounded for CFI. The intensity considered here is more precisely the spatial peak pulse average intensity, defined by [13] :

$$I_{spta} = \frac{1}{T_s} \int_0^{T_p} I_i(t, \mathbf{r_{max}}) dt, \tag{3.26}$$

where $\mathbf{r_{max}}$ is the position of maximum intensity, T_s is the pulse repetition period, and $I_i(t, \mathbf{r})$ is the instantaneous intensity. Jensen [13, pp.21-22] gives the example of a burst pulse of length T_p propagating as a plane wave in water with a constant pressure p_0. The peak intensity is then given by $I_{sptp} = \frac{p_0^2}{2Z}$, where Z is the characteristic impedance of water ($Z = 1.48\ \mathrm{kg}/[\mathrm{m}^2.\mathrm{s}]$). This yields the average intensity:

$$I_{spta} = \frac{1}{T_s} \int_0^{T_p} \frac{p_0^2}{2Z} dt = \frac{p_0^2}{2Z} \frac{T_p}{T_s}. \tag{3.27}$$

In the general case, the transmitted pulse amplitude is limited by either the demand in peak intensity I_{sptp} or by the demand in average intensity I_{spta}. Jensen has discussed these intensity limitations for CFI systems [13, pp.219-222], while pointing out that no definitive general conclusion could be drawn. However, in the situations when the average intensity limit I_{spta} is reached for a given pulsing strategy (a given pulse repetition period, frame rate, and packet size), the total energy of the transmitted pulse is bounded (the term $p_0^2 T_p / 2Z$ cannot be increased in Eq.3.27) and thus, coded excitation may not be used for any sensitivity improvement.

3.4.2 Sensitivity/Resolution trade-offs

CFI implementations are known to suffer from a sensitivity/resolution trade-off: long narrowband pulses provide good SNR conditions but have intrinsically a poor spatial resolution. Coded excitation solutions have been proposed to enhance this trade-off (transmitting wideband codes for a good resolution while maintaining a good sensitivity thanks to the gain in SNR provided by the technique). Chiao [17] pointed out that unlike B-mode imaging, CFI systems typically operate close to the average intensity limits, and reasoned that further penetration improvement using coded excitation is generally not feasible; only resolution and frame-rate improvements may be possible.

The critical quantity for analysing the spatial resolution in CFI systems is the extent of the region in space over which different scatterer velocity contributions are averaged in a single velocity estimate (the "sample volume" size), this constrains the spatial resolution of the inferred velocity distribution. After a matched filter, the axial length of the sample volume depends on the bandwidth of the transmitted pulse as discussed in section 3.2.3. It can be clearly seen from the previous expression Eq.3.17 that if the conventional pulse and the coded pulse have the same energy (same average transmitted intensity), an increase of the bandwidth (resolution) *via* coded excitation will yield a decreased SNR:

$$\mathrm{GSNR} = \frac{\mathrm{SNR}_{coded}}{\mathrm{SNR}_{conv}} = \frac{k_s E/N_0 B_{coded}}{k_s E/N_0 B_{conv}} = \frac{B_{conv}}{B_{coded}} < 1. \tag{3.28}$$

Thus, coded excitation provides a more flexible sensitivity/resolution trade-off only if the energy of the coded waveforms can be increased compared to a given reference conventional pulse.

Fig.3.4 sums up the trade-off between resolution and SNR conditions in a more synthetic way, when both type of excitation signals have the same peak amplitude (i.e. same peak intensity), from the expressions of the previous section. Consider a typical narrowband CF pulse of fractional bandwidth $B_f = 0.2$, this pulse provides SNR conditions arbitrarily set to 14 dB. This CF pulse has a duration $T_{ref} = 1/0.2f_0$. The solid light grey curve curve shows the decrease in SNR if the bandwidth of this pulse is increased (dependence as $1/B^2$ from Eq.3.19). Alternatively, the medium grey curve corresponds to the SNR provided by a coded signal with the same peak amplitude and duration T_{ref}, as given by Eq.3.20. We can see that increasing the bandwidth to yield a better spatial resolution will yield poorer SNR conditions. Note that the curve was not plotted for a fractional bandwidth less than $B_f = 0.2$ since in this region the corresponding hypothetical waveform would have a time-bandwidth product inferior to one, which is not realisable. In the case when the coded waveform is longer than the considered reference pulse ($2T_{ref}$ and $5T_{ref}$, for the dark grey and the black lines respectively), we see

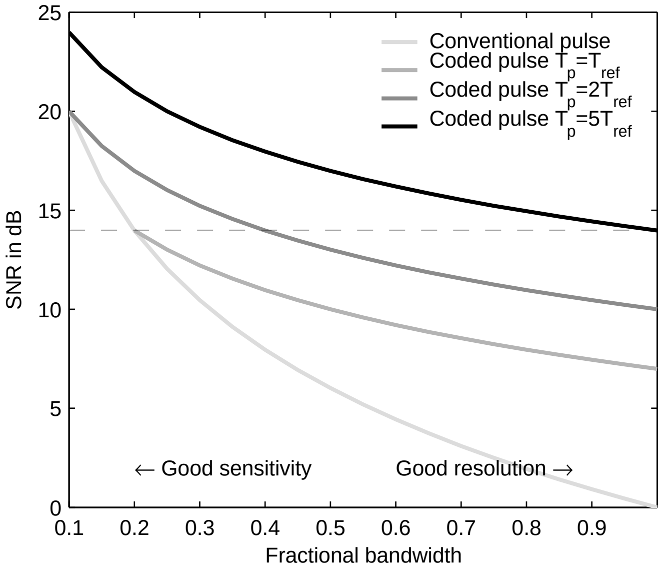

Figure 3.4: Illustration of the Resolution / SNR trade-off for coded pulses and conventional CF pulses with square spectra, and for a constant excitation signal peak amplitude.

that coded excitation offers a more flexible trade-off, the spatial resolution of the waveform can be improved (up to $B_f = 0.4$ and $B_f = 1.0$ respectively) without any loss in SNR, but the transmitted energy (and thus the average transmitted intensity) has been increased by factors of 2 and 5, respectively. This corresponds to the theoretical cases of waveforms with a square spectra (section 3.3). In practise, the transmitted waveforms don't have a rectangular spectrum, and an increasing fraction of the energy of an excitation signal is lost as its bandwidth is increased, due to the limited bandwidth of the transducer. This will be investigated in the next subsection with simulations.

3.4.3 Sensitivity and resolution study with simulations

This subsection aims to better quantify the resolution/ sensitivity trade-offs with some fairly realistic waveforms and simulation parameters. In practise, CF pulses of different lengths can be used for velocity estimation depending on a particular application. In this study, we used CF pulses ranging from 4 cycles to 12 cycles. To study the potential improvement in resolution and sensitivity by coded waveforms, SNR values were compared after a matched filter for the different CF pulses and two types of coded waveforms: LFM chirps and Barker codes. For all the simulations, the hypothesis was made that the energy of the transmitted signal could be increased (increase in average intensity tolerated), the peak intensity was thus the limiting factor for SNR improvement and all the excitation signals were scaled to yield the same peak amplitude. The excitation signal was obtained with (3.24) for LFM chirps. Barker coded excitation signals were obtained by convolving a CF pulse of a given length in cycles with the corresponding "oversampled" baseband Barker codes, as the procedure described in section 1.2.3 (based on [17]). The model used for the synthetic RF speckle signals is similar to the previous section, except that it takes in to account the effect of a transducer, i.e. the excitation signals e were convolved with a synthetic transducer's two-way impulse response h_{tran} (modelled as sinusoidal Gaussian amplitude pulse, with a -6 dB fractional bandwidth of 0.5 and centre frequency $f_0 =$ 5 MHz), to yield s:

$$s = e \otimes h_{tran}, \tag{3.29}$$

and then similarly to Eq.3.22), and to Eq.3.25, the received signal r and the SNR values were obtained from:

$$r = s \otimes n_1 + n_2, \tag{3.30}$$

$$\mathrm{SNR} = \frac{< (s \otimes n_1 \otimes h_{matched\,filter})^2 >}{< (n_2 \otimes h_{matched\,filter})^2 >}. \tag{3.31}$$

The SNR gain in dB is then computed from:

$$\mathrm{GSNR} = 10\mathrm{log}(\mathrm{SNR}_{coded}/\mathrm{SNR}_{conv}). \tag{3.32}$$

3.4.3.1 Case of LFM chirps

Fig.3.5 shows the results obtained for chirps of duration $T_p = 10$ μs, and different fractional bandwidths. For reference, one cycle lasts 0.2 μs at 5 MHz. As can be seen, the gain in SNR provided by the different LFM chirps severely depends on their bandwidth (and thus on their spatial resolution). For instance, a 10 μs LFM chirp of 100% fractional bandwidth provides a very good spatial resolution but is unable to provide any gain in SNR over CF pulses longer than 7 cycles.

To further elucidate the sensitivity/resolution trade-off, Table 3.1 compares the resolution of the different chirps and the corresponding gain in SNR they achieve over an 8 cycle CF pulse (duration 1.6 μs). The resolution was measured as the FWHM of the matched filtered pulse envelope. For reference, the chirp $B_f =$ 0.15 and the 8 cycles CF pulse have similar bandwidth and resolution (1.3 mm). The table also reports the increase in the transmitted signal energy over an 8 cycles CF pulse. An increase in sensitivity and resolution is shown with the chirp

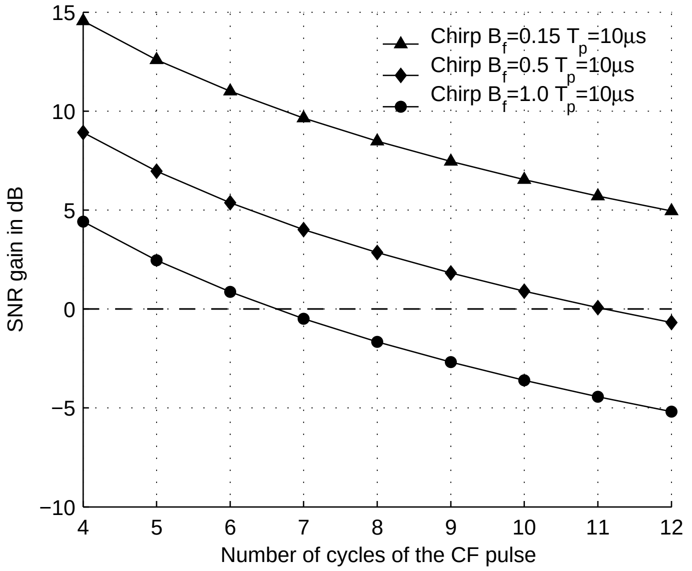

Figure 3.5: Sensitivity improvement provided by chirps of different fractional bandwidths over CF pulses of different lengths in cycles, for the same excitation signal amplitude.

Chirp	Res.(mm)	GSNR (dB)	Energy increase
$B_f = 1.00$	0.26	-1.6	3.7
$B_f = 0.50$	0.42	2.9	5.3
$B_f = 0.15$	1.34	8.5	6.1

Table 3.1: Resolution/ Sensitivity improvement/ Increase in energy over an 8 cycles CF pulse/ Comparison for 3 LFM chirps of duration 10 μs. The 8 cycles reference CF pulse has a spatial resolution of 1.3 mm.

$B_f = 0.5$, but the price to pay is an increase in the average transmitted intensity by approximately a factor of 5 compared to the 8 cycles CF pulse (for a similar pulsing strategy). Note that the obtained gain in SNR is relatively small ($\approx$ 3 dB). The gain in SNR provided by a chirp waveform can be arbitrarily increased without compromising the spatial resolution just by increasing the time duration of the waveform, which was set to 10 μs. In practice, however, several factors may bound the choice of the duration of the waveform, the more important being the limitation in the average transmitted intensity for patient safety, as discussed in subsection 3.4.1.

3.4.3.2 Case of Barker codes

Barker codes differ from LFM chirps in the fact that for these coded waveforms, the time-bandwidth product is fixed by the code used. It is possible, however, to vary the duration of

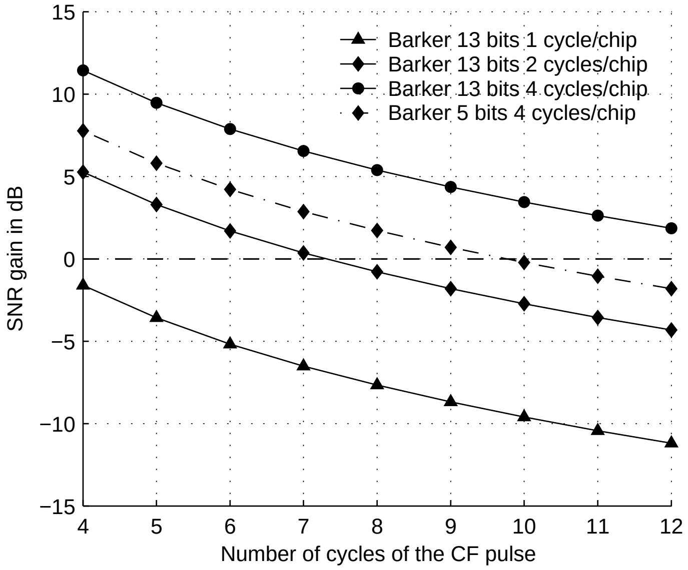

Figure 3.6: Sensitivity improvement provided by different Barker codes over CF pulses of different lengths in cycles, for the same excitation signal amplitude.

the coded waveform (and thus to increase the sensitivity), by adding several cycles per chip, but the counterpart, and contrary to the case of LFM chirps is a decreased bandwidth and resolution (so that the time-bandwidth product remains constant). Fig.3.6 shows the gain in SNR provided by different Barker codes and illustrates the sensitivity/resolution trade-off for this type of coded waveform. Table 3.2 gives more insights into the resolution. As can be seen, a 13 bits Barker code with 1 cycle per chip does not provide any gain over CF pulses longer than 4 cycles, although this waveform has an excellent resolution. The energy of this waveform after convolution by a transducer's impulse response is only 90% of the reference 8 cycles CF pulse energy. If a significant improvement in sensitivity is to be obtained, 4 cycles per chip signals have to be used, but this also bounds the maximum achievable resolution, which is then around 0.69 mm (see Table 3.2). Note again that the gains in SNR with the simulation parameters are rather limited, but the obtained gains in resolution are still very interesting for CFI, especially in relation to visualising small vessels.

Barker code	Res.(mm)	GSNR (dB)	Energy increase	T_p
13 bits 1 cycl.	0.23	-7.7	0.9	2.6 μs
13 bits 2 cycl.	0.37	-0.8	2.6	5.2 μs
13 bits 4 cycl.	0.69	5.3	6.1	10.4 μs
5 bits 4 cycl.	0.69	1.7	2.3	4.0 μs

Table 3.2: Resolution/ Sensitivity improvement/ Increase in energy over an 8 cycles CF pulse/ Length of the coded pulse, comparison for 4 Barker codes. The 8 cycles reference CF pulse has a spatial resolution of 1.3 mm.

3.5 Practical considerations

3.5.1 Hardware complexity, baseband decoding of the waveforms

Implementation of a matched filter at the receiver for CFI applications add a significant complexity to systems. It should be noticed that the length of the filter at the receiver is usually superior or equal to the length of the code used, thus in general, long coded sequences provide better SNR gains but introduce a higher computational load. It is likely that current technologies can handle this technical challenge, but in practice, an effective engineering solution will always try to limit the hardware complexity and the costs of a technical solution. For phase shift based velocity estimation techniques used in typical CFI implementations, decoding can be performed on the baseband signals, which is particularly attractive, since the sampling rate requirements are much lower after quadrature amplitude demodulation. Barker codes (and pseudo-random binary sequences, in general) are particularly effective for a practical hardware implementation since the codes can be generated with bi-level pulsers, whereas in theory, LFM chirps require multi-level pulsers. However, pseudo-chirps can also be used as demonstrated by O'Donnell [20]. A recent study has also demonstrated an effective solutions to synthesise non binary codes with good compression properties using a bipolar pulser [58].

The following illustrates the principle of baseband decoding. Consider the complex baseband signal $\underline{Z} = I + jQ$, the decoded baseband signal $\underline{Z}_d$ is obtained after a complex baseband matched filter:

$$\underline{Z}_d = \underline{Z} \otimes (\tilde{I}_c + j\tilde{Q}_c)^* = (I + jQ) \otimes (\tilde{I}_c + j\tilde{Q}_c)^* \tag{3.33}$$

where I_c and Q_c are the in-phase and quadrature components of the demodulated coded excitation signal, $\tilde{Q}_c$ and $\tilde{I}_c$ are time reversed version of I_c and Q_c, $\otimes$ denotes convolution and * conjugation. The decoded In-phase and Quadrature signals I_d and Q_d are thus the real part and imaginary part of $\underline{Z}_d$:

$$\begin{aligned} I_d &= (I \otimes \tilde{I}_c) - (Q \otimes \tilde{Q}_c) \\ Q_d &= (Q \otimes \tilde{I}_c) - (I \otimes \tilde{Q}_c) \end{aligned} \tag{3.34}$$

In the case of Barker codes, the excitation signal is obtained by modulating a baseband (real valued) sequence, as a consequence, $Q_c = 0$. The complex baseband matched filter simply consists of filtering the I and Q sequence with a time-reversed version of the modulating baseband Barker sequence I_c. Zhao [26] investigated different complex baseband decoding strategies (including sidelobes reduction with an inverse filter) and showed that the baseband decoding process was equivalent to a real convolution with the I/Q channels in parallel.

Complex baseband decoding with LFM chirps is also possible. Fig.3.7 shows the in-phase and quadrature components I_c and Q_c of a quadrature amplitude demodulated chirp (fractional bandwidth B_f = 0.5, time duration T_p = 10 μs, f_0 = 5MHz). Fig.3.8 shows the amplitude of the Fourier spectrum of the original LFM chirp, and that of the complex baseband chirp ($I_c + jQ_c$). As can be expected, the resulting spectrum has the same shape as the original spectrum, but centered on 0 and with twice the amplitude. The resulting compressed pulse was obtained as the result of the convolution of $(I_c + jQ_c) \otimes (\tilde{I}_c + j\tilde{Q}_c)^*$ and is shown in Fig.3.9. It has exactly the same shape as the compressed original chirp envelope but with twice the amplitude. Note that, to perform the complex baseband matched filtering in the case of LFM chirps, four convolutions have to be made in theory (Eq.3.34) instead of one, if performed on the RF data. This means that the computational load is not necessarily reduced by a great amount, depending on the downsampling factor, and the decoding requires a complex correlator. Baseband decoding with chirps was demonstrated as early as 1992 by O'Donnell [20][59] who implemented a whole coded excitation system with a linear array, using pseudo-chirps.

3.5.2 Sidelobes reduction

One of the practical aspects to consider when using coded waveforms is the magnitude of the sidelobes after compression. This is particularly critical for standard B-mode imaging in which case the range sidelobes have to be be reduced to a value inferior to the dynamic range (possibly 60 dB) of an image to ensure that their presence does not create any artifact. If the same pulse is

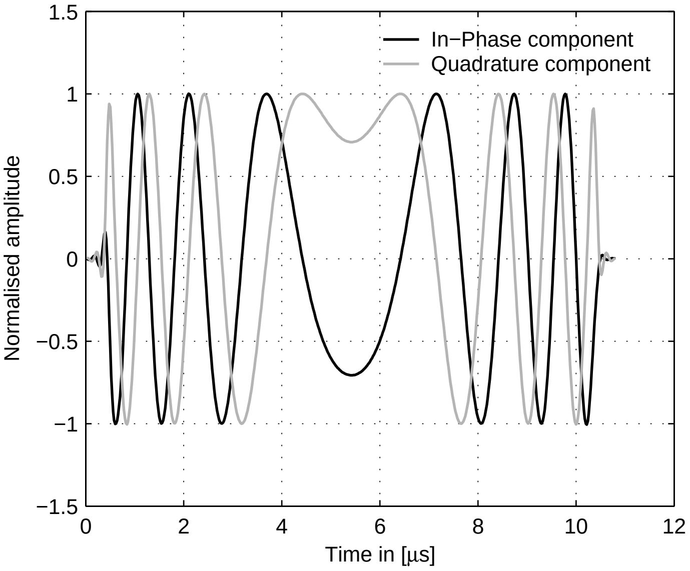

Figure 3.7: In-phase and quadrature components I_c and Q_c of the complex baseband chirp obtained after quadrature amplitude demodulation of a chirp waveform with parameters $T_p =$ 10 μs, $B_f =$ 0.5.

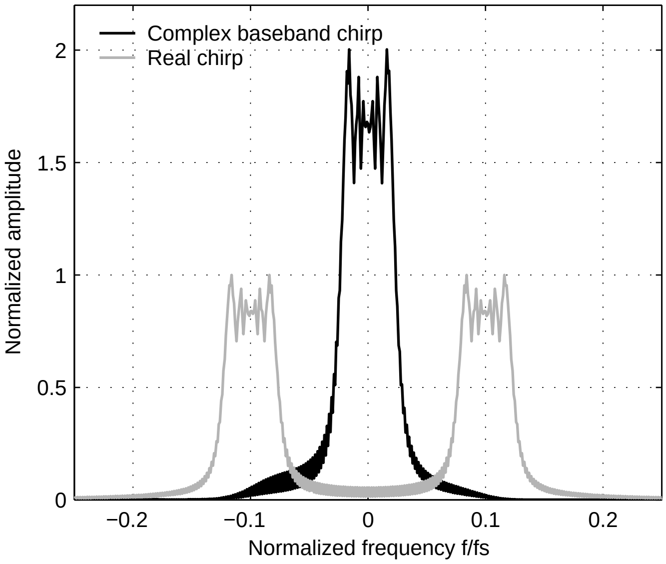

Figure 3.8: Comparison between the spectrum amplitude of the original chirp and the complex baseband chirp obtained after quadrature amplitude demodulation, for an original chirp with parameters $T_p =$ 10 μs, $B_f =$ 0.5.

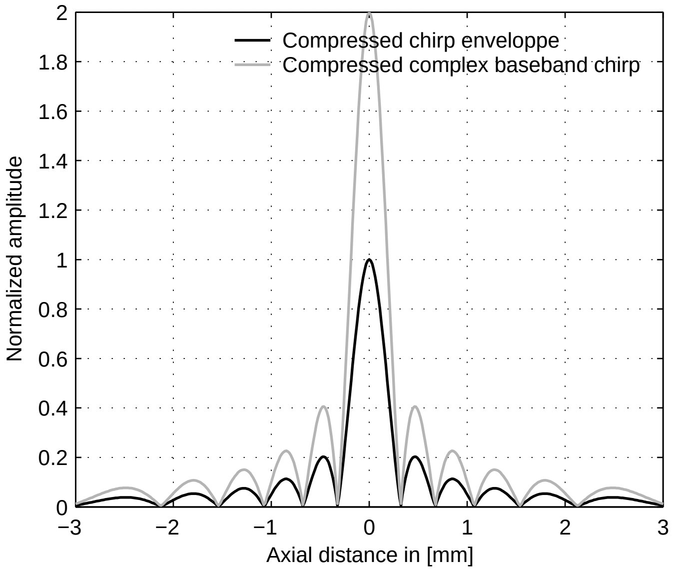

Figure 3.9: Comparison between the envelope of the compressed original chirp and the complex baseband chirp.

used both to form the B-mode grey-scale image of the region of interest and the velocity colour code that will be superimposed on top of it, a reduction of 40 dB seems to be a minimum value [26]. If the coded pulse is only used for velocity estimation purpose, the situation is however a bit different, since the noise levels are not far from the levels of signals backscattered from blood, the dynamic range of the useful signals for velocity estimation is thus limited. The artifact Doppler signals arising from the sidelobes after compression of signals from moving blood would probably be too low to be detected. Moreover, a threshold is usually applied, so that velocity information inferred from too weak signals is not displayed. The other concern is that sidelobes from slowly moving structures could create some additional clutter signals even in a remote region from the boundaries of a vessel. But in this case again, a clutter rejection filter is always applied anyway, which should remove these components. Acceptable levels for sidelobes thus appear to depend a lot on a specific implementation (level of signal threshold, clutter rejection filters, coded excitation used for velocity estimation only or both for the grey-scale image and the velocity colour code).

The impact of sidelobes on the sample volume itself and the spatial resolution of the velocity estimates are not clear either. It was shown in Chapter 1 that the sample volume was essentially perturbed axially. This means that velocities may potentially be averaged over a greater area and a significant velocity spread may be introduced in a range cell, which could potentially decrease the statistical performance of velocity estimators [11]. The overall resolution of the velocity estimates can however largely be dominated by signal processing. Efficient techniques to reduce sidelobes have been demonstrated in the field of medical ultrasound imaging for pseudo-random binary sequences [59][60][61]. These are usually based on inverse filtering (spectrum inversion techniques) described in the geophysics literature [62] or in the radar literature [63]. The drawbacks of these techniques is that, in the case of Barker codes, for instance, very long decoding sequence (much longer than the original oversampled Barker sequence) are then necessary [26]. In the case of LFM chirps, Misaridis has reviewed the techniques to reduce the sidelobe levels in [24] based on the radar literature [64], these involve usually and apodisation or an amplitude modulation of the excitation signal, combined with a mismatched filter at the receiver. An effective scheme based on apodisation of the LFM chirp and mismatched filtering was demonstrated by the same author [65]. Cowe [50] also demonstrated effective solutions for the case of Doppler applications involving a Wiener filter.

For the proposed waveforms in this study, a comparison between a system using Barker coded waveforms and LFM chirps is quite difficult. It was shown in Chapter 1 experimentally that Barker codes have relatively high sidelobes to start with (depending on the length of the baseband sequence used) and relatively independent of the bandwidth of the transmitted signal. In general the level of sidelobes is a trade-off with the axial resolution of the compressed pulse and the achieved gain in SNR [65]. Thus, depending on the sidelobes level required, the figures of gain in SNR and spatial resolution could significantly depart from the figures presented in Table 3.1.

3.5.3 Frequency dependent attenuation and non linear effects

Frequency dependent attenuation and non-linear effects are significant factors in the propagation of ultrasonic pulses in tissues. Misaridis [23] studied theoretically and with simulations the effect of a frequency mismatch between the received chirp and the emitted chirp due to frequency dependent attenuation. He showed that LFM chirp compression properties are quite robust to such effects although, a decrease in the gain in SNR is to be expected due to this mismatch. Moreover simulations showed that frequency dependent attenuation reduced the bandwidth of the chirp waveforms. Some studies have also proposed solutions to compensate for these effects [66]. Chiao [17] showed the relative robustness of pseudo-random binary sequences to frequency dependent attenuation and non linear propagation. These results seem to be in agreement with the observed relative robustness of coded waveforms compression properties after propagation in soft tissues in an experimental study [31].

One of the important aspects for velocity estimation is the shift in the centre frequency of the transmitted pulse due to frequency dependent attenuation. In the case of a Gaussian pulse, Misaridis [23] reports the following expression for the centre frequency f_{mean} of the pulse, as a function of depth z, fractional bandwidth B_f, an attenuation coefficient β:

$$f_{mean} = f_0 - (\beta B_f^2 f_0^2) z \tag{3.35}$$

This equations implies that if coded waveforms with a larger bandwidth than conventional CF pulses are used to improve resolution, the shift in the centre frequency of signal will be more important, this in turn can affect the statistical performance of a phase shift based estimator such as the 1D autocorrelator. The errors introduced by a shift in the centre frequency on the performance of pulsed Doppler techniques have been discussed in different studies [67][68], for instance. Therefore, the use of relatively wideband code waveforms may require the use of more advanced algorithms which take into account this shift in the centre frequency. Loupas proposed such an estimator in [11], this algorithm and the 1D autocorrelator will be introduced more in depth in the following chapter.

3.6 Conclusion

This chapter has discussed some basic considerations in using coded excitation techniques for CFI applications in medical ultrasound. The framework of this analysis was restricted to the study of the potential improvements in sensitivity and spatial resolution if conventional CF pulses are replaced by coded waveforms, in a typical CFI implementation using phase shift based velocity estimation techniques, and with a matched filter at the receiver. Specific differences have been emphasised with the case of B-mode imaging applications. One of the important aspects is that typical Doppler equipment operates close to the intensity limits for patient safety. In this case, the energy of the transmitted waveform is a limiting factor and thus the benefits of coded excitation are less dramatic. An SNR model for the specific case of incoherent scattering found in velocity estimation was reviewed and appropriate expressions were derived to discuss the potential resolution /sensitivity trade-off improvement with coded excitation. For typical CFI implementation using narrowband CF pulses, SNR improvements should be moderate compared to the possible improvements for B-mode imaging conditions (up to 15-20 dB [20]). Still, the achievable improvements in axial resolution are interesting in relation to visualising small vessels, for instance.

The sensitivity / resolution trade-offs were quantified and compared for two types of coded excitation: Barker codes and LFM chirps. If an increase in the energy of the transmitted pulse is permitted, then coded waveforms with a moderate length (up to 10 $\mu\mathrm{s}$) can be designed which offer a gain in both spatial resolution and sensitivity. The demand in average transmitted intensity can however be greatly increased (up to factors of 5/6, see Table 3.1 and 3.2), depending on the improvement on resolution, with still, quite moderate gains in SNR (less than 10 dB). Compared to Barker codes, LFM chirps have the unique feature that the time-bandwidth product can be set to any arbitrary value, which allows some flexibility in choosing independently the time duration and bandwidth of the waveform. In particular the sensitivity can be increased by transmitting longer chirps (up to a certain level for patient safety), without compromising the bandwidth (and the resolution). On the contrary, Barker codes have a time-bandwidth product fixed by the number of bits of the code, increasing the time duration by transmitting more cycles per chip translates into a reduction of the bandwidth and resolution.

Practical considerations have however to be taken into account as well. The first is the hardware complexity and cost. Again, in general, the use of long coded sequences will increase the complexity of matched filtering at the receiver, and thus put a constraint on the length of the code and the potential improvement in sensitivity, on top of intensity limitations for patient safety. For phase shift based velocity estimators, an effective solution should involve complex baseband decoding of the coded signals. Barker codes are an attractive solution for their simplicity, but solutions can similarly be designed for LFM chirps. Another consideration is range sidelobes reduction. It has been discussed that the sidelobes level requirements for velocity estimation may differ from imaging applications. In general, reducing the sidelobes level is a trade-off with the axial resolution and the SNR conditions, which may put a constraint on the expected benefits in the sensitivity / resolution trade-off. Finally, the effects of frequency-dependent attenuation were briefly mentioned. Coded waveform compression properties should be quite robust to such effects, however, the use of relatively wideband waveforms should increase the shift in the mean frequency the returned signals experience with depth, which might decrease the performance of phase shift based estimation.

Finally, a complete discussion on the potential benefits of coded excitation as a means to improve the performance of velocity estimation and especially, to provide better quantitative velocity estimates should involve a thorough investigation of the impact of the use of coded waveforms on the statistical performance (mean and bias) of velocity estimators. This will be the object of the following chapters.

Chapter 4

Phase shift based estimation with coded excitation

The goal of this chapter is to study the possible impact of using relatively wideband coded waveforms instead of conventional CF pulses with phase shift based estimators. The following questions are thus central to this chapter:

- What is the influence of the bandwidth of the transmitted signals on the statistical performance of these estimators after a matched filter at the receiver ?
- What is the influence of the SNR conditions on the statistical performance? i.e. in which situation will the gain in SNR provided by coded excitation be beneficial, and by how much is the statistical performance improved?
- How does coded excitation compare with a conventional situation when the packet size is increased? i.e. is it possible to use fewer pulses with coded excitation (increase of the frame rate) to yield a robust velocity estimate?
- Is coded excitation still beneficial when using relatively efficient, more complex 2D algorithms?

The first section introduces the principle of phase domain velocity estimation with a detailed theoretical analysis. The "1D autocorrelator", also called the "Kasai" algorithm is presented. The last part of this section also introduces a more complex 2D estimator, called the "modified autocorrelation algorithm". The second section investigates the theoretical aspects of performance with phase shift based estimators. Finally a simulation study is presented in the last section, which thoroughly investigates the potential impact of using coded excitation on the statistical performance of this type of estimator.

4.1 Principles of phase shift based velocity estimation

4.1.1 Theoretical principle

In this subsection, we review the general theoretical principle of velocity estimation based on the measurement of the phase shift experienced by the successive returned signals from moving scatterers. In the preceding chapter, it has been shown that the received signals due to blood backscattering could be considered as random bandpass signals, with, in first approximations, a centre frequency equal to that of the transmitted pulse, and the same bandwidth. For a theoretical analysis, it is useful to consider a complex signal model with a complex random amplitude envelope $\underline{Z}$ modulating a carrier at centre angular frequency f_0. Let us consider the n^{th} received signal after the n^{th} pulse transmit and for each successive received signal, we take the origin of time as the instant of firing. In the range gated window $[t_1, t_2]$, we then have:

$$r(t, nT_s) = \underline{Z}(t)e^{j2\pi f_0 t} = |\underline{Z}(t)|e^{j\phi(t)}e^{j2\pi f_0 t} \quad t \in [t_1, t_2] \tag{4.1}$$

where $r(t, nT_s)$ is the value of the received signal at instant t, following the n^{th} pulse transmit, T_s is the time between two pulse transmits (PRP), and $\phi(t)$ the argument of $\underline{Z}$. This model of complex signal was justified by Rice for random bandpass processes [69, p365] and may be obtained from a real signal, in practise, with the use of the Hilbert transform. If now, after another pulse transmit, the $(n+1)^{th}$ received signals is a time shifted version (time shift Δt) of this signal due to the movement of the scatterers in the sample volume:

$$\begin{aligned} r(t,(n+1)T_s) &= r(t-\Delta t, nT_s) \\ &= \underline{Z}(t-\Delta t)e^{j2\pi f_0 (t-\Delta t)} = |\underline{Z}(t-\Delta t)|e^{j\phi(t-\Delta t)}e^{j2\pi f_0 (t-\Delta t)} \quad t \in [t_1, t_2]. \end{aligned} \tag{4.2}$$

For simplicity of notations, we can now consider a specific instant t in the range gate, after quadrature amplitude demodulation has taken place. The complex envelope values $\underline{Z}_n$ and $\underline{Z}_{n+1}$ obtained after demodulation for this specific time t for the n^{th} and $(n+1)^{th}$ signals are given by:

$$\begin{aligned} \underline{Z}_n &= \underline{Z}(t) = |\underline{Z}_n|e^{j\phi_n} \\ \underline{Z}_{n+1} &= \underline{Z}(t-\Delta t)e^{-j2\pi f_0 \Delta t} = |\underline{Z}_{n+1}|e^{j\phi_{n+1}} \end{aligned} \tag{4.3}$$

With according to the previous equations Eq.4.1 and Eq.4.2:

$$\begin{aligned} \phi_n &= \phi(t) \\ \phi_{n+1} &= \phi(t-\Delta t) - 2\pi f_0 \Delta t \end{aligned} \tag{4.4}$$

The phase shift that appears in the complex amplitude is thus, from Eq.4.4:

$$\Delta\phi = \phi_n - \phi_{n+1} = \phi(t) - \phi(t-\Delta t) + 2\pi f_0 \Delta t \tag{4.5}$$

If we neglect the term $\phi(t) - \phi(t-\Delta t)$ the phase difference is simply equal to:

$$\Delta\phi \approx 2\pi f_0 \Delta t \tag{4.6}$$

The implications of this assumption will be studied in the next section. We can now relate this phase shift to a velocity by substituting the expression of Δt, which depends on the velocity of the scatterers in the interval T_s (v is the axial velocity of scatterers):

$$\Delta t = \frac{2v}{c} T_s. \tag{4.7}$$

We thus find the following velocity estimator, based on a estimation of the phase shift $\Delta\phi$:

$$v = \frac{c\Delta\phi}{4\pi f_0 T_s}. \tag{4.8}$$

In fact, one can also interpret the two values $\underline{Z}_n$ and $\underline{Z}_{n+1}$ as two samples of the complex slow time signals sampled at the frequency (PRF) $1/T_s$. An instantaneous frequency f_i can be computed from the derivative of the phase of the signals:

$$f_i = \frac{1}{2\pi}\frac{d\phi(t)}{dt} \approx \frac{1}{2\pi}\frac{\Delta\phi}{T_s}. \tag{4.9}$$

Using the expressions of the phase in shift Eq.4.6 and of Δt in Eq.4.7 yields:

$$f_i = \frac{\Delta t}{T_s} f_0 = \frac{2v}{c} f_0, \tag{4.10}$$

and thus, the frequency naturally identifies with the Doppler shift. An estimator of the Doppler shift is then simply given by:

$$f_D = \frac{\Delta\phi}{2\pi}\frac{1}{T_s}. \tag{4.11}$$

Of course, applying the Doppler equation to this last estimator yields the same velocity estimator previously obtained in Eq.4.8. In practise, the In-Phase I and Quadrature component Q of the signal after coherent quadrature amplitude demodulation give access to the cosine and sine values of the phases ϕ_i and ϕ_{i+1}. The phase shift can thus be determined by its tangent; using some simple trigonometry:

$$\Delta\phi = \phi_n - \phi_{n+1} = \arctan\frac{\sin(\phi_n - \phi_{n+1})}{\cos(\phi_n - \phi_{n+1})} = \arctan\frac{\sin\phi_n\cos\phi_{n+1} - \cos\phi_n\sin\phi_{n+1}}{\cos\phi_n\cos\phi_{n+1} + \sin\phi_n\sin\phi_{n+1}}. \tag{4.12}$$

Noting that $\underline{Z}_n\underline{Z}^*_{n+1} = |\underline{Z}_n\underline{Z}^*_{n+1}|e^{j(\phi_n - \phi_{n+1})}$ the estimator can equivalently be written:

$$f_D = \frac{\mathrm{Arg}[\underline{Z}_n\underline{Z}^*_{n+1}]}{2\pi T_s} = \frac{1}{2\pi T_s}\arctan\frac{\mathrm{Im}[\underline{Z}_n\underline{Z}^*_{n+1}]}{\mathrm{Re}[\underline{Z}_n\underline{Z}^*_{n+1}]} \tag{4.13}$$

where Arg denotes the argument of a complex number and $\mathrm{Im}[]$ and $\mathrm{Re}[]$ denote the imaginary and real parts of a complex number. Substituting $\underline{Z}_n = Q(n) + jI(n)$ and $\underline{Z}_{n+1} = Q(n+1) + jI(n+1)$ yields the simple estimator of the mean Doppler frequency, using a single pair of signals:

$$f_D = \frac{1}{2\pi T_s}\arctan\left[\frac{Q(n)I(n+1) - Q(n+1)I(n)}{Q(n+1)Q(n) + I(n+1)I(n)}\right] \tag{4.14}$$

4.1.2 The narrowband approximation

All the preceding analysis was based on the assumption that:

$$\phi(t - \Delta t) \approx \phi(t) \tag{4.15}$$

It is interesting to understand what this approximation means in terms of signal properties, and under what conditions this approximation holds. A way to understand Eq.4.15 is simply to state that the random complex amplitude should not vary too much over the considered time interval Δt. This should obviously depend on the amplitude of Δt to be measured (and thus the corresponding velocity to be estimated for a given PRF). Note that in general, to avoid aliasing conditions, Δt is less than half a period at the considered centre frequency. To understand the impact of this approximation on the estimator, let us consider a hypothetical case when $\underline{Z}$(t) is a sinusoid of constant amplitude A and angular frequency f_{mod}:

$$r(t) = \underline{Z}(t)e^{j2\pi f_0 t} = Ae^{j2\pi f_{mod}t}e^{j2\pi f_0 t} \tag{4.16}$$

After a shift Δt the signal becomes:

$$r(t-\Delta t) = Ae^{j2\pi f_{mod}(t-\Delta t)}e^{j2\pi f_0(t-\Delta t)} = Ae^{j(2\pi f_{mod}t-(f_{mod}+f_0)\Delta t)}e^{j2\pi f_0 t} \tag{4.17}$$

We see that the phase shift appearing in the complex envelope is then:

$$\Delta\phi = 2\pi(f_0 + f_{mod})\Delta t. \tag{4.18}$$

And thus, the modulation introduces an error in the estimation. The error is negligible provided $f_0 \gg f_{mod}$, that is, provided the envelope does not fluctuate too much over a period of the signal. This is a narrowband approximation on the signal because intuitively as the signal's bandwidth is increased, some higher frequency components in the complex envelope are introduced, and the hypothesis $f_0 \gg f_{mod}$ can not be satisfied anymore.

From this simple analysis, this approximation is likely to be satisfied, and thus, the overall accuracy of the method should improve if:

- Δt is small, i.e. if small velocities are measured or a relatively high PRF is chosen ($\Delta t = v/\mathrm{PRF}$). In practice, however, this cannot be easily controlled.
- the more the transmitted signal is narrowband (although the Doppler bandwidth may depend to some extent on factors that are independent of the bandwidth of the transmitted signal (as already mentioned in the introduction chapter, section 1.1.3.2), this is referred to as “spectral broadening" [12, p134-140]).

4.1.3 Combining several pairs of signals

The estimator derived so far in Eq.4.12 only uses a single pair of signal. To increase the reliability of estimation (of either the Doppler shift or the corresponding velocity), it is often desirable to combine several pairs of signals, especially in typically noisy conditions found in CFI applications). This is possible in practise because although the velocities vary considerably over a cardiac cycle in a blood vessel (or artery), the hypothesis of stationarity over a period of time of 5 to 10 ms can be considered as a good approximation [28, p629]. This gives time to transmit/receive a maximum of $N_p = 25$ bursts at a typical PRF of 5kHz (this is only a theoretical value, though, because in CFI applications, some time is also allocated to refresh the B-mode grey scale image).

It is interesting to note that several schemes can be proposed from Eq.4.12. The simplest approach consists in averaging the phase shifts computed from $N_p - 1$ consecutive pairs:

$$\Delta\phi = \frac{1}{N_p - 1} \sum_{n=1}^{N_p-1} \arctan \frac{\sin(\phi_n - \phi_{n+1})}{\cos(\phi_n - \phi_{n+1})}. \tag{4.19}$$

That is, the estimated frequency over several pulse transmits becomes :

$$f_D = \frac{1}{2\pi T_s} \frac{1}{N_p - 1} \sum_{n=1}^{N_p-1} \Delta\phi_n, \tag{4.20}$$

where $\Delta\phi_n = \phi_n - \phi_{n+1}$.Another estimator can be obtained by averaging the numerator and the denominator in Eq.4.12:

$$f_D = \frac{1}{2\pi T_s} \arctan \frac{\sum_{n=1}^{N_p-1} \sin(\phi_n - \phi_{n+1})}{\sum_{n=1}^{N_p-1} \cos(\phi_n - \phi_{n+1})} \tag{4.21}$$

These two estimators were in fact considered by Sirmans [70] and are referred to as the Scalar Phase Change (SPC) and Vector Phase Change (VPC) estimators. In practice, the classical estimator used in medical ultrasound slightly differs from these two, and can be written as:

$$f_D = \frac{1}{2\pi T_s} \arctan \frac{\sum_{n=1}^{N_p-1} \mathrm{Im}[\underline{Z}_n \underline{Z}_{n+1}^*]}{\sum_{n=1}^{N_p-1} \mathrm{Re}[\underline{Z}_n \underline{Z}_{n+1}^*]}. \tag{4.22}$$

Rewriting the preceding equation as:

$$f_D = \frac{1}{2\pi T_s} \arctan \frac{\sum_{n=1}^{N_p-1} |\underline{Z}_n \underline{Z}_{n+1}^*| \sin(\phi_n - \phi_{n+1})}{\sum_{n=1}^{N_p-1} |\underline{Z}_n \underline{Z}_{n+1}^*| \cos(\phi_n - \phi_{n+1})}, \tag{4.23}$$

we can see that this estimator performs an average of the cosine terms at the denominator and the sine terms at the numerator, but contrary to the VPC estimator, it retains some information from the envelope amplitude variations of the signals through the weighting term $|\underline{Z}_{n+1} \underline{Z}_n^*|$ in the sums. Following the definition of $\underline{Z}$, this estimator can also be easily put into form using the Q and I component of the demodulated signal :

$$f_D = \frac{1}{2\pi T_s} \arctan \frac{\sum_{n=1}^{N_p-1} Q(n)I(n+1) - Q(n)I(n+1)}{\sum_{n=1}^{N_p-1} I(n)I(n-1) + Q(n)Q(n+1)} \tag{4.24}$$

This estimator is often referred to as the “Kasai” algorithm in the field of medical ultrasound, referring to the name of one of the researcher from a Japanese team who demonstrated for the first time in the eighties the feasibility of a real-time CFI system using this estimator [39]. Some authors had however considered the use of similar phase shift based estimation schemes beforehand [71][72] as noticed in [12]. The estimator is also referred to as the “1D autocorrelator” algorithm, which can be understood by noting from Eq.4.22, that if R denotes the complex autocorrelation function of the baseband signals, then:

$$R(T_s) = \frac{1}{N} \sum_{n=1}^{N_p-1} \underline{Z}_n \underline{Z}_{n+1}^*, \tag{4.25}$$

is the autocorrelation of the Doppler baseband signals at lag one. Obviously $\mathrm{Re}[\sum \underline{Z}_{n+1}\underline{Z}_n^*] = \sum \mathrm{Re}[\underline{Z}_{n+1}\underline{Z}_n^*]$ and the same holds for the imaginary part, the estimated frequency can thus easily be computed from the real and imaginary part of the complex autocorrelation at lag one. This estimator had been studied from the 70’s in the radar literature and is often referred to as the “mean frequency estimator” or the “Pulse Pair Processing” estimator (PPP) [73][74]. Sirmans [70] studied the three estimators numerically and found that the PPP offered the best properties in noisy conditions. It is finally interesting to note that in each of the estimators presented, it is not clear how the estimated frequency over several $N_p - 1$ pulse pairs relates to the mean Doppler frequency present in the N_p samples of the slow time Doppler signal. In the case of the 1D autocorrelator, however, it can be shown that the estimated frequency is an estimator of the mean frequency of the Doppler power spectrum of the signal, the derivation can be found in [39].

4.1.4 More advanced algorithms: example of the 2D modified autocorrelation

Since the advent of the 1D autocorrelator estimator, and its successful implementation for a real-time Colour Flow Imaging system, several authors have proposed refined phase shift based algorithms. The motivations for new algorithms is an increased statistical performance. As hardware became cheaper and faster, the relative difficulty of implementation of more complex algorithms became less of an issue. The basis for an increased performance is to extract the maximum information from the available data. From this point of view, the Kasai estimator works essentially in 1D because the algorithms only retain one value per gated range window. Recall that all the theoretical analysis was performed using a single instant t in a range gated window (usually in practise, the signal is collapsed into a single point per gated range window by integration in the range gate [11]). A more powerful approach for estimation consists of extracting the full information provided by the 2D dataset of sampled complex baseband signals $\underline{Z}(n,m)$, where m refers to samples along the fast time axis. Vaitkus [75] showed, with a theoretical analysis based on the Cramer Rao Lower Bound (CRLB), that 2D based estimation should lead to an increased statistical performance. In the next paragraph, we will focus on the 2D estimation approach developed by Loupas in [11], which is called “the modified autocorrelation”.

Loupas’2D estimator is derived similarly to the 1D autocorrelation estimator, but the mean Doppler frequency is this time estimated using the 2D complex autocorrelation $R(n',m')$:

$$R(m',n') = \sum_{m=1}^{M-m'} \sum_{n=1}^{N_p-n'} \underline{Z}(m,n)\underline{Z}^*(m+m',n+n'), \tag{4.26}$$

where M is the total number of samples in a gated range window, and m indexes samples along the fast time axis, with sampling period t_s. The estimated Doppler frequency is then computed from the lag one ($n' = 1$):

$$f_D = \frac{1}{2\pi T_s}\arctan\left(\frac{\mathrm{Im}[R(0,1)]}{\mathrm{Re}[R(0,1)]}\right) = \frac{1}{2\pi T_s}\frac{\sum_{m=1}^{M}\sum_{n=1}^{N_p-1}\mathrm{Im}[\underline{Z}(m,n)\underline{Z}^*(m,n+1)]}{\sum_{m=1}^{M}\sum_{n=1}^{N_p-1}\mathrm{Re}[\underline{Z}(m,n)\underline{Z}^*(m,n+1)]}. \tag{4.27}$$

We see that this estimator makes full use of the 2D set of data $\underline{Z}(m,n)$ from a range gate to infer the mean Doppler shift f_D. It can be understood as performing the 1D autocorrelator on the slow time signals at time $t = mt_s$, $m \in [1, M]$ and then averaging all the estimates. The corresponding velocity estimator v_{2D_DOP} is then obtained by applying the Doppler equation:

$$v_{2D\_DOP} = \frac{c}{2}\frac{f_D}{f_0} \tag{4.28}$$

Loupas pointed out that in the implementation of Eq.4.28, the centre frequency at the denominator is considered to be constant, which will lead to some error in the velocity estimate if the mean frequency of the returned signal has changed. This was also highlighted in the introduction chapter. Thus, the centre frequency of the fast time axis f_{RF} should also be estimated in the range gate in order to make a full evaluation of the Doppler equation. A similar analysis to the preceding case shows that the mean frequency in the fast time axis signal can be estimated from:

$$f_{RF} = f_{dem} + \frac{1}{2\pi t_s} \arctan\left(\frac{\mathrm{Im}[R(1,0)]}{\mathrm{Re}[R(1,0)]}\right) = f_{dem} + \frac{1}{2\pi t_s} \frac{\displaystyle\sum_{m=1}^{M-1}\sum_{n=1}^{N_p} \mathrm{Im}[\underline{Z}(m,n)\underline{Z}^*(m+1,n)]}{\displaystyle\sum_{m=1}^{M-1}\sum_{n=1}^{N_p} \mathrm{Re}[\underline{Z}(m,n)\underline{Z}^*(m+1,n)]}, \tag{4.29}$$

where f_{dem} is the demodulating frequency. The final velocity estimator is then computed from:

$$v_{2D} = \frac{c}{2}\frac{f_D}{f_{RF}} \tag{4.30}$$

This estimator was studied by Loupas using some extensive simulations, which demonstrated an enhanced statistical performance compared to the 1D autocorrelator [11]. In the simulations presented, the gain in performance of the centre RF frequency estimation part in v_{2D} (Eq.4.30) appeared to be important compared to v_{2D_DOP} (Eq.4.28) when a significant velocity dispersion was simulated (scatterers with different velocities in the sample volume). Finally, it is interesting to note that a few years later, Brands [76] derived an estimator called C3M (which stands for 'Complex Cross Correlation model) which is mathematically identical to Loupas' estimator except that it works directly on the RF signals instead of the demodulated signals. The benefits of such an approach are however not clear, since processing the baseband signals reduces in general the complexity of implementation due to lower sampling requirements.

4.2 Theoretical study of the statistical performance

4.2.1 Motivations for a theoretical approach and litterature review

Since the goal of this chapter is to quantify the potential benefits of using coded excitation on the statistical performance of phase shift based estimators, it is interesting to obtain a theoretical expression for the variance of the velocity estimates, even if this expression only gives a partial picture of the performance of the estimator working in ”real" conditions. Of particular interest in the context of this study is to obtain an expression showing the influence on the statistical performance of:

- the bandwidth of the transmitted signals.
- the SNR conditions.
- the packet size (total number of transmit / receive cycles used to infer one velocity estimate).

Only a few papers have studied the statististical performance of the 1D autocorrelator in the field of medical ultrasound. Such analysis in general requires some approximations, due to the relative complexity of the analytical expressions involved. Kristoffersen [77] developed a general theoretical framework to describe the statistical properties of mean frequency estimators. Torp et al. [78] described the probability density function of the autocorrelation estimates. Later on, a theoretical expression was presented by Loupas in the same paper introducing the modified autocorrelation [11]. His analysis is based on an expression obtained in the early seventies by Miller et al. [79], who derived the variance of the frequency estimates when a large number of independent pairs are used. The application of these results to medical ultrasound is however not without flaws since the 1D autocorrelator works on consecutive pairs of signals $\{\underline{Z}_i, \underline{Z}_{i+1}\}$, which are obviously not independent. Miller et al. were also able to show that in this particular case, the estimator reaches the Cramer Rao lower bound and is asymptotically unbiased for symmetric power spectra. Sirmans [70] studied the bias of the estimator and showed that the estimator remained very robust even in the case of asymmetric spectra.

The more rigorous case for medical ultrasound applications when the estimator is used on correlated consecutive pairs appears to have been studied by [80] using a perturbation analysis. Zrnic [73][74] studied in depth the statistical properties of the estimator for weather radar applications, and showed in particular that the probability density function of the error could be found directly, but the relative complexity of the expressions prevented from obtaining any simple insights into the statistical performance. He proposed an unifying expression for both cases (independent and correlated pairs) and showed that incidentally, the two cases did not differ much in terms of performance. In the next section, we propose to use and adapt the expression of Miller[79] as Loupas in [11], but we will further arrange it to obtain an interesting expression in the context of this study.

4.2.2 Derivation of an expression of the variance of the velocity estimates

The model of complex correlation assumed by Miller is based on the assumptions of a Gaussian signal of power S embedded in a random white noise of power N, which yields:

$$R(\tau) = S.e^{-(2\pi B_D \tau)^2/2} e^{-j2\pi f_D \tau} + N.\delta(\tau), \tag{4.31}$$

where B_D is the Doppler bandwidth (in Hz) of the modelled signal and f_D is the true mean Doppler frequency. Loupas rearranged Miller's expression into (adapting the notations), to obtain the mean frequency estimator variance σ^2 :

$$\sigma^2 = \frac{(1 + 1/\mathrm{SNR})^2 - e^{-2\pi^2 B_D^2 T_s^2}}{8\pi^2 N_p T_s^2 e^{-2\pi^2 B_D^2 T_s^2}}, \tag{4.32}$$

where SNR is defined as S/N, N_p is the number of pulse transmit/receive cycles (which yields $N_p - 1$ consecutive pairs of signals). To get some insights into the role of the transmitted bandwidth B, we propose to use a simple model of the Doppler bandwidth B_D. In the ideal case when no spectral broadening occurs, and the velocity spread of the targets is limited, the relationship between the two bandwidth is simply:

$$B_D = \frac{2v}{c} B \tag{4.33}$$

To reduce the number of variables in this expression, the terms in $B_D T_s$ can further be arranged. We use $\delta = vT_s$, the axial displacement of the scatterers during the sampling time T_s (or PRP), λ the wavelength at the centre frequency, and B_f, the fractional bandwidth:

$$B_D T_s = 2(\delta/\lambda) B_f, \tag{4.34}$$

The statistical performance of estimators is usually studied using the relative error, that is, the ratio of the standard deviation of the frequency estimates to the actual true mean frequency (this is more rigorously the definition of the ‘coefficient of variation’, we will however use the term ‘relative error’, for consistency with the literature). We obtain the following equation for the performance:

$$\frac{\sigma}{f_D} = \left[\frac{(1 + 1/\mathrm{SNR})^2 - e^{-8\pi^2 (\delta/\lambda)^2 B_f^2}}{32\pi^2 N_p (\delta/\lambda)^2 e^{-8\pi^2 (\delta/\lambda)^2 B_f^2}} \right]^{\frac{1}{2}} \tag{4.35}$$

Note that the term $f_D T_s$ was similarly simplified into $(2\delta/\lambda)$ at the denominator since in our simple model, we have $f_D = \frac{2v}{c} f_0$. This yields an interesting expression, where the performance only depends on the SNR conditions, the displacement of the scatterers between the pulse repetition period T_s as a fraction of the wavelength, and the fractional bandwidth of the transmitted pulse. This expression can equivalently evaluate the performance in terms of velocity estimates since the two quantities are proportional ($v = \frac{c}{2f_0} f_D$). As can be seen, the final expression obtained does not yield any simple behaviour in terms of the influence of the SNR (function as $(1 + 1/SNR)^2$), nor for the influence of the bandwidth of the transmitted signals (through the exponential terms). It can be noticed however, that the relative error is decreased as $1/\sqrt{N_p}$, which is the same as what would be expected when averaging N_p independent estimates.

4.2.3 Plots of the expression

The expression 4.35 was plotted for different set of parameters, and a number of pulse transmit/receive cycles set to $N_p = 10$. The relative errors obtained show that the estimator performs very well for 10 pulse transmit/receive cycles in the idealised situation when no spectral broadening occurs, and the velocity spread in the range cell is negligible. Even in the worst SNR conditions (5 dB) the relative error is still of the order of 10 % for narrowband waveforms. Fig.4.1 shows the influence of the fractional bandwidth of the transmitted pulse on the performance, for four different axial shifts of scatterers (0.05 λ, 0.15 λ, 0.20 λ). Note that the symmetric interval of non aliased velocities correspond to shifts in [-0.25 λ, +0.25 λ]. We can clearly see that the performance of the estimator degrades for large fractional bandwidths. For SNR larger than 20 dB, increased axial displacements lead to a decreased performance for large fractional bandwidth, whereas the relative error is completely independent of the axial displacements for fractional bandwidths less than 0.3. The situation for lower SNR is slightly different; the expression suggests that smaller shifts are more affected for low fractional bandwidths, in particular, on can notice that the performance is significantly deteriorated for a small shift (0.05λ) for an SNR of 5 dB and a low fractional bandwidth. Fig.4.2 presents the information differently and shows the evolution of performance for a fixed shift of 0.15 λ, and two different fractional bandwidths, against SNR. This figure confirms that the performance is not significantly affected by the SNR conditions for SNR values greater than 10 dB. The fractional bandwidth has clearly a significant impact on the ultimate performance reached by the estimator (around 2.5% for $B_f = 0$ .15 and only 8.3 % for $B_f = 0.5$). Finally Fig.4.3 shows the relatively

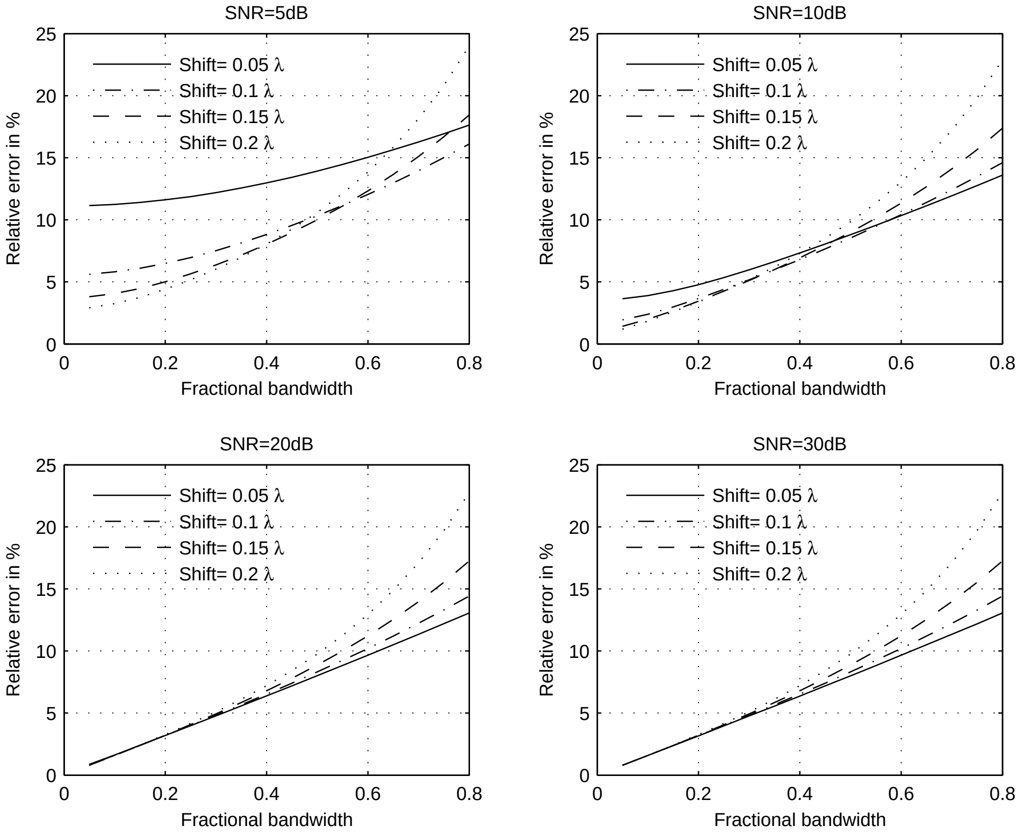

Figure 4.1: Plot of the theoretical performance of the 1D autocorrelator against the fractional bandwidth used, for different axial displacements of scatterers as a fraction of the wavelength and different SNR conditions, $N_p = 10$.

complex dependence of the performance against the non-aliased range of axial displacements in relatively low SNR conditions (5 and 10 dB). Again, different behaviours are observed for pulses with different fractional bandwidths. It can be observed that the performance is deteriorated for $B_f = 0.5$ and that the curve demonstrate a minimum in this case.

4.2.4 Discussion

The preceding plots show that the estimator is quite robust when using a medium packet size ($N_p = 10$). An improvement in the SNR conditions by coded excitation appears to be beneficial in terms of performance only for a low range of SNR (less than 10 dB). From an application point of view, this is not completely irrelevant since for blood flow estimation the SNR is usually low. Tissue Doppler Imaging techniques, however, benefit from SNR conditions due to the difference in backscattering power from blood and tissues (signals level from tissues are

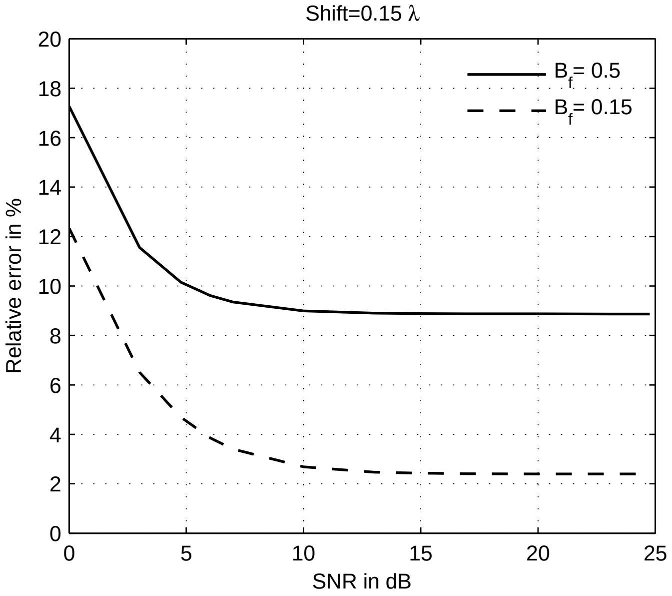

Figure 4.2: Plot of the performance of the 1D autocorrelator against the SNR for an axial displacement of 0.15 λ and two different fractional bandwidths, $B_f = 0.15$ and $B_f = 0.5$, $N_p = 10$.

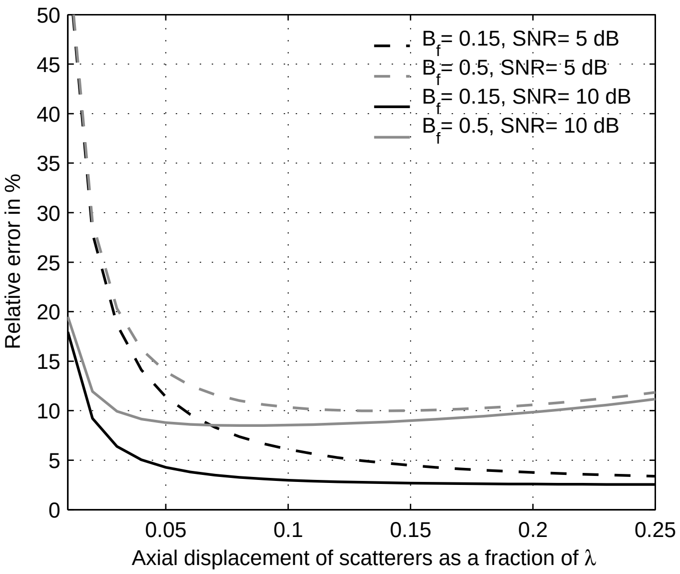

Figure 4.3: Plot of the performance of the 1D autocorrelator against the axial displacement for two different fractional bandwidths, $B_f = 0.15$ and $B_f = 0.5$, and two different SNR conditions 5 and 10 dB, $N_p = 10$.

typically 20 to 40 dB higher then the observed levels for blood [13, p207]). From a resolution point of view, the preceding plots clearly show that due to the narrowband approximation involved for the estimation technique, the performance is deteriorated if a wideband pulse is used, at least for moderate SNR conditions (20-30 dB). These aspects will be further studied using simulations in the next section. In particular, since Miller's expression was obtained as an asymptotic solution (for large N_p values) it is not convenient to evaluate the performance for smaller packet size, therefore the use of coded excitation might be beneficial in this case to achieve a robust estimation with an increased frame rate. It also interesting to study the relative error of the estimator when a matched filter is used at the receiver, which is not taken into account by Eq.4.31.

4.3 Simulations

4.3.1 Implementation of the 1D autocorrelator with coded excitation

The estimator works essentially in 1D since it is applied to the slow time signals. For a particular depth of return corresponding to $t = t_1$, and considering N successive pulse transmits, f_D is estimated as:

$$f_D = \frac{1}{2\pi T_s} \frac{\sum_{n=1}^{N-1} \mathrm{Im}[\underline{Z}(t_1, nT_s)\underline{Z}(t_1, (n+1)T_s)^*]}{\sum_{n=1}^{N-1} \mathrm{Re}[\underline{Z}(t_1, nT_s)\underline{Z}(t_1, (n+1)T_s)^*]}, \tag{4.36}$$

where $\mathrm{Im}[]$ and $\mathrm{Re}[]$ denote the imaginary and real parts of a complex number.

In a conventional CFI implementation, signals are usually range gated and filtered in the same operation after quadrature amplitude demodulation has taken place. The signals are integrated over the duration of a range gate T_r (equivalent to the averaging filter described in section 3.2.1), and the estimator is then applied on signals of the form $\underline{Z}_{int}(mT_r, nT_s)$:

$$\underline{Z}_{int}(mT_r, nT_s) = \int_{mT_r}^{(m+1)T_r} \underline{Z}(t, nT_s)dt. \tag{4.37}$$

where m indexes the successive range gates with depth. For optimal performance, T_r is usually chosen to be equal to the duration of the transmitted pulse ($T_p = T_r$)[57].

In the case of an implementation with coded excitation the step of integration in the range gate is *a priori* not necessary since a matched filter would be applied to the data. It is also interesting to note that T_r can then be chosen independently of T_p, since due to the 1D nature of the estimator "range gating" becomes essentially downsampling along the fast time axis after matched filtering and quadrature amplitude demodulation have been performed. Finally, although matched filtering is only considered on the RF data in this study, applying the filter on the baseband data is also possible (i.e. after quadrature amplitude demodulation). This is particularly interesting from an implementation point of view because the sample rate requirements are lower with the baseband data. Zhao [26] detailed the principles of a CFI system working with Barker codes with long decoding sequences applied to the demodulated signals. Baseband matched filtering is also possible for LFM chirps, although the operation requires a complex correlator in this case. This approach was demonstrated by O'Donnell [20] with pseudo-chirps, in the context of B-mode imaging. The principle of baseband decoding was also introduced in the previous chapter.

4.3.2 Simulation set-up

For all the simulations, the simple 1D model of backscattered signals presented in section 3.3.4 (Chapter 3) was adopted. The principle is repeated here for convenience: synthetic radio-frequency (RF) speckle signals signal are obtained by successively convolving an excitation signal e (either a CF pulse or a chirp) with a transducer's impulse response h_{trans} and a Gaussian white noise realisation n_1:

$$s = (e \otimes h_{trans}) \otimes n_1 \tag{4.38}$$

where $\otimes$ denotes time convolution. For all simulations, the centre frequency used was 5 MHz, the transducer's impulse response was modelled as a Gaussian modulated pulse of -6 dB fractional bandwidth $B_f = 0.5$, and the sampling frequency was set to 50 MHz. LFM chirp waveforms were chosen for this study as an example of coded excitation. We adopt the hypothesis that an increase in the transmitted intensity is permitted and that the peak intensity of the signals is the limiting factor to improve the SNR. All excitation signal amplitudes were thus normalised (criterion of the same peak intensity). To mimic the successive returned signals of moving blood, the obtained RF synthetic signals were shifted in time, and independent white noise (allpass) realisations of given powers were added to model different SNR reception conditions. Thus, the modelled kth returned signal $r(k, t)$ can be simply expressed as:

$$r(t, k) = s(t - k\Delta t) + n_{2k} \qquad k \in [1, N_p] \tag{4.39}$$

where $s(t)$ is the generated RF synthetic speckle signal, n_{2k} are independent white (allpass) Gaussian noise realisations, and N_p is the number of transmit/receive cycles (packet size) used to perform velocity estimation. Note that this simulation scheme ignores all the possible effects of decorrelation from one received signal to another (velocity spread in the sample volume, modulation by the transducer's transverse field pattern due to the transverse component of the velocity of scatterers, etc.), and is thus an ideal statistical performance case study. The time shift Δt was set to yield an equivalent axial displacement shift of the scatterers, measured as a fraction of the wavelength at the centre frequency. The values were selected to span the positive values of the symmetric non-aliased range of estimated axial shifts [-0.25 λ, +0.25 λ]. In order to mimic shifts in time smaller than one sample at 50 MHz, the signals were interpolated eight times and downsampled to the original sample frequency after time translation.

Gated range portions of the simulated returned RF signals were extracted, matched filtered, demodulated, and processed by the velocity estimation algorithm. T_r was set to be approximately the length of the wideband compressed chirp tested (T_p = 10 μs, B_f = 0.5), which yields $1/B_f f_0$ = 0.4 μs. Both the 1D autocorrelator and the modified autocorrelation were implemented based on Eq.4.22, Eq.4.27 and Eq.4.28 . In the case of the modified autocorrelation algorithm only the simplified version was implemented (called the “2D_ DOP” estimator in Loupas' original paper [11] corresponding to Eq.4.28 and which will be referred to as the “simplified modified autocorrelation” estimator in the rest of this chapter). Since our simulation does not model any frequency dependent attenuation or velocity spread in a range cell, it was found that the RF centre frequency estimation part of the modified autocorrelation algorithm introduced a loss in performance at high SNR. The performance of estimation was measured as the relative error, i.e. the ratio of the standard deviation of the estimated displacements to the actual true displacement. In order to obtain statistically reliable results, individual standard deviations of the displacement estimates were computed from 15000 independent range gated windows for each combination of the simulation parameters.

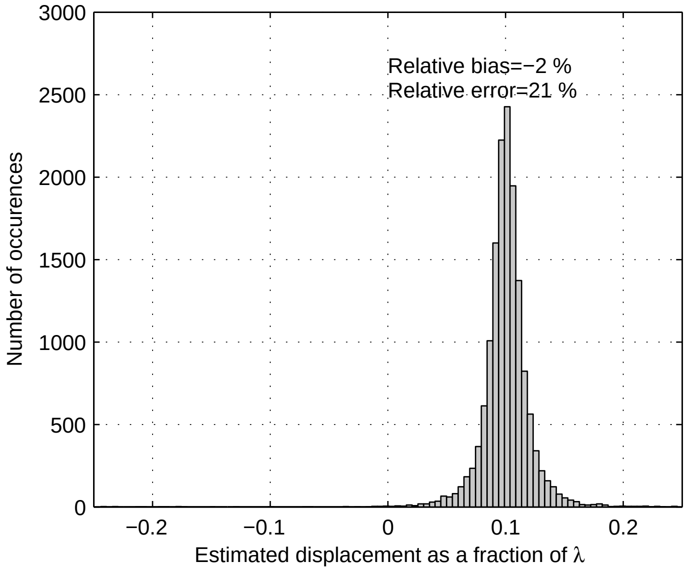

Figure 4.4: Histogram of the velocity estimates obtained for a simulated axial displacement of 0.10 λ, and SNR= 5 dB for the chirp signal $B_f = 0.5$.

4.3.3 Statistical performance analysis

A first set of simulation studies the performance of the 1D autocorrelator algorithm with a chirp of length $T_p = 10$ μs, and fractional bandwidth $B_f = 0.5$ as an excitation signal. As seen in the previous chapter, this coded waveform offers a small gain in SNR but a substantial gain in spatial resolution compared to the 8 cycles CF pulse (an improvement of 2.9 dB for a resolution of 0.42 mm against 1.3 mm for the CF 8 cycles pulse, see Table 3.1). The 8 cycles CF pulse was used as a reference to compute the SNR conditions as in (4.40), and to compare the performance of velocity estimation with chirps.

$$\mathrm{SNR} = \frac{< (s \otimes h_{matched\,filter})^2 >}{< (n_{2k} \otimes h_{matched\,filter})^2 >}. \tag{4.40}$$

Fig.4.7 shows the performance obtained for 4 different SNR conditions, a gated range window length of 0.5 μs and 4 transmit/receive cycles. The histograms of the velocity estimates obtained for a displacement of 0.10 λ and 5 dB SNR conditions are also reported in Fig.4.4 for the chirp and Fig.4.5 for the CF pulse. As can be seen, the obtained distributions do not differ much for the two different types of signal, and even in high noise conditions, the estimator remains unbiased (relative bias of 2 %). For all the simulations, it was observed that the bias never exceeded 2% except close to aliasing conditions, as will be described later on.

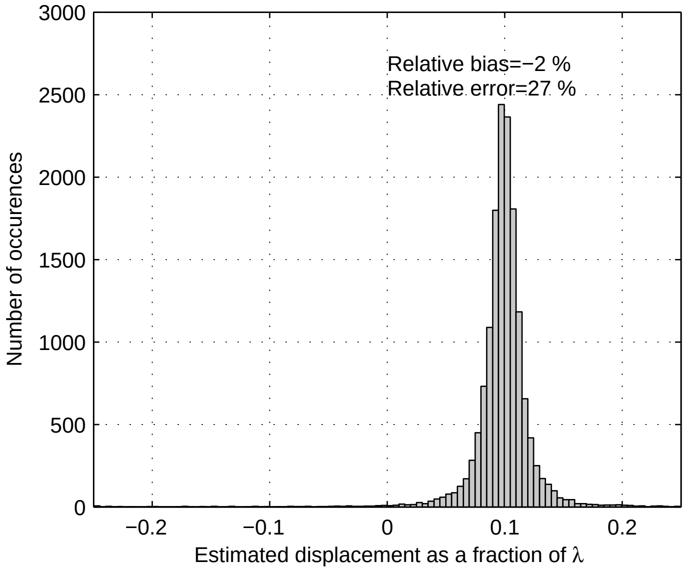

Figure 4.5: Histogram of the velocity estimates obtained for a simulated axial displacement of 0.10 λ, and SNR= 5 dB for the CF 8 cycles pulse.

The moderate gain in SNR provided by the chirp appears to be significantly beneficial in terms of relative precision for relatively poor SNR conditions ($\leqslant$ 10 dB), and for axial shifts below 0.15 λ. For a medium range of SNR (20-30 dB), the performance obtained with the chirp seems to reach a plateau, and the CF pulse achieves a better performance than the coded waveform, which suggests that in this region the performance is essentially driven by the bandwidth of the excitation signal. It can also be noticed that the performance increases with an increasing axial shift up to to 0.15 λ, and then slightly deteriorates, at least at low SNR, for an axial shift of 0.20 λ. An inspection of the histogram in Fig.4.6 shows that this phenomenon is due to the fact that a part of the velocity estimates distribution becomes aliased. The bias observed in this specific situation was obviously higher ($\approx$ 5 %). The phenomenon is accentuated in the case of the chirp.

Fig.4.8 shows the results obtained with the same set of conditions with the simplified modified autocorrelation algorithm. A net overall gain in performance can be noticed with this estimator. A gain in performance is observed with the chirp at the lowest SNR condition for all the axial shifts considered. The previous trend observed in the medium range SNR is confirmed; the performance varies little from 20 dB to 30 dB and a better performance is achieved in the case of the CF pulse (the ultimate relative error goes down to approximately 3 %, whereas it's only of 7.5% in the case of the chirp).

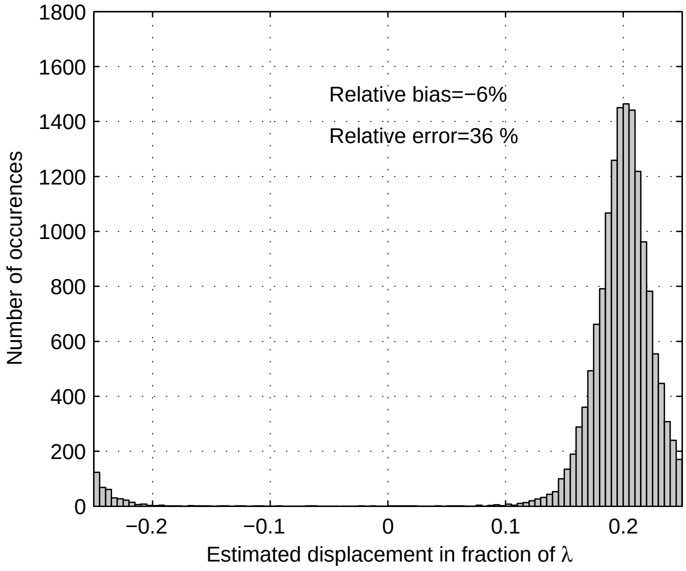

Figure 4.6: Histogram of the velocity estimates obtained for a simulated axial displacement of 0.2 λ, SNR= 5 dB for a chirp $B_f = 0.5$, showing that part of the distribution is aliased.

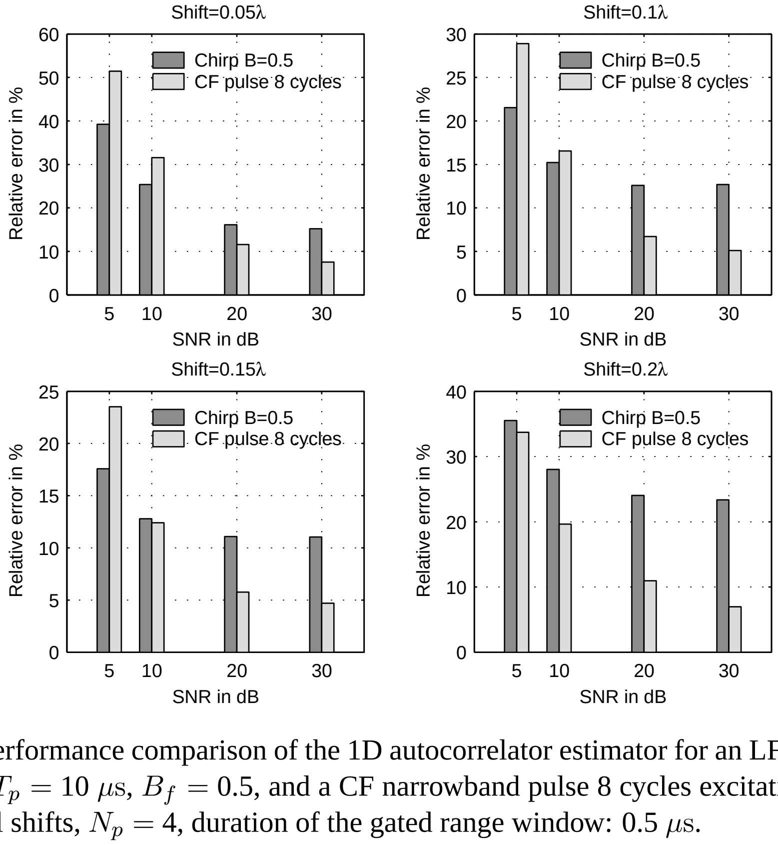

Figure 4.7: Performance comparison of the 1D autocorrelator estimator for an LFM chirp excitation signal $T_p = 10$ μs, $B_f = 0.5$, and a CF narrowband pulse 8 cycles excitation signal, for different axial shifts, $N_p = 4$, duration of the gated range window: 0.5 μs.

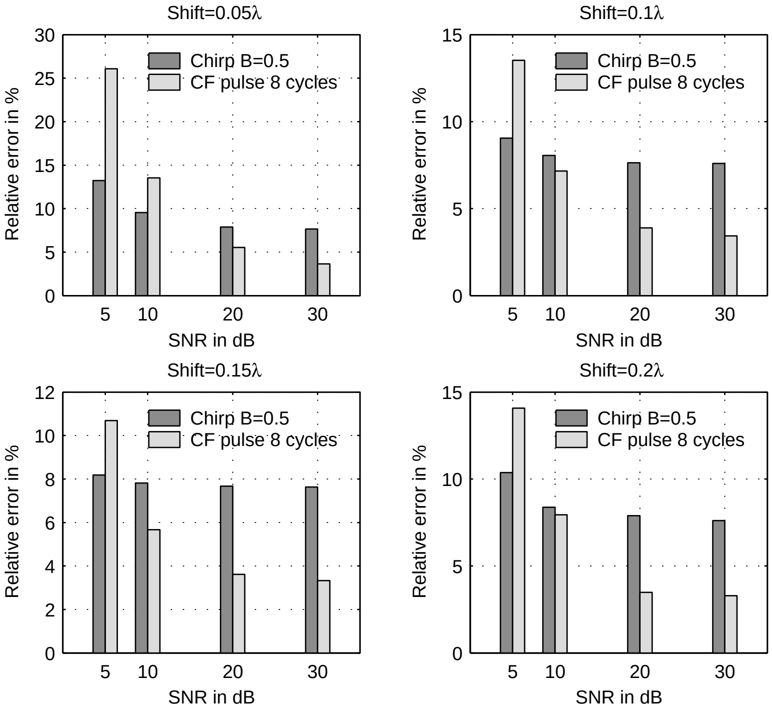

Figure 4.8: Performance comparison of the simplified modified autocorrelation estimator for an LFM chirp excitation signal $T_p = 10$ μs, B_f= 0.5, and a CF narrowband pulse of 8 cycles excitation signal, for different axial shifts. $N_p = 4$, duration of the gated range window: 0.5 μs

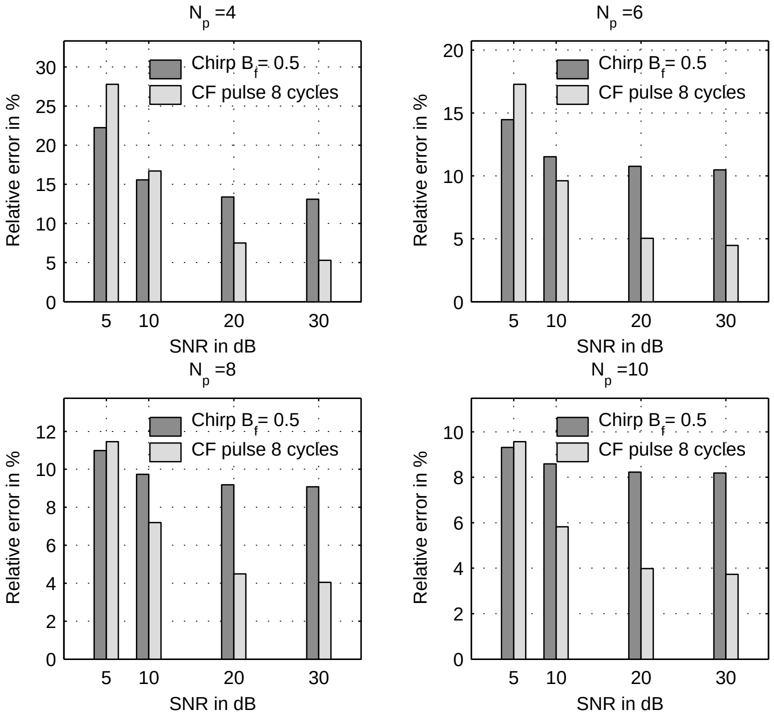

Figure 4.9: Performance comparison of the 1D autocorrelator estimator between an LFM chirp $T_p = 10$ μs, $B_f = 0.5$, and a CF narrowband pulse of 8 cycles, for different N_p, duration of the gated range window: 0.5 μs, axial shift: 0.10 λ.

In Fig.4.9, the axial shift was held constant at 0.10 λ and the number of pulse transmit/receive cycles was varied from 4 to 10 with the 1D autocorrelator algorithm. As the number of pulse transmit/receive cycles is increased, the gain in performance obtained with the chirp becomes less and less evident for the lowest SNR conditions (5-10 dB). Yet, a similar performance level to the CF pulse is maintained in this region of SNR, with an improved spatial resolution.

In the last set of simulations, fig.4.10, the performance of the 8 cycles CF pulse is compared to that of a chirp with a fractional bandwidth $B_f = 0.15$. This waveform offers a good gain in SNR (Table 3.1, Chapter 2), but this time no improvement in resolution is to be expected. As can be seen, the extra gain in SNR provided by the narrowband chirp translates into a significant improvement of the performance up to 20 dB SNR. For an SNR value of 30 dB, the performance of the chirp and the CF pulse converge towards a similar value, which confirms that for a medium range of SNR (20-30 dB) the performance of the 1D autocorrelator is mainly driven by the bandwidth of the transmitted waveform. The same trend is observed in fig. 4.11 in the case of the simplified modified autocorrelation algorithm. The excellent performance achieved in this case suggests that velocity estimation could be performed with this combination

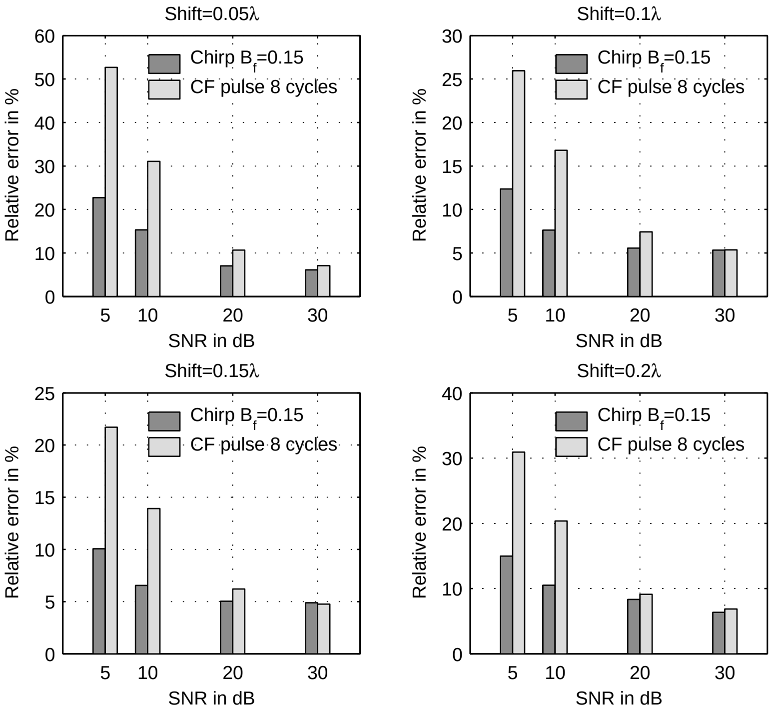

Figure 4.10: Performance comparison of the 1D autocorrelator estimator for an LFM chirp excitation signal $T_p = 10$ μs, $B_f = 0.15$, and a CF narrowband pulse of 8 cycles excitation signal, for different axial shifts, $N_p = 4$, duration of the gated range window: 0.5 μs.

of estimator and coded waveform without any need to further increase the number of pulse transmit/receive cycles.

4.4 Discussion and conclusion

This chapter has presented the principles of phase-shift based velocity estimation in medical ultrasound. Two algorithms were presented : the 1D autocorrelator algorithm and the 2D modified autocorrelation. The potential impact of using coded excitation with this type of estimator has been studied on a theoretical basis as well as with simulations, with LFM chirps as an example of a coded waveform. A theoretical expression was adapted to discuss the potential improvement in statistical performance on a theoretical ground. It was shown that the 1D autoccorrelator estimator is quite robust for a medium packet size ($N_p = 10$) and that potential improvements with SNR are only significant for quite low SNR conditions (below 15 dB). It was also shown that in moderate SNR conditions, the statistical performance is significantly impacted by the fractional bandwidth of the signals, a low fractional bandwidth yields a better

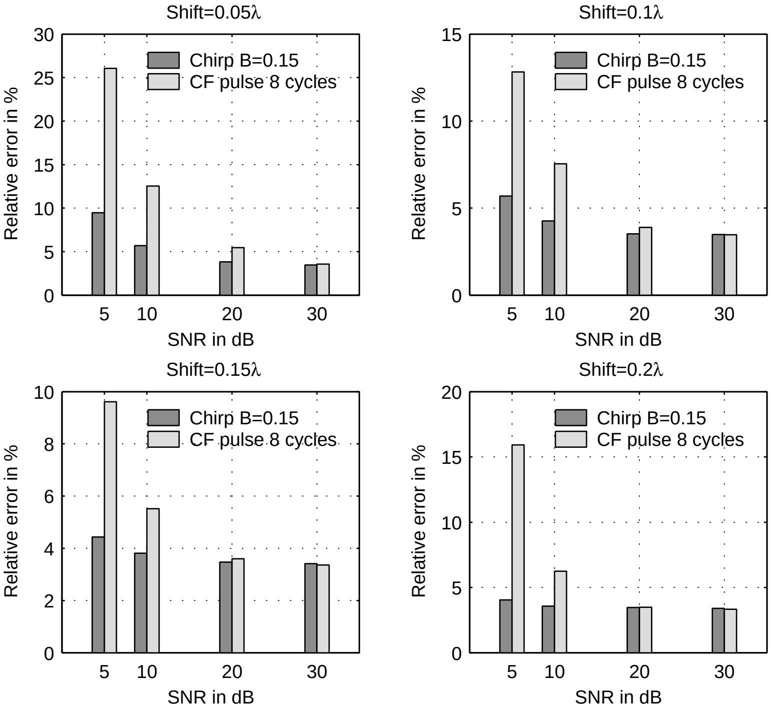

Figure 4.11: Performance comparison of the simplified modified autocorrelation estimator for an LFM chirp excitation signal T= 10 μs, B_f = 0.15, and a CF narrowband pulse excitation signal of 8 cycles, for different axial shifts, $N_p = 4$, duration of the gated range window: 0.5 μs.

performance, which was to be expected given the fact that this estimator works on a narrowband approximation. The set of simulations performed shows that a significant gain in performance and spatial resolution can be obtained for a low range of SNR (10 dB or less) with coded excitation, while maintaining the same transmitted peak pressure amplitude. This suggests that coded excitation could be used to enhance the sensitivity and spatial resolution at long ranges or to achieve the same performance as standard techniques with a limited number of transmit/receive cycles, provided an increase in intensity is permitted. When the SNR conditions are in a medium range (20-30 dB), the simulations confirmed the theoretical results that the performance of phase domain estimators is essentially driven by the bandwidth of the transmitted pulse, which limits any resolution improvement without any performance degradation. These results suggest a spatial resolution / performance trade-off in the use of coded excitation with phase shift based estimators.

Chapter 5

Time-shift based estimation with coded excitation

The goal of this chapter is primarily to investigate the potential benefits of using coded excitation with wideband time-shift based velocity estimation strategies. To understand how the use of coded excitation might be beneficial, it is important to know from a theoretical basis how the performance of these estimators is affected. This chapter thus provides an up-to-date review of the theoretical aspects of estimation performance with time-shift based velocity estimation in the context of medical ultrasound applications. The following questions are central to this chapter:

- Which aspects limit the performance of time-shift based estimators?

- In which situations can the gain in SNR provided by coded excitation be beneficial with this type of estimator? By how much is the statistical performance of the estimator improved?

- Is any gain in resolution possible? i.e. what is the impact of the bandwidth of signals on the statistical performance of estimators?

The first section presents an overview of the current applications of these estimators, followed by their principle and implementation. The second section is dedicated to the study of the theoretical performance aspects. The third section presents some simulations. And finally, the fourth section discusses the possible improvement of performance with coded excitation in the light of the results of sections 2 and 3.

5.1 Time-shift based velocity estimation in medical ultrasound

5.1.1 Motivation of this study in the context of current applications

Dotti et al. [81] appear to have been the first to consider the use of an estimation scheme based on crosscorrelation in the field of medical ultrasound for the measurement of blood flows in 1976. Later on in 1982, Dickinson et al. [82] proposed to measure the displacement of tissues with a correlation method. Interestingly, it seems that it was not until another publication by Bonnefous [83] that this method raised a real interest in the field of medical ultrasound for velocity or displacement estimation. Bonnefous' paper was also probably a milestone in the understanding of current velocity estimation schemes, which do not rely on a "true" Doppler shift as with the early CW techniques. The detailed analysis of the publication clearly demonstrated that the blood flow velocity could simply be inferred from the shift in time that the received signals experience over two successive pulse transmits due to the movement of the red blood cells. A bit later, Bonnefous also proposed a statistical analysis of the performance of the new velocity estimation scheme [84]. Embree presented some experimental results using this method to measure blood flows [67]. Hein implemented a real-time blood flowmeter based on the crosscorrelation technique [85] and checked the obtained statistical performance experimentally [86].

Following closely these early works, several studies showed that the crosscorrelation technique outperformed the 1D autocorrelator in terms of statistical performance [87, 88]. One of the claimed advantage of these techniques over phase shift based estimators is that they do not suffer from aliasing problems [83]. Despite these facts, it is not clear how much current scanners rely on time-shift based estimators for applications like CFI. Evans and McDicken noted in [12, p264] that time shift based estimation had failed so far (in 2000) to be widely introduced in commercial scanners, which they imputed to the large amount of computing power required. Another reason for this may be, as Jensen [13, p245] and Torp in [87] pointed it out, that for applications like CFI, with relatively poor SNR conditions, it is often desirable to use long (narrowband) pulses, which is beneficial to phase-shift domain estimators performance (these was shown in Chapter 4). It is worth mentioning as well that some phase domain estimators such as Loupas' modified autocorrelation actually reach a very close performance to the golden standard of normalised crosscorrelation [11, 89], yet with a much lower computational complexity.

Time-shift based estimators are however nowadays extensively used in research for a number of techniques involving the measurement of either a displacement or a velocity of soft tissues. They are used for instance in the field of elastography [7], in the field of strain and strain rate imaging of the heart [6], for tissue motions estimation [90, 91], or for acoustic radiation force microscopy (ARFI) applications [89]. For all these applications, time-shift based estimators and most particularly normalised crosscorrelation, have gained a widespread acceptance. [6] reports the following benefits compared to phase-shift based estimation technique for strain and strain rate estimation techniques:

- a better axial resolution due to the possibility of using wideband pulses.
- no problem of aliasing
- the possibilty to obtain a displacement or velocity estimate with only two pulse emissions, whereas phase-shift based estimators typically require a few pulses to yield a robust estimate. (This is particularly important in elastography, because usually only two signals are acquired: a pre-compression signal and a post-compression signal).
- the method is more robust to frequency dependent attenuation.

A recent comparison study [92] confirmed the better robustness of time-shift based tissue speckle tracking for strain estimation compared to phase-shift based estimation. The authors also hypothesised that time-shift based estimation is a lot more robust to large deformation of the scattering medium than phase shift based estimation.

A clear drawback of these techniques is that they are inherently computationally intensive, and have a higher hardware cost compared to a relatively simple algorithms like the 1D autocorrelator. According to [6], it was still hard in 2002 to obtain fully real-time strain imaging system, with a good temporal resolution (high frame rate), with this type of estimator (obviously the amount of post-processing required is also a challenge, and for some applications, off-line processing might still be unavoidable). It is likely that with the constant gain in computing power over time, this will become less of an issue in the future, but a good engineering solution is always a trade-off between costs, simplicity of implementation and performance. This may particularly be important in the context of this study, because the use of coded excitation with a matched filter already adds a significant extra computational complexity to the system. In the first real-time blood flowmeter solutions proposed, the full crosscorrelation of the signals could not be evaluated, instead, a much simpler method was implemented, called “crosscorrelation using the sign”, or polarity coincidence method. In fact, a set of time-shift based estimators are known to provide only slightly degraded performance compared to the normalised crosscorrelation, and a potentially lower hardware cost [93], like the Sum of Absolute Difference (SAD) algorithm or the Sum of Squared Difference (SSD) algorithm , which will be presented in the next section. These estimators seem to have been studied only in very few papers in the field of medical ultrasound ([94] and [95], essentially).

5.1.2 Principle of time-shift based estimation and description of the algorithms

The time delay Δt between the received signals from a single target moving at a velocity v between two pulses transmits emitted at a time interval T_s is equal to:

$$\Delta t = \frac{2vT_s}{c} \tag{5.1}$$

A measure of Δt readily leads to the target displacement between the interval T_s or the mean velocity during the same time interval. In a practical case for medical ultrasound applications, the received signal r can be described, using a linear system description approach, by the convolution between the transmitted signal s and a scattering function f which depends on the spatial scatterers distribution and backscattering power:

$$r_1(t) = s \otimes f_1 = \int s(u) f_1(t-u) du \tag{5.2}$$

After a second transmit, the scatterers have moved yielding the second received signal:

$$r_2(t) = s \otimes f_2 = \int s(v) f_2(t-v) dv \tag{5.3}$$

If we now examine the crosscorrelation of the two received signals, by definition of the crosscorrelation function $R_{r_1 r_2}$:

$$R_{r_1 r_2}(\tau) = \int r_1(t) r_2(t+\tau) dt = \int \int \int s(u) s(v) f_1(t-u) f_2(t+\tau-v) du dv dt \tag{5.4}$$

This relatively complex integral can be simplified if we consider that :

- the reflectivity functions are ideally δ-correlated i.e. their autocorrelation function is a

Dirac impulse (the fluctuations in compressibility and density of the medium from which backscattering arise have a correlation length much smaller than the wavelength of the pulse, as in the model of Chapter 3).

- f_2 is simply a time-translated version (time delay Δt) of f_1, due to a uniform movement of scatterers between the two pulse transmits: $f_2(t) = f_1(t - \Delta t)$.

We then have the following property:

$$\int f_1(t-u)f_2(t+\tau-v)dt = \delta(u-v+\tau-\Delta t) \tag{5.5}$$

The preceding equation then simplifies into:

$$R_{r_1 r_2}(\tau) = \int s(u)s(u+\tau-\Delta t)du = R_{ss}(\tau-\Delta t) \tag{5.6}$$

which shows that the crosscorrelation function of the received signal is simply the autocorrelation function of the transmitted signals shifted in time correspondingly to the displacement of scatterers. In particular, a measure of the position of the peak of the crosscorrelation function will yield the desired time delay Δt. In this idealised model, the shape of the crosscorrelation function only depends on the transmitted signals; transmitting a wideband signal should thus yield a sharp correlation peak, and thus, a good statistical performance. In real conditions of course, Eq. 5.5 is only an approximation, and f_1 and f_2 are not δ-correlated. As a consequence, the correlation peak may be significantly broadened (also called "decorrelation" of signals). In particular, the hypothesis that f_2 deduces from f_1 by a simple translation requires that the medium probed undergoes a uniform translation, and that all the scatterers remain in the insonified volume, which is more or less realistic. Intuitively, however, this hypothesis will be a good approximation for small displacements (or a small time interval between the pulses transmits); and if the volume probed is not too large.

5.1.3 Practical implementation

Apart from the possible decorrelation between the two successively received signals, two factors at least may impact on the performance of this method in a practical implementation. The first of these factors, is that, to obtain a local measure of the displacement, the received signals are range gated and crosscorrelation is thus only performed on short segments of signals. The size of the range gate duration is of a great importance. As it will be seen, it can have a significant impact on the accuracy of the method: a large window duration increases the performance; but also reduces the spatial information provided by the estimates. This parameter can also depend on the type of application. Walker et al. [96] reports typical values of gated range window duration as 0.65 μs for blood flow estimation applications and 1.3 μs for strain estimation applications. Another difficulty is that due to the sampled nature of signals, the ultimate shift in time determined by the position of the peak may only be, in principle, determined as an integer multiple of the sampling period. For most applications in medical ultrasound, even at a relatively high sampling rate (say, 50 MHz), the time delays to be measured are only a few sampling periods, the obtained time resolution is thus far too coarse. For this reason, the croscorrelation function has to be interpolated around its peak to yield a more accurate estimate. This is usually done by fitting a parabola through three consecutive samples at the position of the maximum. The method was originally described in [97]. If $R(l_{coarse})$ is the peak value of the sampled correlation function (l_{coarse} is the index which corresponds to the crosscorrelation peak) then the fractional index value l_{fine} that defines the position of the peak fitted by a parabola is given by [11]:

$$l_{fine} = \frac{1}{2}\frac{R(l_{coarse}-1) - R(l_{coarse}+1)}{R(l_{coarse}-1) - 2R(l_{coarse}) + R(l_{coarse}+1)} + l_{coarse}. \tag{5.7}$$

Finally, other estimators than crosscorrelation may be used, on a similar principle. The following estimators were implemented in this study, T corresponds to the range gate duration, r_1 and r_2 are two received successive signals:

- The normalised crosscorrelation estimator (NXC)

$$R_{NXC}(\tau) = \frac{\int_{-T/2}^{T/2} r_1(t) r_2(t+\tau) dt}{\sqrt{\int_{-T/2}^{T/2} r_1^2(t) dt \int_{-T/2}^{T/2} r_2^2(t) dt}}. \tag{5.8}$$

  The presence of the denominator normalises the crosscorrelation function, i.e. when the signals perfectly correlate, the peak value is equal to one. The peak value is also called the correlation coefficient ρ, this coefficient measures of the "decorrelation" of the signals (see previous paragraph). Thus, in general, unless $r_2(t)$ is a perfect time-translated version of $r_1(t)$, ρ is inferior to one.

- Crosscorrelation using the sign (Xsign)

$$R_{XSign}(\tau) = \int_{-T/2}^{T/2} sign(r_1(t))sign(r_2(t+\tau))dt, \tag{5.9}$$

where the sign function returns 1 for a positive signal value and -1 for a negative signal value. This estimator is also sometimes called the Polarity Coincidence Correlation estimator.

- Sum of Absolute Differences (SAD)

$$R_{SAD}(\tau) = \int_{-T/2}^{T/2} |r_1(t) - r_2(t+\tau)|dt \tag{5.10}$$

- Sum of Squared Differences (SSD)

$$R_{SSD}(\tau) = \int_{-T/2}^{T/2} |r_1(t) - r_2(t+\tau)|^2 dt \tag{5.11}$$

For these last two estimators, the time shift Δt is estimated as the minima positions of the functions.

5.2 Theoretical study of the statistical performance of time-shift based estimators

5.2.1 Theoretical aspects of the statistical performance of crosscorrelation

The performance of time delay estimation with crosscorrelation has been a very intensively studied problem in signal processing from the early eighties ([98], [99], [100], [101], [102], for instance, and a more recent review is given in [103]). In the field of medical ultrasound, different works have studied the performance of the crosscorrelation estimator. One of the first analysis was due to Bonnefous [84]. Foster [104] proposed an analysis of the performance based on a similar approach used in the radar field, and studied the impact of a lot of different parameters on the statistical performance with simulations. Jensen also proposed an expression for the variance of the estimates in[13] based on [105]. [12, p271] gives an excellent review of the work carried out in this area in medical ultrasound, while pointing out that the individual results of different studies do not seem to be entirely compatible. This can be imputed to the various simplifying assumptions in the derivation of these expressions. In fact, it seems that an indirect approach based on the derivation of the Cramer-Rao Lower Bound (CRLB) for the time delay estimation problem yields the most accurate method. By definition, the CRLB bound is a theoretical limit for the variance of any unbiased estimator, based on the behaviour of a maximum likelihood estimator; it is thus *a priori* not sure how crosscorrelation performs compared to this ideal bound. Several studies have however confirmed that crosscorrelation was able in some conditions to reach this bound [103]. This approach was introduced to the field of medical ultrasound by Walker et al. [96]. In this study, Walker first makes the interesting comment that in the presence of noise, the crosscorrelation estimation technique typically suffers from two types of error:

- the first type is some small errors, referred to as “jitter” errors, which are due to small deviations in the location of the peak of the crosscorrelation function around its true value.

- the second type is called “false peak” errors and occurs when the maximum peak of the crosscorrelation peak is not the true peak, but an adjacent peak. This results in much larger error amplitudes.

Walker mentioned that false peak errors can be removed in practise *via* non linear filtering (although this would also supposedly reduce the spatial information of the estimated displacements or velocities) whereas jitter errors can not be suppressed, and thus place a fundamental limit on the performance of crosscorrelation. He was finally able to conclude, with some extensive simulations, that the CRLB bound accurately predicts the jitter of crosscorrelation estimates, in a relatively large set of conditions relevant to medical ultrasound parameters.

5.2.2 Analysis of the CRLB

The expression obtained by Walker et al. in [96] for the CRLB was based on [98]. The expression was adapted to medical ultrasound applications, by considering the case when the two signals received are decorrelated speckle signals (introduction of the correlation coefficient ρ in the expression). This yields the following theoretical performance bound [96].

$$\frac{\sigma_{\Delta t}}{\Delta_t} \geqslant \frac{\sigma_{CRLB}}{\Delta t} = \frac{1}{\Delta t}\sqrt{\frac{3}{2f_0^3\pi^2 T(B_f^3+12B_f)}\left(\frac{1}{\rho^2}\left(1+\frac{1}{\mathrm{SNR}}\right)^2-1\right)}, \tag{5.12}$$

where $\sigma_{\Delta t}$ is the standard deviation of estimated time delays, σ_{CRLB} is the theoretical CRLB bound on the standard deviation of time delay estimates. Fig.5.1 plots the obtained relative errors for three displacements, expressed as a fraction of the wavelength (0.10 λ, 0.20 λ and 0.40 λ). The other parameters in Eq.5.12 were set to $f_0 = 5$ MHz, $T = 1$ μs, $B_f = 0.5$, and $\rho =$ 0.98, which according to [96] is a typical correlation coefficient found for blood signals, taken here as an example. A noticeable aspect of the performance is that the relative error depends on the inverse of the quantity to be estimated (factor 1/ Δt in 5.12). As a consequence, larger velocities or displacements (relatively to a given PRF) should always benefit from a lower relative error. A second noticeable feature is that in the presence of decorrelation ($\rho < 1$), the error does not decrease to zero, but instead, the curve demonstrates an asymptote, which depends on the displacement to be measured, the correlation coefficient and the time duration of the window used T. The equation of the asymptote for high SNR is readily obtained from Eq.5.12:

$$\lim_{SNR \to +\infty} \frac{\sigma_{CRLB}}{\Delta t} = \frac{1}{\Delta t} \sqrt{\frac{3}{2 f_0^3 \pi^2 T (B_f^3 + 12 B_f)} \left(\frac{1}{\rho^2} - 1 \right)} \tag{5.13}$$

Fig. 5.2 shows the evolution of the relative error for an axial displacement of 0.10 λ and different fractional bandwidths of the received signals. As expected, the performance improves with the bandwidth of signals, which shows that the crosscorrelation technique is clearly a “wideband” estimation strategy. The curves show that the performance can be quite deteriorated for low fractional bandwidths and low SNR conditions. Finally, Fig. 5.3 shows the performance obtained for the same set of parameters, a displacement of 0.10 λ and three different T values : 1 μs, 2 μs and 4 μs, which correspond to distances of respectively of 0.8 mm, 1.84 mm and 3.1 mm. The improvement in relative error is quite slow when increasing the duration of the gated range window (as $1/\sqrt{T}$, according to 5.12), but as can be clearly seen, there is a trade-off between resolution and performance, large T values provide a more robust estimate, especially in the low SNR region, but the spatial resolution is also decreased. In practical applications, it should however be noted again that the ultimate spatial resolution can also depend to a large extent on the signal processing chain of the data (overlapping of windows, median filtering, etc...).

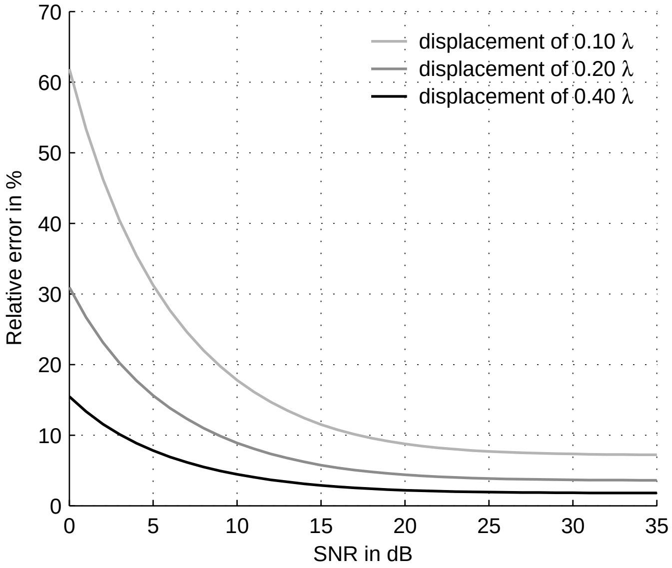

Figure 5.1: Plot of the CRLB performance bound, for three displacements (0.10 λ, 0.20 λ and 0.40 λ); $f_0 = 5$ MHz, $T = 1$ μs, $B_f = 0.5$, and $\rho = 0.98$.

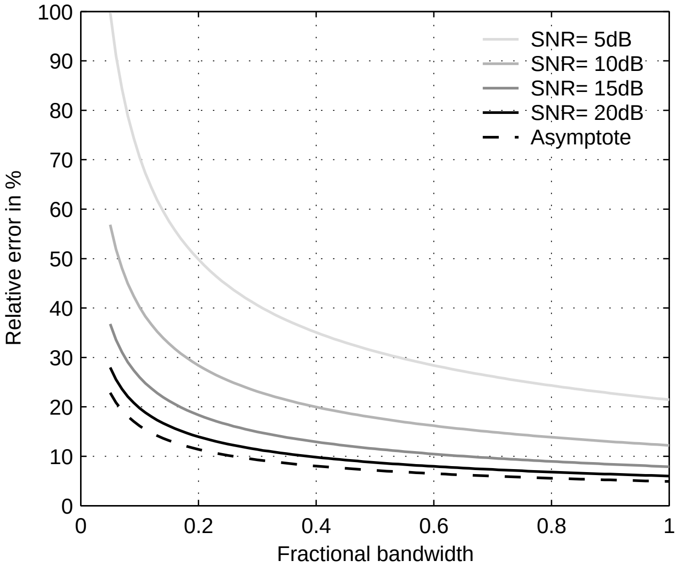

Figure 5.2: Plot of the CRLB performance bound with the fractional bandwidth of signals, for a displacements of 0.10 λ, and five different SNR conditions (5 dB, 10 dB, 15 dB, 20 dB, ∞), $f_0 = 5$ MHz, $B_f = 0.5$, and $\rho = 0.98$,$f_0 = 5$ MHz.

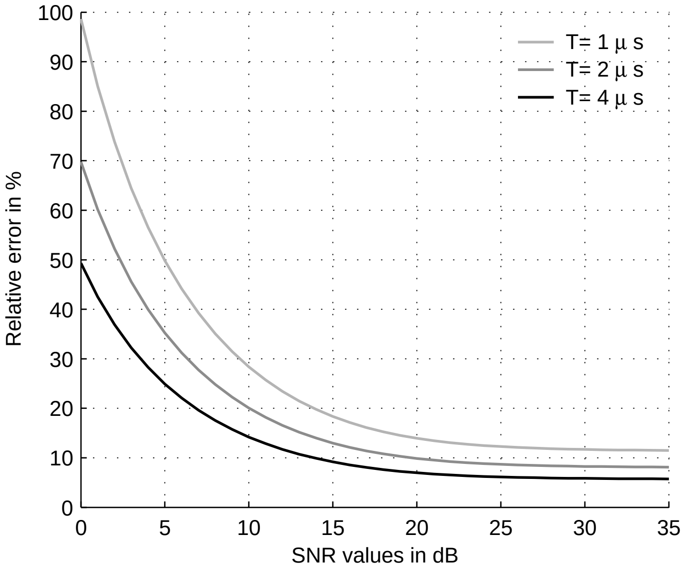

Figure 5.3: Plot of the CRLB performance bound with the time duration of the gated range window against the SNR conditions, for a displacement of 0.10 λ, $f_0 = 5$ MHz, $B_f = 0.5$, and $\rho = 0.98$. $f_0 = 5$ MHz.

5.2.3 Limitations of the CRLB approach

5.2.3.1 Decorrelation of signals

The model adopted by Walker et al. incorporates the decorrelation of signals as a loss in amplitude of the normalised correlation peak of the signal but does not really account for the broadening of the correlation peak, essentially the normalised crosscorrelation of the signals is considered as a scaled version of the autocorrelation of one of either of the received signals:

$$R_{r_1 r_2} = \rho R_{r_1 r_1} \tag{5.14}$$

Cespedes [106] showed the equivalence between the effect of an electric noise and the decorrelation of signals as described by Eq.5.14 in the CRLB bound Eq.5.12. In particular an equivalent "decorrelation SNR" SNR_ρ can be defined as:

$$\frac{1}{\rho} = 1 + \frac{1}{\mathrm{SNR}_\rho} \tag{5.15}$$

Conversely, the term $1 + \frac{1}{\mathrm{SNR}}$ in Eq.5.12 can be replaced by an equivalent decorrelation term $1/\rho$ using the same expression. It follows from Cespedes' analysis that with the model of decorrelation of signals of Eq.5.14, decorrelation can be interpreted as an additional stationary and uncorrelated noise term. Whether decorrelation can be treated as such, in practise, is however not clear. In general as well, the decorrelation of signals can be a function of parameters such as the centre frequency or the time delay to be estimated itself, which gives a more complex dependence of the bound of Eq.5.12 to these parameters. According to [84], for instance, an approximate expression for ρ is given by:

$$\rho = \left[1 - \frac{\delta_{tran}}{BW}\right](1 - 2\pi^2 f_0^2 \sigma_{[\Delta t]^2}) \tag{5.16}$$

The first term in the preceding equation shows the effect of decorrelation due to the scatterers leaving the sample volume, and depends on the transverse displacement component of the scatterers δ_{tran} and the ultrasound beam width BW. This term clearly approximates the lateral beam fall-off as rectangular window of size BW. The dependence of ρ on the time shift to be estimated can be made more explicit: suppose the axial shift to be measured is δ_{axial}, giving rise to a shift in time Δt, then the transverse displacement is given by:

$$\delta_{tran} = \delta_{axial}\tan\theta = \frac{c\Delta t}{2}\tan\theta \tag{5.17}$$

where θ is the angle of the trajectory of scatterers with the axis of the transducer. The second term in this expression is a decorrelation factor due to the velocity spread in the sample volume, which is taken into account as a spread in the time shift to be estimated, characterised by a variance $\sigma_{[\Delta t]^2} =< \Delta t^2 >$, and is proportional, according to Bonnefous' analysis to the square of the centre frequency of the signals.

5.2.3.2 SNR model and spectral characteristics of signals

Another limitation in the expression presented in Eq.5.12 is the model of the spectral characteristics adopted for the signals, which was chosen to be rectangular (that is constant power densities in the bandpass) for simplicity of derivation. Moreover, [96] considers a basic SNR model, independent of the bandwidth of signals. A more realistic SNR model, as presented in section 3.3 (Chapter 3), shows that the SNR after a matched filter (or a simple bandpass filter adapted to the bandwidth of the transmitted CF pulse) has a dependence as $1/B^2$. To obtain some insights into the performance with this SNR model, one can arbitrarily define a reference SNR_{ref} for a fractional bandwidth B_f = 0.5, an effective SNR taking into account the

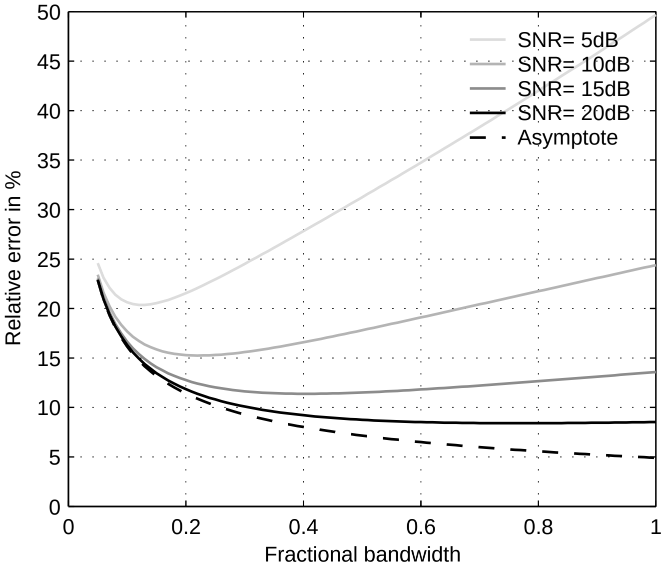

Figure 5.4: Plot of the CRLB performance bound with the fractional bandwidth of signals with a more realistic bandwidth-dependent SNR model, for an axial displacement of 0.10 λ, and four different SNR conditions (5 dB, 10 dB, 15 dB, 20 dB).

proposed SNR model is then simply given by:

$$SNR_{eff} = SNR_{ref}/4B_f^2 \tag{5.18}$$

Substituting the SNR term in 5.12 by SNR_{eff} then yields the performance bound:

$$\frac{\sigma_{\hat{\Delta t}}}{\Delta_t} \geqslant \frac{1}{\Delta t}\sqrt{\frac{3}{2f_0^3\pi^2 T(B_f^3+12B_f)}\left(\frac{1}{\rho^2}\left(1+\frac{4B_f^2}{\mathrm{SNR}_{ref}}\right)^2-1\right)} \tag{5.19}$$

This modified bound was plotted for different SNR_{ref} values in Fig.5.4, with the same set of conditions as in Fig.5.2. As can be clearly seen, the performance curves demonstrate a minimum for low SNR, which confirms that even with a wideband estimation strategy, it advantageous to use narrowband pulses when the SNR conditions become too poor. In particular, the curves show that for an SNR of 5 dB (with the reference used of a pulse with a fractional bandwidth B_f = 0.5), the performance is bounded with a minimum relative error of 20 %, which shows that crosscorrelation cannot be used to yield very good estimates in such conditions without additional averaging. When the SNR conditions becomes higher, the best performance is achieved for increasing fractional bandwidths.

5.2.3.3 Limit of validity of the CRLB

Following Walker's analysis of the different regimes of performance of the crosscorrelation estimator, it seems interesting to know in which conditions the performance can deviate from the CRLB, that is, in which conditions the crosscorrelation estimator switches from a small error regime ("jitter") to a large error regime i.e. "false peak" estimation regime. For medical ultrasound applications, this is particularly important because a good performance (about 10 % relative error) is only achievable in the jitter error regime, the false peak regime requires some further non-linear processing, which is not ideal. [96] concluded that the CRLB is valid when the SNR is fairly high and the correlation between signals is also high, without any further precision. The problem of false peak error estimates was also studied in the field of medical ultrasound by Jensen in [107]. His study showed that below a certain SNR threshold, the probability of detection of the correct peak drops sharply, the threshold observed was of approximately 5 dB.

In fact, it can be inferred intuitively that the SNR conditions or the decorrelation of signals are not the only parameters driving the transition between the two regimes of errors. Recall from our idealised model that the crosscorrelation function of two speckle signals is essentially the shifted autocorrelation of the transmitted signals. Fig.5.5 plots the autocorrelation function of a 4 cycles CF pulse, and that of a 10 cycles CF pulse. Clearly the autocorrelation peak is sharper for a relatively wideband 4 cycles CF pulse, meaning that crosscorrelation estimates with wideband signals should be less prone to a false peak detections (for an equivalent level of noise). Clearly as well, the autocorrelation function is periodical with a period equal to the period of the transmitted signals. A way to avoid false peak detection error is thus to restrict the interval of search of the correlation to $[-\frac{1}{2f_0}, +\frac{1}{2f_0}]$. This, however, restricts the maximum velocity that can be estimated. Not surprisingly, this interval corresponds exactly to the non-aliased range of velocities that can be estimated with phase domain estimators. This shows intuitively that with crosscorrelation, it can become quite difficult to measure velocities beyond the Nyquist limit, at least in poor SNR conditions, because large errors are introduced by false peak detection. Jensen mentioned this difficulty in [107], and proposed several methods to overcome this limitation.

The problem of large errors with crosscorrelation estimates in poor SNR conditions appears to also have been studied in the field of signal processing. Ianniello [108] proposed an analytical expression of the probability of "detection anomaly" with crosscorrelation. He also

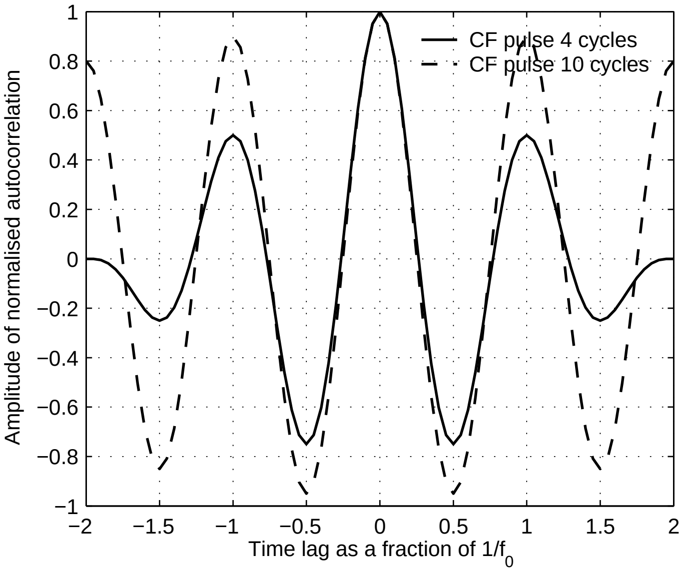

Figure 5.5: Autocorrelation function of a 4 cycles and a 10 cycles CF pulse, with the time lag expressed as a fraction of their period $(1/f_0)$.

concluded that signals with narrow-band spectra or with large sidelobes have a greater probability of an anomalous estimate due to the relative large values of the autocorrelation function at time delays removed from zeros. Finally, a global description of the theoretical behaviour of the crosscorrelation estimates was achieved by Weiss et al. using the Ziv-Zakai bound [101][102]. Essentially, the following bounds were obtained for the variance of the time delay estimates:

$$\sigma^2_{\hat{\Delta t}} \geqslant \begin{cases} \dfrac{D^2}{12} & BTSNR' < \gamma \\ \text{Threshold} & \gamma < BTSNR' < \delta \\ \text{Barankin bound} & \delta < BTSNR' < \mu \\ \text{Threshold} & \mu < BTSNR' < \eta \\ \text{Cramer-Rao bound} & \eta < BTSNR' \end{cases} \tag{5.20}$$

Where the SNR' is defined as, given the signal power S and the noise power N:

$$SNR' = \frac{(S/N)^2}{1+2(S/N)} = \frac{\text{SNR}^2}{1+2\text{SNR}} \tag{5.21}$$

D is the interval of search of the correlation peak, B is the bandwidth of the signal in Hz, γ, δ, μ, η are different threshold values delimiting the different regions of performance. In this framework, the performance in a large error regime is described by the Barankin bound (this bound simply exceeds the CRLB by a factor $12/B_f^2$), and ultimately the performance is bounded by D^2/12, that is, the peak of the crosscorrelation function is completely randomly located in the interval [-$D/2$, +$D/2$]. In this last case, no velocity or displacement information can be retrieved. An interesting aspect is that both the time of observation of signals T, their bandwidth B, and the SNR as described by Eq.5.21 determine through their product in which region of performance the estimator operates. As is easily understood according to this analysis, a relatively large TB product has to be achieved when the SNR is poor to operate in the small error regime described by the CRLB. Increasing the bandwidth is however detrimental to the SNR conditions, and increasing T, the size of the gated range window, ultimately decreases the spatial information the estimates provide. Finally, it can be mentioned that this bound was applied to the field of elastography by Varghese [109]. The author was able to provide a qualitative agreement between the standard deviation of strains obtained with simulations and the bounds described by Eq.5.20, and concluded that a robust strain estimation can only be performed in the CRLB regime.

5.2.4 Discussion on the potential improvement of the performance with coded waveforms

As seen in the previous paragraph, the CRLB corresponds to a small error regime, which can only be achieved within certain conditions in terms of SNR and decorrelation of signals, which are yet not unrealistic. This is thus an interesting tool to study the potential of coded excitation techniques to improve the performance of time-shift based estimation. Inspection of Fig.5.1 clearly shows that when the SNR conditions are relatively poor, a gain in SNR with coded excitation is promising in decreasing the relative error, especially for the estimation of small displacements. For velocity estimation, this corresponds to cases when the PRF cannot be increased (high depth for example), or low blood flow velocities. Note, however, that in the case of slow velocity estimation (slow relatively to a given PRF), if the scatterers remain in the beam for P pulse transmits, it is always possible to crosscorrelate signals that are received kT_s apart ($k \in [2, P-1]$) instead of crosscorrelating adjacent signals to yield a smaller relative error [85]. The velocity is then simply inferred from:

$$v = \frac{c\Delta t_k}{2kT_s} \tag{5.22}$$

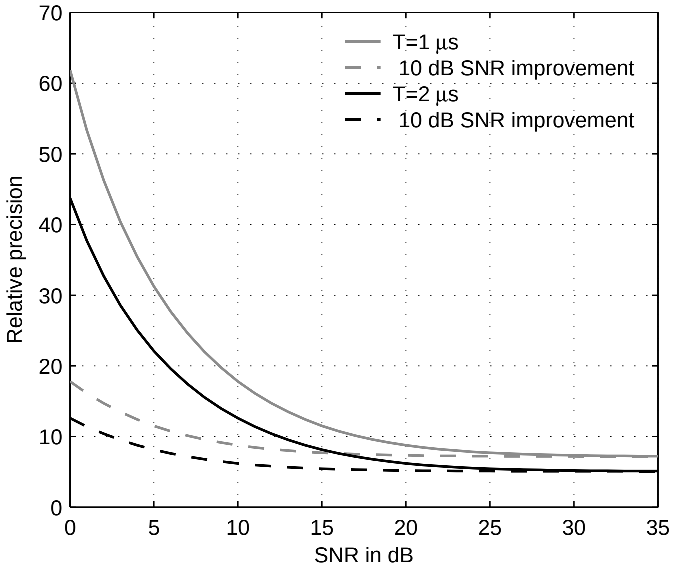

Figure 5.6: Plot of the CRLB performance bound two different gated range window durations $T = 1$ μs and $T = 2$ μs, $B_f = 0.5$, for an axial displacement of 0.10 λ, against the SNR conditions and effect of 10 dB SNR improvement.

where Δt_k is the shift in time measured when crosscorrelating signals received kTs seconds apart. The graph in Fig.5.6 shows the potential impact of an increase of 10 dB in the SNR for an axial displacement of 0.10 λ. For an SNR of 5 dB and a time duration of $T = 1$ μs, the relative error goes from 30 % to about 10 %, which is quite an important gain in terms of performance. The gain observed for $T = 2$ μs is not as large, but remains significant. Realistic gains in SNR for some coded waveforms over CF pulses of different cycles were presented in section 3.3.4 (Chapter 3). Since crosscorrelation is a wideband estimation scheme, a 4 cycles CF pulse is chosen as an appropriate reference to be compared with. The following table reports the gain in SNR measured over 4 cycles CF pulse, for coded waveforms having a spatial resolution comparable to or superior to the chosen 4 cycles reference pulse (approximately 0.68 mm, when using the FWHM and the simulation parameters of section 3.3.4). As can be seen, an improvement of 5 to 10 dB with coded excitation is quite realistic, even with coded waveforms having a moderate duration (from 4 μs to 10 μs). For CFI applications, coded excitation could thus bring the boost in SNR necessary to perform robust blood flow estimation without the need to reduce the bandwidth (and thus the spatial resolution) of the transmitted signals.

On the contrary, it appears from Fig.5.1 and Fig.5.6, that for a medium range of SNR (20-30 dB), the performance of the crosscorrelation estimator is not significantly affected by the SNR conditions and reaches an asymptotic curve which depends on the level of decorrelation of

Coded signal	GSNR (dB)	T_p (μs)	Resolution (mm)
Chirp $B_f = 0.50$	8.91	10 μs	0.42
Chirp $B_f = 1.00$	4.41	10 μs	0.26
Barker 5 bit 4 cyc.	4.99	4.0 μs	0.69
Barker 13 bit 2 cyc.	7.51	5.2 μs	0.37
Barker 13 bit 4 cyc.	11.31	10.4 μs	0.69

Table 5.1: Different coded waveforms and the SNR improvement they achieve over a 4 cycles pulse along with their time duration T_p, and the spatial resolution, measured as the FWHM of the compressed pulse. The reference 4 cycles CF pulse has an axial resolution of 0.68 mm

signals and the length of the gated range window used, as previously described. As pointed out by [96], this means that apart from blood flow applications which typically suffer from low SNR conditions, the performance of estimation with time shift based estimators is bounded by the physical decorrelation of signals. As seen previously, decorrelation essentially depends on the physical deformation of the medium in the volume probed (with potentially a non-uniform velocity field across the sample volume). Consequently, the use of coded excitation should not have a major impact on the performance for applications with a moderate to large SNR (say above 15 dB) (it was shown in Chapter 2 , in particular, that the sample volume obtained with a coded waveform after compression is similar to that obtained for a wideband CF pulse, essentially the axial resolution is perturbed by the range sidelobes, but the transverse resolution is the same).

This however is only true in the CRLB regime, and the limitations of this bound, as pointed out in the previous subsections, may balance this conclusion. A first limitation concerns the decorrelation of signals, it is not clear whether the simple proposed model fully grasps the combined impact of physical decorrelation and the SNR conditions on the performance of estimation. A further limitation of [96] is that the crosscorrelation peak search interval was limited to the Nyquist range and used relatively large time windows (4 μs). If a larger interval was searched and a smaller window used, the crosscorrelation could significantly depart from the jitter operation mode at a relatively higher SNR than what is observed in [96]. Following the analysis developed by Weiss and presented in the previous subsection, this depends on the TB product used. A clear potential performance improvement by coded excitation could thus be the possibility to achieve the large $TBSNR'$ product necessary to operate in a small error regime. In particular, coded excitation could offer the possibility to increase the bandwidth of signals (B) while improving the SNR conditions. This would effectively give the ability to measure displacements or velocities beyond the Nyquist limit without the need to remove false peaks by any non-linear processing methods. This could be very useful in blood flow estimations studies, when aliasing is a factor limiting high temporal resolution. Another potential application is elastography, which requires the estimation of relatively large displacements (between λ/4 and 10λ, according to [89]).

5.3 Study of the performance with simulations

5.3.1 Study of the systematic error introduced by interpolation of the peak of the crosscorrelation

The necessary interpolation of the crosscorrelation peak can introduce a systematic error in the crosscorrelation estimates. One of the simplest solutions is the parabola fitting method, as introduced in Eq. 5.7, but some other methods have also been considered and studied [90, 110, 111]. The effect of parabola interpolation was also specifically studied in the field of strain estimation [112]. None of these studies, however, has investigated the potential impact of interpolation on the performance using some other estimators than crosscorrelation. In this section, we propose to study the bias introduced by the parabola interpolation scheme on the different time-shift based estimators introduced in subsection 5.1.3. For the SAD and the SSD estimators, the principle of interpolation is the same, except that a minimum has to be interpolated instead of a maximum. Synthetic signals were generated according to the model of section 4.3.2 (Chapter 4), using a 4 cycles pulse, but no noise was added to the signals. The bias was computed as the sample mean of the difference between the estimated time delay and the true time delay using 1000 gated range independent window realisations of length $T = 1$ μs. The same parameters used in section 4.3.2 were used, and are repeated here for convenience: centre frequency $f_0 =$ 5 MHz, fractional bandwidth of the transducer: $B_f =$ 0.5.

The following graph Fig.5.7 compares the results obtained for the NXC, SSD, SAD and Xsign estimators for different time delays, expressed as a fraction of the sampling period (with the parameters used the maximum time delay tested corresponds to an axial displacement of 0.10 λ). As can be seen, for all the estimators except Xsign, the bias exhibits a periodical character. For Xsign and SAD, the parabola can introduce a bias of up to 8-9% in the time delay estimate with the parameters used, depending if relatively small time delays are to be measured. On the contrary, the bias obtained for the SSD and NXC are very similar, and appear to be approximately one order of magnitude below the two other estimators.

Fig 5.8 and 5.9 show some typical outputs of the different estimators as a function of the time lag, for a simulated axial displacement of 0.1 λ, plotted for a gated range window duration $T = 2\ \mu\mathrm{s}$. It is first noticeable that all these curves exhibit the same periodicity (period of $1/f_0$ with the time lag), therefore all the estimators tested should be prone to false peak detection in the presence of poor SNR conditions. A potential explanation for the observed differences in the performance of the parabola interpolation can be explained by the fact that the R_{SAD} and R_{XSign} functions exhibit a much sharper peak than the R_{NXC} and R_{SSD} . The curves seem to demonstrate a singularity at their extremum (discontinuity in the first derivative of the curve), that may not be well interpolated by a smooth parabola curve. To test this hypothesis, a new interpolation scheme is proposed which simply relies on a linear interpolation of the functions at their extremum. Fig 5.10 shows the basic geometry when the minimum of the curve has to be interpolated (case of SAD). The interpolated minimum of the curve is at point A, the position of which is found so that the points $R(l_{coarse-1})$, A and B form an isosceles triangle. This yields the following lag l_{fine} for the position of the interpolated minimum of the curve at point A:

$$l_{fine} = \begin{cases} l_{coarse} + \dfrac{R(l_{coarse}-1) - R(l_{coarse}+1)}{2R(l_{coarse}-1) - R(l_{coarse})} & \text{if} \quad R(l_{coarse}-1) > R(l_{coarse}+1) \\ l_{coarse} \quad \text{if } R(l_{coarse}-1) = R(l_{coarse}+1) \\ l_{coarse} - \dfrac{R(l_{coarse}+1) - R(l_{coarse}-1)}{2R(l_{coarse}+1) - R(l_{coarse})} & \text{if} \quad R(l_{coarse}-1) < R(l_{coarse}+1) \end{cases} \tag{5.23}$$

The result of the implementation of this interpolation scheme is shown in Fig.5.11 and Fig.5.12. In the case of the SAD estimator, a clear improvement is observed; the systematic bias obtained is even better than to that observed for SSD and NXC with the parabola interpolation method, and is less than 1% even in the worst case. For the XSign estimator however, the improvement provided by the new interpolation scheme is far less obvious.

5.3.2 Analysis of the statistical performance with a matched filter at the receiver with simulations

In this section, the statistical performance of the four estimators is tested under different SNR conditions, and for four different axial displacements: 0.05 λ, 0.10λ, 0.20 λ, and 0.40 λ, when

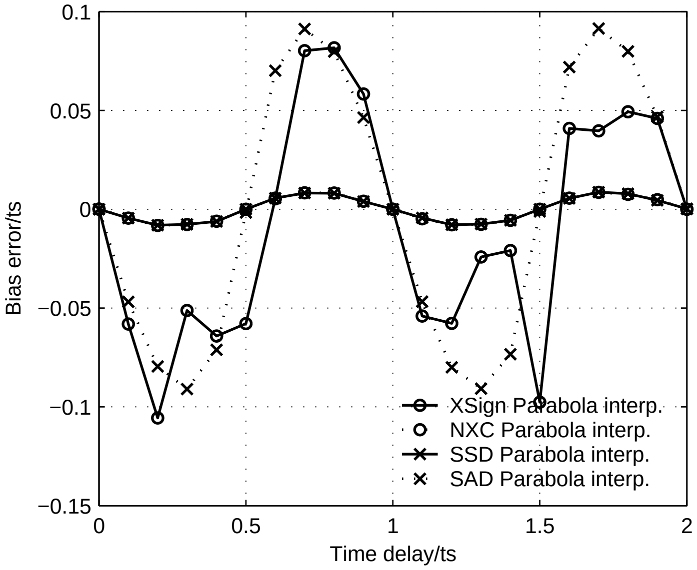

Figure 5.7: Comparison of the bias introduced by parabola interpolation for the four tested estimators. Each point represents the average bias computed with simulations over 1000 independent realisations.

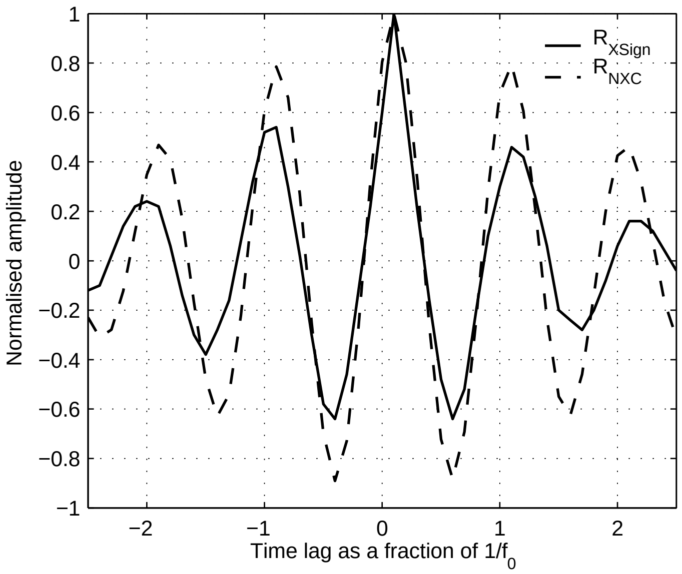

Figure 5.8: Comparison of some typical R_{NXC} and R_{SAD} functions observed for a displacement of 0.10 λ, $T = 2\mu\mathrm{s}$.

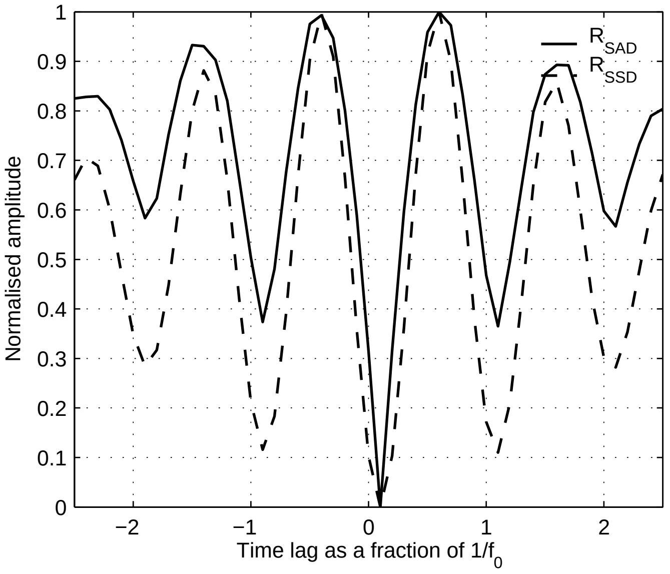

Figure 5.9: Comparison of some typical R_{SAD} and R_{SSD} functions observed for a displacement of 0.10 λ, $T = 2\mu$s.

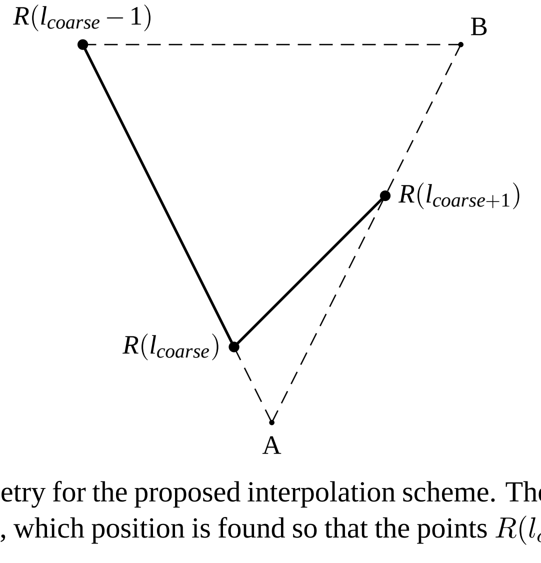

Figure 5.10: Basic geometry for the proposed interpolation scheme. The interpolated minimum of the curve is at point A, which position is found so that the points $R(l_{coarse-1})$, A and B form an isosceles triangle.

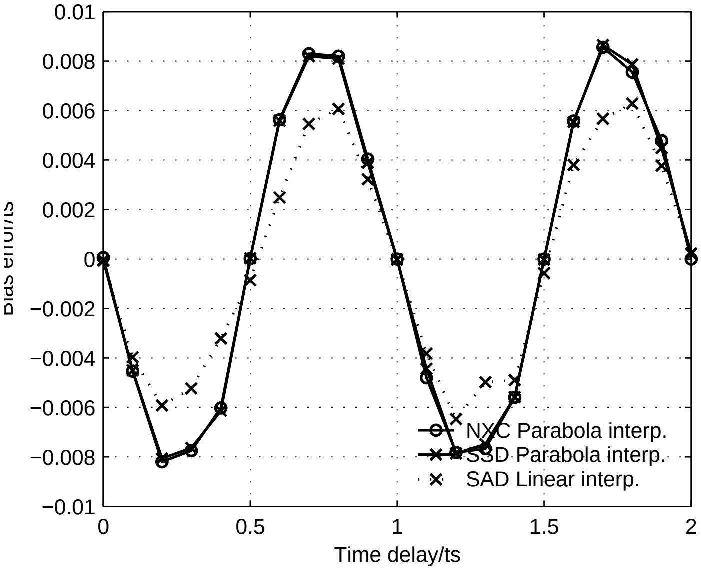

Figure 5.11: Comparison of the bias introduced by parabola interpolation for SSD and NXC and comparison with the proposed scheme for SAD. Each point represents the average bias computed with simulations over 1000 independent realisations.

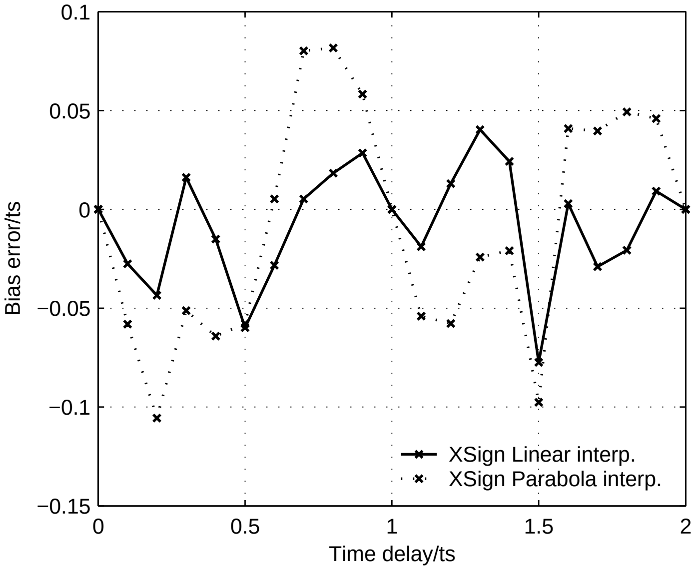

Figure 5.12: Comparison of the bias introduced by parabola interpolation for XSign and comparison with the new interpolation scheme. Each point represents the average bias computed with simulations over 1000 independent realisations.

a matched filter is implemented at the receiver. The set-up of the simulations is similar to section 4.3.2, except that a CF 4 cycles pulse is used as a reference to compute the SNR conditions after the matched filter. Note that similarly to the previous simulations with phase-shift based estimators, all sources of decorrelation between successive received signals are neglected. The estimation is performed using only two simulated received signals. The estimators were implemented according to subsection 5.1.3, into FORTRAN subroutines called by MATLAB to accelerate the computations. The interpolation schemes chosen were the parabola interpolation for the SSD and NXC estimator and the new proposed linear interpolation scheme for the SAD and the XSign estimator. The interval of search of the extrema of the functions were restricted to $[-\frac{1}{2f_0}, +\frac{1}{2f_0}]$, for axial displacements values of 0.10 λ and 0.20 λ and to $[-\frac{1}{f_0}, +\frac{1}{f_0}]$ for an axial displacement of 0.40 λ. Since we are interested in potential gains in resolution as well, the gated range window duration was set to 1 μs, which is a relatively low value, leading to a potential good axial spatial resolution. For the following graphs we use the same definition of relative error as in Chapter 3, i.e. the ratio of the standard deviation of displacement estimates to the actual displacement.

Fig.5.13 reports the results obtained for a small and a medium displacement (0.05 λ and 0.10 λ). The four estimators perform very similarly in terms of relative error and bias, the Xsign performs slightly worse than the three others. These observations are coherent with previous results reported in [94, 92]. For these displacements, the dependence of the performance as the inverse of the displacement to be estimated is clearly visible: doubling the axial displacement from 0.05 λ to 0.10 λ halves the relative error. For low SNR conditions, the relative error is quite important, 50% or more, which shows that crosscorrelation cannot be used to measure such displacements in this range of SNR without averaging the estimates over more pulse transmit/receive cycles. In fact a good statistical performance seems to be obtained only for a medium range of SNR (20 dB). In terms of bias, the estimators are all quite robust (around 10% in the lowest SNR conditions tested), but again, a very low bias (2% and less) is only achievable for 10 dB or less). A comparison with Fig 5.1 shows a qualitative agreement between the CRLB and the relative error in the case of an axial displacement of 0.10 λ. (Note however that the simulations take into account the effect of a transducer, whereas the CRLB was derived for the theoretical case of square spectra, the comparisons are thus only qualitative).

Fig.5.14 reports the results obtained for an axial displacement close to the Nyquist limit (0.20 λ) and a displacement exceeding the Nyquist limit (0.4 λ). The relative errors obtained in poor

SNR conditions are quite high, well above 50% and even higher than for an axial displacement of 0.10 λ. A comparison of the orders of magnitude predicted by the CRLB in Fig.5.1 clearly shows that in this region the CRLB is not achieved. The relative bias is also excessively high in poor SNR conditions compared to the case of smaller axial displacements. These results show that even in ideal conditions (no decorrelation), robust estimation of displacements close to, or superior to the Nyquist limit is not possible while using only two pulse/receive cycles if the conditions are lower than 20 dB. The obtained histograms of the estimates for an SNR of 15 dB are quite instructive. Even in the case of a displacement of 0.20 λ, for which the search interval of the minimum was restricted to the Nyquist interval, we see that in a significant number of cases, the boundaries of the interval are detected (corresponding to axial displacements of +/- 0.25 λ), which considerably deteriorates the performance of the estimator both in terms of relative error and relative bias. In particular it can be seen that for large displacements, the CRLB cannot be reached for SNR conditions lower than 20 dB. For a larger displacement of 0.40 λ, a false peak is detected, at -0.10λ, which is separated from the true peak by λ/2. This is coherent with the theoretical analysis performed.

Arguably, and as pointed by Jensen [107], the relative error bears only little information concerning the performance of the estimators in these latest cases, because false peaks introduce large errors. Following Jensen's approach in [107], we may define a correct detection probability, as the probability that the estimated value falls between plus or minus 0.05 λ around the true value. Fig 5.17 reports the measured probability over 1000 realisations with simulations for the NXC estimators, an axial displacement of 0.40 λ, and varying the gated range window length. Clearly, the probability of correct detection varies with the gated range window duration. For the shortest window duration tested, the probability of correct detection becomes maximal only for SNR values superior to 20 dB. Finally, it is interesting to notice that for these relative large axial displacements, the Xsign estimator offers lower performance than the three other estimators, which doesn't seem to have been previously reported in other studies. It suggests that in spite of its simplicity, this estimator may not be used to measure displacement or velocities larger than the Nyquist limit, at least in poor to moderate SNR conditions SNR and with the short time duration window tested (1 μs). The SAD, SSD and NXC estimators all compare similarly. Since SAD is the estimator with the potential lowest hardware cost (no multiplications involved), this is the estimator chosen for comparison with coded excitation in the next subsection.

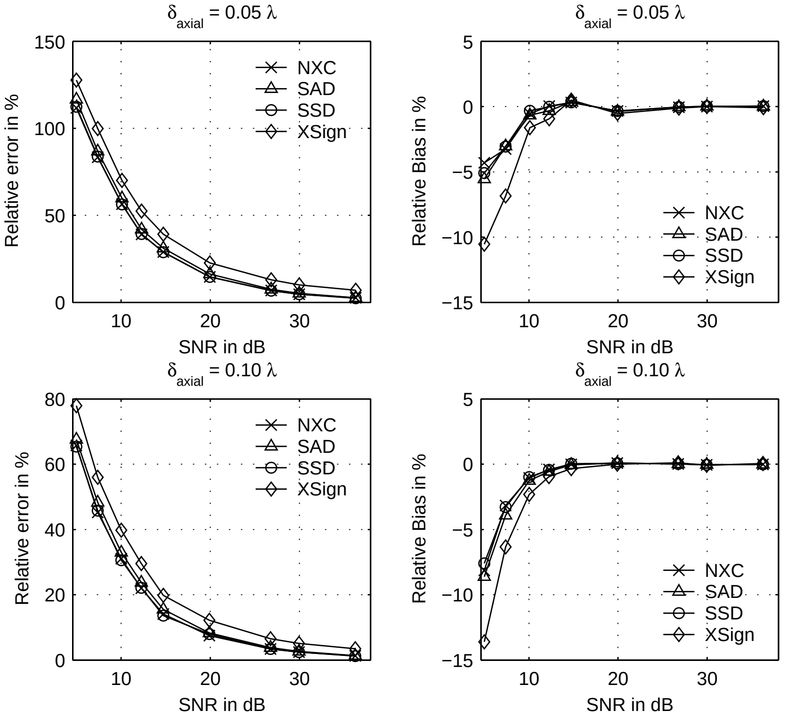

Figure 5.13: Up: Comparison of the relative error against the SNR conditions obtained by simulations for the four different estimators for an axial displacement of 0.05 λ, $T = 1$ μs. Down: same with an axial displacement of 0.10 λ.

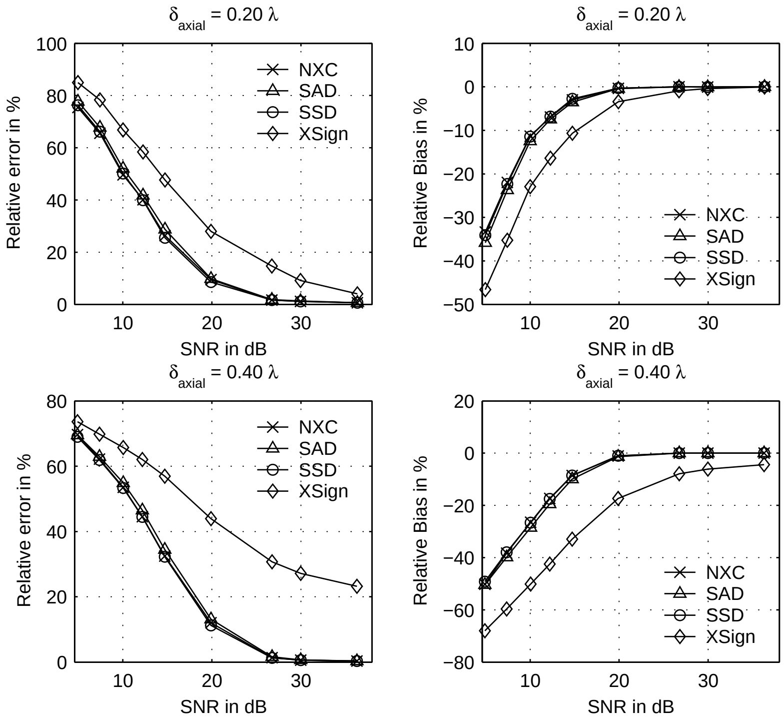

Figure 5.14: Up: Comparison of the relative error and bias against the SNR conditions obtained by simulations for the four different estimators and for an axial displacement of 0.20 λ, $T = 1$ μs. Down: same with an axial displacement of 0.40 λ.

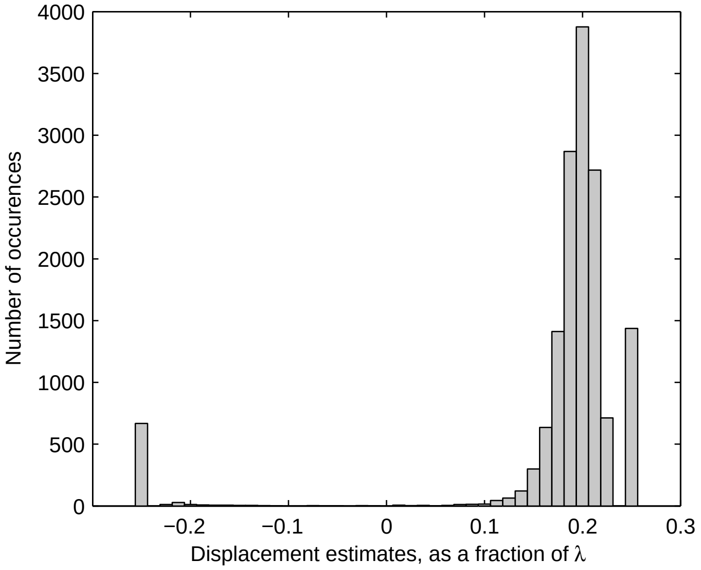

Figure 5.15: Histogram of the estimates obtained for an axial displacement of 0.20 λ and SNR conditions of 15 dB, the interval of search of the correlation peak was limited to [-0.25 λ, +0.25 λ].

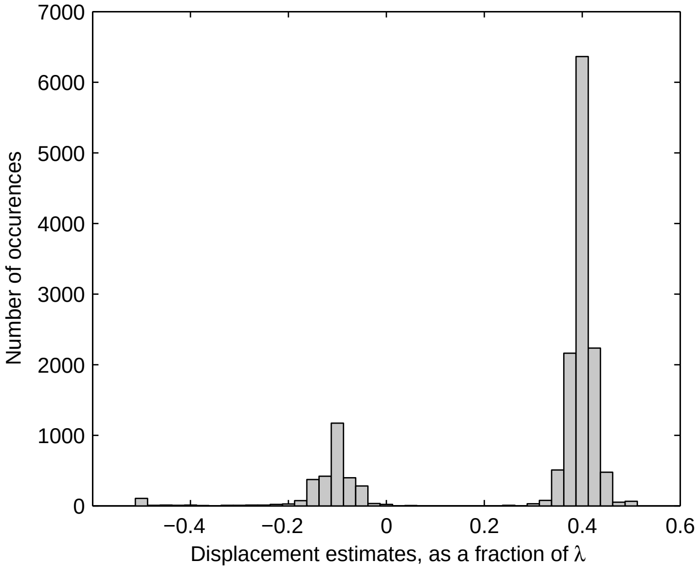

Figure 5.16: Histogram of the estimates obtained for an axial displacement of 0.40 λ and SNR conditions of 15 dB, the interval of search of the correlation peak was limited to [-0.5 λ, +0.5 λ]. A false peak is clearly detected corresponding to a shift of 0.5 λ from the true peak.

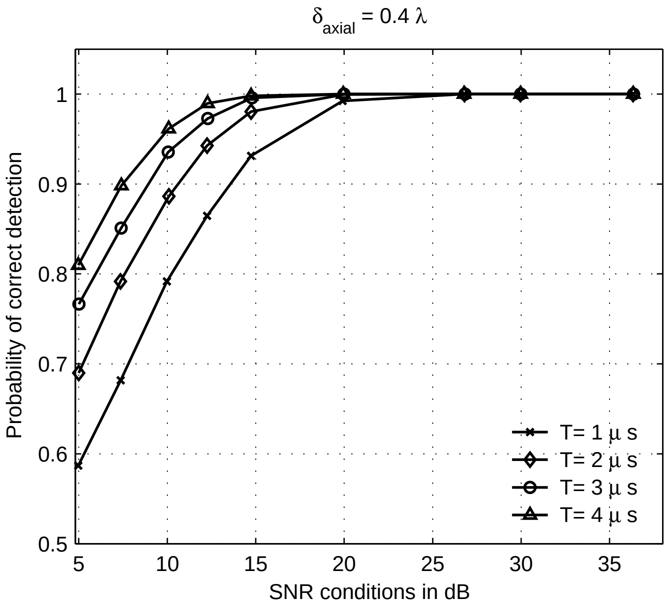

Figure 5.17: Probability of correct detection of the peak of the normalised crosscorrelation versus SNR conditions for an axial displacement of 0.4 λ.

5.3.3 Improvement of the performance with coded excitation

This subsection presents the results of the simulations obtained to assess the potential benefits of using coded excitation with time-shift based estimators. As previously mentioned the SAD was used, because it offers a very similar performance to NXC, for a potentially lower implementation cost. The same CF 4 cycles pulse was used as a reference, two LFM chirp waveforms were used with a duration of 10 μs and respective fractional bandwidth (B_f = 0.5 and B_f = 0.1). The results obtained for axial displacements of 0.05 λ and 0.10 λ are reported in Fig.5.18. A significant gain in performance is obtained for low SNR up to 20 dB. In terms of bias, the results obtained with the chirps are excellent for all the SNR conditions tested (relative bias inferior to 1%) in all cases. A slight difference in performance is observed between the two chirps, the chirp with the fractional bandwidth B_f = 0.5 performs slightly better than the chirp B_f = 1.0, which suggests that the performance is driven by the SNR in these conditions and thus, the coded waveform achieving the highest gain in SNR yields the best performance (4.41 dB versus 8.91 dB, for respectively B_f = 0.5 and B_f = 1.0, according to table 5.1) . The results obtained for axial displacements of 0.20 λ and 0.40 λ are reported in Fig.5.19. The gains in performance obtained in these cases are very significant over the low range of SNR and some improvement is achieved up to 25 dB. This confirms that in this case, the use of coded excitation can make the performance of the estimator switch from a large, “false peak” error regime, to a small error “jitter” regime. This can be interpreted in the light of the theoretical analysis by the fact that the chirp waveforms achieve the $TBSNR'$ product necessary to operate in the jitter regime of errors. It can be noticed that in this case the chirp B_f = 1.0 performs slightly better than the chirp B_f = 0.5. This analysis is further confirmed if we adopt the same approach as in the preceding subsection and plot the probability of correct detection for the three different waveforms in Fig. 5.20.

5.4 Discussion and conclusion

This chapter has presented an up-to-date review of the use of time-shift based estimators in the context of medical ultrasound applications and their statistical performance. From a theoretical point of view, an interesting aspect is that the performance of these estimators can achieve the CRLB for time delay estimation. The CRLB however only describes the performance of these estimators for relatively high values of SNR, when the errors observed are relatively small and correspond to small deviation in the location of the correlation peak around its true

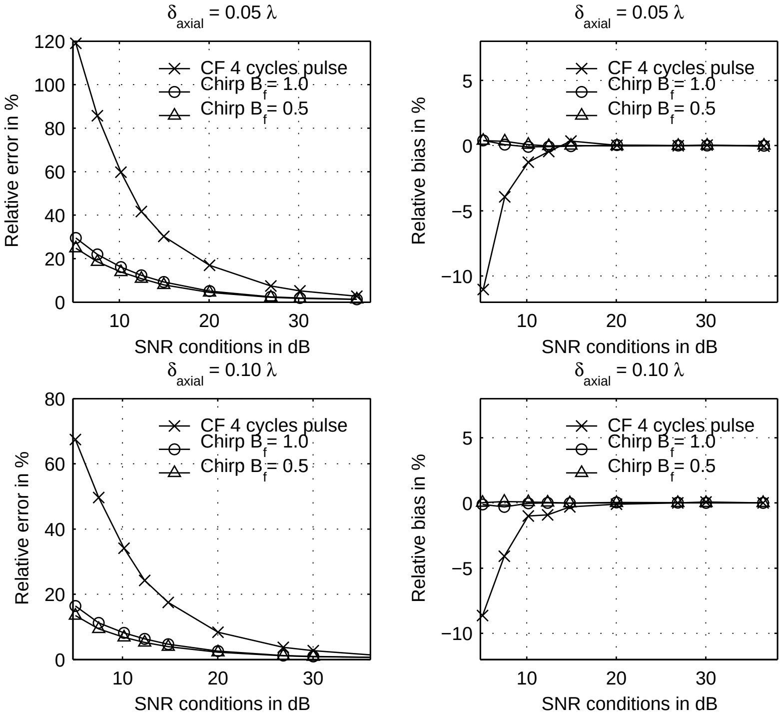

Figure 5.18: Up: Comparison of the relative error and bias obtained by simulations for a CF 4 cycles against the SNR conditions, and two LFM Chirps of duration $T_p = 10$ μs, and respective fractional bandwidths $B_f = 0.5$ and $B_f = 1.0$ with the SAD estimators for an axial displacement of 0.05 λ, $T = 1$ μs. Down: same for an axial displacement of 0.10 λ.

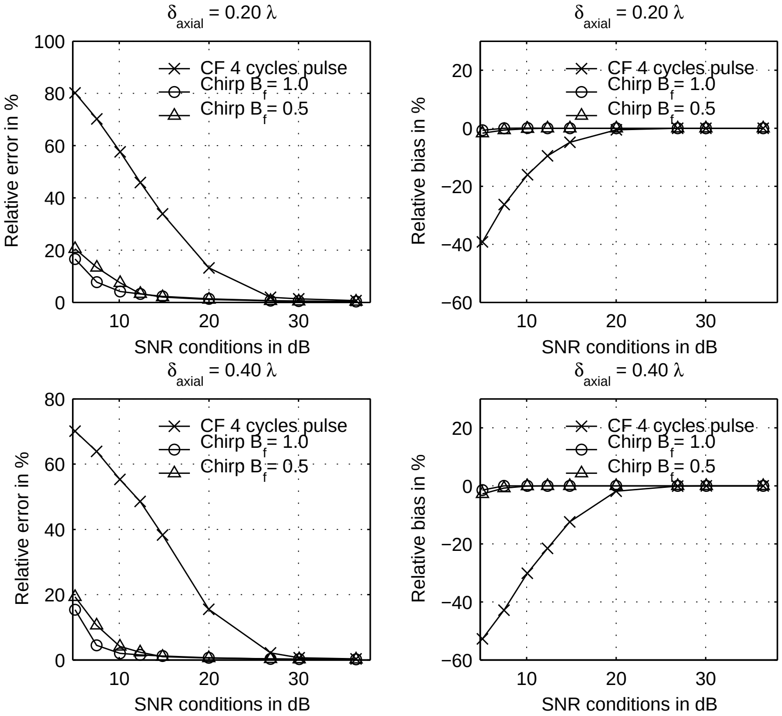

Figure 5.19: Up: Comparison of the relative error and bias obtained by simulations for a CF 4 cycles against the SNR conditions, and two LFM Chirps of duration $T_p = 10$ μs, and respective fractional bandwidths $B_f = 0.5$ and $B_f = 1.0$ with the SAD estimators for an axial displacement of 0.20 λ, $T = 1$ μs. Down: same for an axial displacement of 0.40 λ.

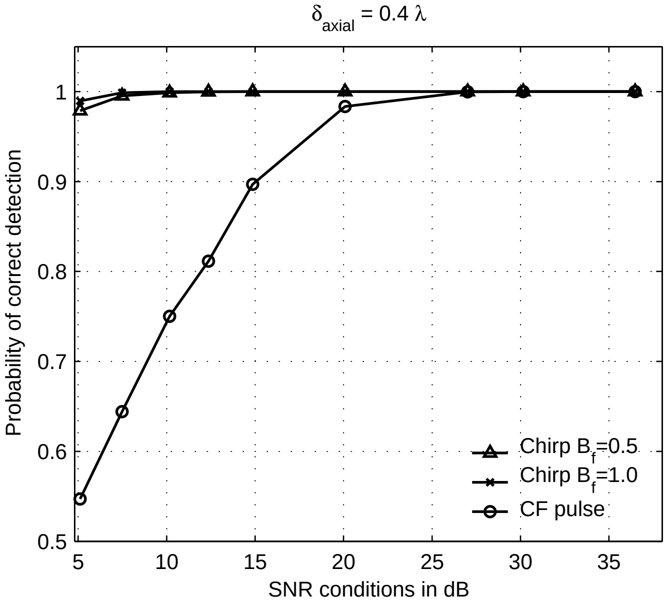

Figure 5.20: Probability of correct detection of the peak of the normalised crosscorrelation versus SNR conditions for an axial displacement of 0.4 λ, comparison between a CF pulse 4 cycles, a chirp $B_f = 0.5$ and a chirp $B_f = 1.0$, $T = 0.5$ μs

value. In many cases the crosscorrelation can operate in a much larger error regime, which is due to false peak detection. This regime of error is to be avoided in most applications, because it implies the use of non-linear filtering to remove the false peaks, which potentially also reduces the spatial information provided by the estimates. In particular, it was shown that the estimation of large displacements (large velocities) above the Nyquist limit in moderate SNR conditions can be quite difficult. Another potentially important deviation from the CRLB regime of performance in practise is the physical decorrelation of signals. It is not clear if the relatively simple model of decorrelation introduced by Walker et al. [96] fully describes the dependence of the statistical performance on the physical decorrelation of signals found in practice. On a theoretical ground, it was shown that coded excitation could be useful even in the CRLB performance regime for SNR values lower than 15-20 dB. The margin of improvement in terms of relative error appears to be higher for smaller displacements. Even when some relatively high conditions in SNR are reached, it was also shown that a gain in bandwidth through the use of wideband coded waveform could be beneficial in terms of performance (not to mention the gain in spatial resolution itself). For applications benefiting from a moderate to large SNR (that is most of applications in normal conditions apart from blood flow estimation), it is not clear how much coded excitation would be useful, because the CRLB then shows that decorrelation is the parameter driving the performance ultimately. Finally, we suggested that coded excitation could enable to switch from a large error regime (false peak detection) to a small error regime, even for low SNR conditions, and for large displacements (beyond the Nyquist limit).

A simulation set-up very similar to that used in the previous chapter was used to study all these aspects numerically. A first study focused on the systematic error (bias) introduced by the extremum interpolation step, for four different time-shift based estimators(NXC, XSign, SAD, SSD). It was shown that the bias exhibits a periodical behaviour with the axial displacement for the SAD, SSD and NXC estimators. The XSign estimator had an erratic behaviour in our simulations. It was also shown that the parabola interpolation scheme was not adequate for the SAD estimator, with an observed relative bias one order of magnitude higher than for the SSD and NXC estimators. The reason for this is that the SAD function exhibits a sharp singularity at its minimum that cannot be interpolated by a smooth curve like a parabola. A new interpolation scheme based on a simple linear interpolation showed much improved results with the SAD, with a relative bias reduced down to less than 1% and comparable to the relative bias observed with SAD and NXC with a parabola interpolation scheme. The statistical performance of all these estimators was tested for different range of axial displacements and SNR conditions. It was clearly shown that the CRLB regime of errors could not be achieved for displacements close to or superior to the Nyquist limit (0.20 λ and 0.40 λ, respectively) for SNR conditions worse than 20 dB, even when the interval of the extremum search was restricted to plus or minus half a period at the centre frequency. In general, these simulations showed that even in ideal conditions (no decorrelation between signals) a robust estimation (less than 10 % relative error) with only two pulse transmit/receive cycles can only be performed for moderate SNR (20 dB and higher). In some applications, more than two signals can be acquired for averaging the estimates (depending on the PRF, and the computational cost of the estimation), in some others, like elastography, only two signals are usually available (a pre-compression and post-compression signal). It was also noticed that the XSign could only be used for very small displacements and that the performance of this estimator deteriorates significantly compared to the NXC estimator when large displacements are to be measured.

Finally, due its relative simplicity, the SAD estimator was used to compare the statistical performance when using coded excitation and conventional CF pulses. LFM chirps were used as a particular example of coded excitation. For small to moderate displacements (compared to the Nyquist limit), the performance was observed to be improved significantly for SNR values lower than 20 dB, which is what was predicted theoretically with the CRLB bound. For larger displacements, the improvement in performance was very significant, which can be explained by the fact the gain in SNR and the high bandwidth provided by coded excitation allows to operate in a small error regime, even in poor SNR conditions (and up to 25 dB) and confirms the points made in the theoretical section. In terms of application, this means that coded excitation could bring a decisive advantage to CFI systems, enabling robust velocity estimation with only a few pulses, and enabling work with velocities that are higher than the Nyquist limit (which means the possibility to work at higher PRF, or at higher range, when the PRF is limited and aliasing becomes a problem). This could also be interesting for strain estimation applications, for which the displacements to be measured are quite large. In fact, a study by Liu [113] has already confirmed with some simulations and experiments the potential of coded excitation for this type of applications.

Chapter 6
Experimental study

The aim of this chapter is to provide a complementary experimental study to the work of previous chapters. The first basic aspect is to demonstrate the feasibility of velocity estimation using coded excitation with phase shift and time shift based estimation schemes in real conditions, with effects such as non-linear propagation, frequency dependent attenuation, and physical decorrelation of signals. A second aspect of this study is to determine whether the use of coded excitation translates into improved performance of velocity estimators, in agreement with the results of previous chapters. The first section presents the experimental setup for this study along with considerations in the design of a rotating phantom. The second section presents the experimental protocol and some specific considerations taken relating to trigger jitter. Finally, the third section presents the experimental results obtained. The conclusion and discussion section sums up the points made and puts these results into perspective.

6.1 Design of a rotating phantom

6.1.1 Choice of a phantom

Phantoms are test objects primarily used to check diagnostic ultrasound equipments performance. From a research perspective, phantom studies are also an interesting intermediate step to validate a new approach or method in a controlled environment before entering a clinical phase study. Materials with controlled acoustical and mechanical properties have successfully been developed over the years to mimic human tissue or blood. Flow phantoms with realistic physiological parameters have been demonstrated for the study of stenoses in arteries, a good review can be found in [114] for example. For some other clinical applications, like echocardiography, the complexity of tissues and movements of the heart however make the fabrication of a realistic phantom particularly challenging. Simpler test objects can however be designed to check some specific aspects of the performance of a new approach in a controlled environment. As stated in the introduction chapter (Chapter 1, displacement and velocity estimation

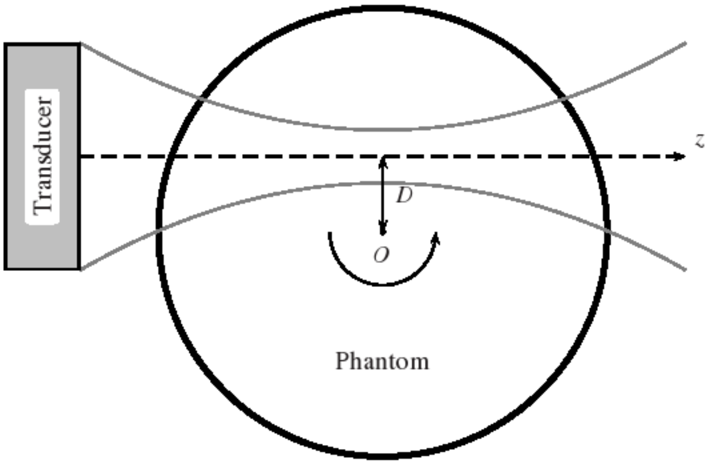

Figure 6.1: Basic geometry of the rotating phantom. O is the centre of rotation, the z axis is the axis of the transducer which is at an offset D from O, and the grey curves represent a very schematic representation of the focused ultrasonic beam.

techniques in medical ultrasound can be used in a wide range of techniques and clinical applications, with some very different physical media probed (viscous liquid in the case of blood /viscoelastic solid in the case of soft tissues), and very different SNR conditions. With the general scope of this study, the choice of the phantom was mainly driven by criteria of ease of implementation with simple and highly controllable movements of the backscattering material. The rotating phantom was chosen for this study, this is a test object that was originally designed to test the performance of scanners for Doppler Tissue Imaging applications [115][116]. It was also used in a recent study published by our lab [117] . The next section presents its geometry and properties.

6.1.2 Basic geometry and approximations

The phantom consists of a cylinder of backscattering material rotating around its axis. The basic geometry is reported in Fig.6.1, showing the positioning of the transducer, with an offset D from the centre of rotation 0, and a simplified representation of the spreading of the focused acoustic beam.

Fig.6.2 examines in more details the displacements of scatterers between two firings. The angle the phantom has rotated between two firings (during a pulse repetition period) is denoted as ϕ.

A scatterer initially on the axis of the transducer at position M has moved to the real position M'. In fact, if ϕ is very small, the trajectory of the scatterer can be well approximated by prolonging the tangent of the circular trajectory until point M''. (Obviously in the figure, the angles were exaggerated so the approximation does not appear to hold well). The amplitude of the approximated rectilinear displacement is then:

$$||\overrightarrow{MM''}|| = ||\overrightarrow{OM}|| \sin \phi \tag{6.1}$$

which can be simplified, using the approximation that for small ϕ, $\sin \phi \approx \phi$:

$$||\overrightarrow{MM''}|| \approx ||\overrightarrow{OM}|| \phi \tag{6.2}$$

The figure also shows the axial component of the displacement vector which is the quantity estimated with ultrasound:

$$\delta_{axial} = ||\overrightarrow{\delta}_{axial}|| = ||\overrightarrow{MM''}|| \cos(\theta) \approx ||\overrightarrow{OM}|| \phi \cos \theta. \tag{6.3}$$

Some elementary geometry shows that:

$$\cos \theta = \frac{D}{||\overrightarrow{OM}||}. \tag{6.4}$$

and thus:

$$\delta_{axial} \approx D\phi, \tag{6.5}$$

which proves the remarkable property that the axial displacement probed is completely independent of the considered position M on the z axis of the transducer (that is, it is independent of the considered depth). The angle θ, made by the approximated linear trajectory with the axis of the transducer, is however dependent on the position of the point M. If z_m measures the position of M with respect to origin O' (projection of O on the z axis), we have:

$$\tan \theta = z_m / D \tag{6.6}$$

Obviously for z_m= 0 (scatterers at point $0'$), $\theta = 0$ and the displacement is purely axial. Eq.6.5 can also be used to obtain some order of magnitudes to make the rectilinear approximation *a posteriori* valid. Since axial displacements are usually a fraction of the wavelength (the maximum non- aliased symmetric interval corresponds to [-0.25λ, +0.25λ]), the comparison

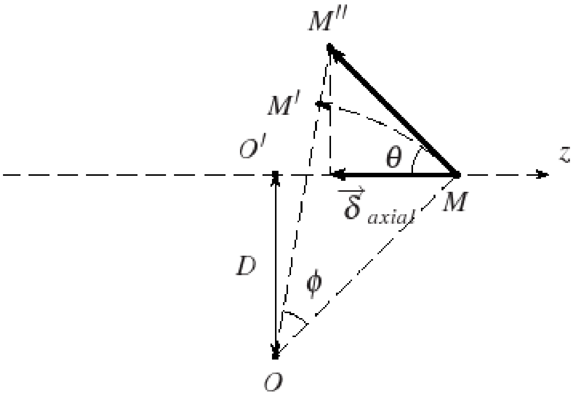

Figure 6.2: Trajectory of scatterers in the rotating phantom. ϕ is the angle the phantom has rotated between two firings. M' corresponds to the real position of scatterers originally at point M after rotation, M" is the approximated position.$\vec{\delta}_{axial}$ is the axial component of the displacements of the scatterers probed by the transducer.

can be made between a wavelength and D, the validity of the approximation depends on:

$$\frac{\lambda}{D} \ll 1, \tag{6.7}$$

which implies to set the distance D relatively large compared to the wavelength.

Finally, in practice, the transducer probes the displacement of scatterers present in a sample volume around its axis, which depends on the beam acoustic properties. Fig.6.3 illustrates the velocity (displacement) dispersion probed in a sample volume. The sample volume close to the focus for a circular single element transducer can be approximated by a cylinder with a diameter equal to the beam width BW (equal for instance to the FWHM of the lateral profile of the transducer beam amplitude), and an axial length set by the range gated window and/or the pulse duration used and the axial length of the transmitted pulse. In a 2D representation a section of the sample volume is a rectangle, of width BW. Assuming that the acoustic focus is set close to the point O', it can be seen as depicted in Fig.6.3 that scatterers entering the sample volume represented by the rectangle on the scheme will have different different axial displacements between two firings, because their trajectory are on different radii. A measure of the dispersion can be computed by the ratio of the difference between the maximum and minimum axial displacement probed in the sample volume to mean displacement. An approximate value of the

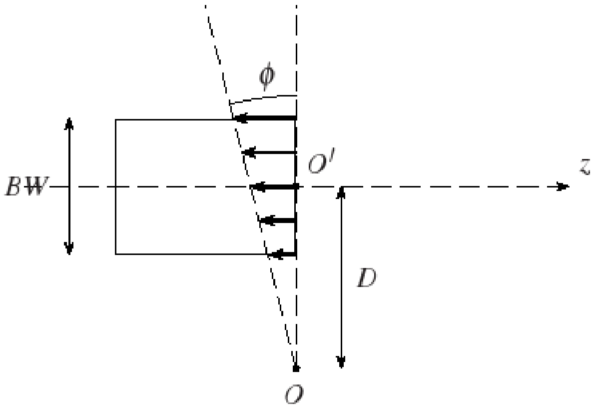

Figure 6.3: Schematic diagram illustrating the displacement dispersion probed in a sample volume. The sample volume is schematically represented as a rectangle, of width BW, the beam width.

displacement dispersion is thus given by:

$$\text{Dispersion} = \frac{((D + BW/2)\phi - (D + BW/2)\phi)}{D\phi} = \frac{BW}{D} \tag{6.8}$$

Since BW is fixed for a given transducer, we see that the distance D controls the dispersion.

6.1.3 Physical implementation

Since modern velocity estimation techniques do not rely on a true Doppler shift but rather on the shift in time or in phase that returned signals experience over several pulses transmits, two solutions can *a priori* be used for a physical implementation of the rotating phantom. One is based on a continuously rotating phantom, the other is based on a stepping phantom, that is, the backscattering material is stationary during each pulse transmit/receive. For this study, the second option was chosen for two main reasons:

- Data acquisition: in a continuous rotating phantom, the system requires relatively fast data transfer at a rate determined by the PRF (possibly up to 10 kHz), as a consequence, the amount of data that can be collected is limited by the memory capacity of the data capture card. On the contrary, in a stepping version of the phantom, the time constraint on data capture is relaxed, since the phantom can remain stationary for as long as necessary to collect and transfer data.

Ingredient	% Mass
Demi-water	82.40
Glycerol	11.32
Benzalkonium Chloride	0.92
SiC powder (400 grain)	0.53
Al_2O_3 (0.3 micron diameter)	0.88
Agar	3.00

Table 6.1: Massic composition of the TMM material used [1].

- Steady rotation. Previous work in our lab has shown that a steady continuous rotation is quite hard to obtain for the relatively low angular speed required, and accurate measurement needs a fine calibration of the angular speed with an optical encoder.

The backscattering material was made using a standard tissue mimicking material recipe [1], based on agar, with SiC and $\mathrm{Al_2O_3}$ scattering particles. The recipe is reported in Table 6.1. In our particular case, the glycerol was omitted, since it is used to obtain a speed of sound close to human soft tissue characteristics ($c \approx$ 1540 m.s^{-1}), and this was not necessary in our study. The diameter for the cylinder was chosen to be 43 mm. The stepping motor is a standard 7.5 degrees stepping motor (48 steps/revolution) coupled with a gear box of ratio (1:125) (from McLennan Servo Supplies, UK), yielding an angle step of $\phi = 2\pi/6000$ rad that is, 0.06 degree. The backscattering cylinder was mounted on the shaft of the gear box and a circuit board SAMOTRONIC101 from Saia-Burgess was used to drive the rotating phantom. Fig.6.4 shows a picture of the experimental set-up.

6.2 Acquisition of signals

6.2.1 Triggering and jitter issues

In the context of a lab experiment with a custom acquisition system, specific attention has to be paid to trigger jitter. In contrast to an integrated scanner in which a single clock is distributed to the different elements of the acquisition chain, the data capture card and Arbitrary Waveform Generator (AWG) used for the experiments have their own internal clocks. Because these two different internal clocks are not synchronised, and have a random phase relationship, a jitter (random error) can be introduced in the delay between the instant of firing and the start of sampling of received signals, which can be detrimental for the performance of velocity estimation,

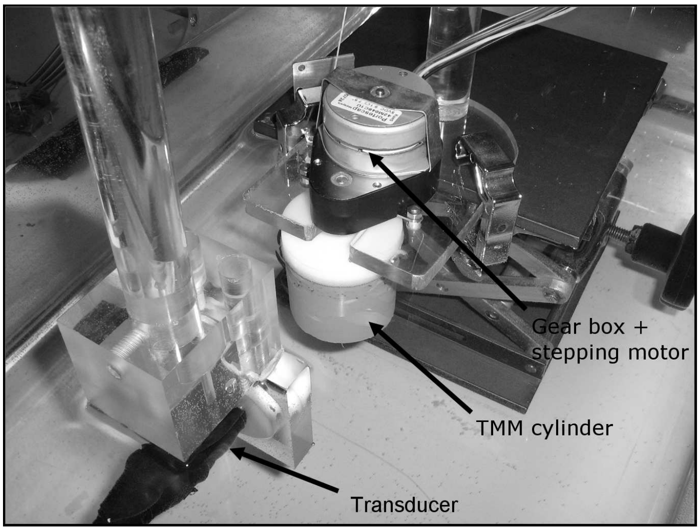

Figure 6.4: Picture showing the transducer mounted on a rod attached to an X-Y test rig system, with the TMM cylinder mounted on the shaft of the stepping motor - gear box ensemble.

especially for low velocities (small displacements). Suppose for instance that the time delay between signals due to motion to be estimated corresponds to 20% of the Nyquist velocity (at 5 MHz, this leads to 20 ns time delay), a trigger jitter error of only 2 ns thus introduces a relative error of 10% in the estimation process (2 ns corresponds to a jitter of one sample at 50 MHz sampling rate). The acquisition-setup was already presented in Chapter 2 (See Fig.2.1). It was found that a software triggering solution for the system offered a simple and accurate solution, suitable for the stepping phantom (since there is no hard time constraint between two pulse transmits, a software trigger can be used). A command is sent to the capture card to trigger an acquisition. The capture card issues a trigger signal which is applied to a first AWG, generating the pulse for transmit. In this experiment, it is also issued to a second AWG, to generate the clock signal necessary to drive the stepper motor with a small delay to allow for complete signals capture before the rotation occurs. The software enters a waiting loop of predetermined duration, to allow for the rotation of the phantom, and the whole operation is repeated. The jitter performance of the system was tested by recording an echo at a fixed depth generated by an analog delay line (Ultrasonic echo generator NR 4110, from Nuclear Enterprise). The jitter was measured as the standard deviation of the random time delays between 1000 successive echo acquisitions. Fig.6.5 shows the obtained histogram of the estimated time delays by cross-correlation technique. The obtained jitter is approximately 0.5 ns, which minimises the impact on the relative error down to 2.5 % in our example case, which is an acceptable value.

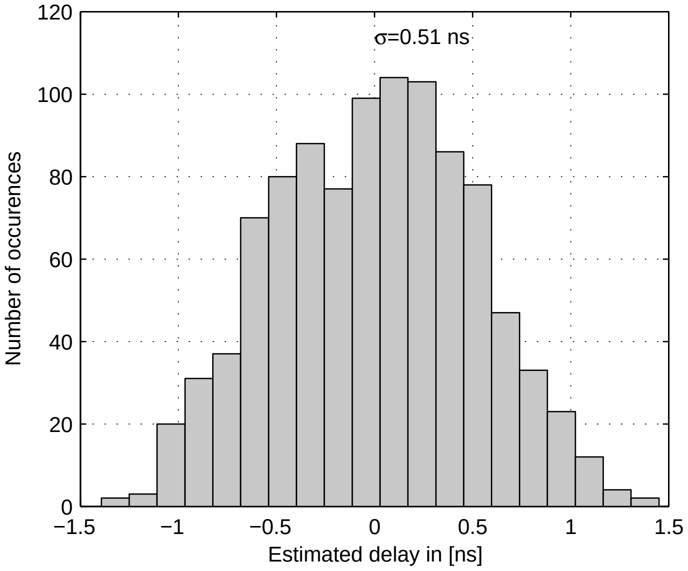

Figure 6.5: Histogram of the random time delays between pulse transmit and data acquisition measured with echoes from an analog delay line. The system exhibits a good performance with a jitter (standard deviation of delays) of 0.5 ns.

6.2.2 Positioning of the phantom relatively to the beam

The backscattering cylinder was positioned and immersed in the tank full of degassed water. The transducer described in Chapter 2 ($f_0 =$ 5.6 MHz, focal depth 50 mm) was attached to the X-Y rig system and first positioned with its axis aligned to the centre line of the phantom, this was done by maximising the amplitude of the echo from the front face of the TMM cylinder. The transducer was then positioned to set the focus approximately at the centre of the phantom. Fig.6.6 shows the signal acquired in this position. The strong echo from the front face is clearly visible, as well as the echo from the back of the phantom. The effect of attenuation on the speckle signal can also be seen. The speed of sound in the phantom can be calculated from this position. The echoes from the front and back face occur at respective times $t_1 =$ 40 μs and $t_2 =$ 98 μs which corresponds to a distance Δd equal to the diameter of the phantom:

$$c_{phantom} = \frac{2\Delta d}{(t_2 - t_1)} \approx\ 1482\,\mathrm{m.s}^{-1} \tag{6.9}$$

Clearly the speed of sound in the phantom can be considered as equal to the speed of sound in water, which simplifies the computations for velocity estimation. The transducer was then moved laterally to a position corresponding to $D =$ 15 mm (as represented in Fig.6.1). A signal acquired in this position is shown in Fig.6.7. It can be noted as well that $\lambda/D \approx 0.017$

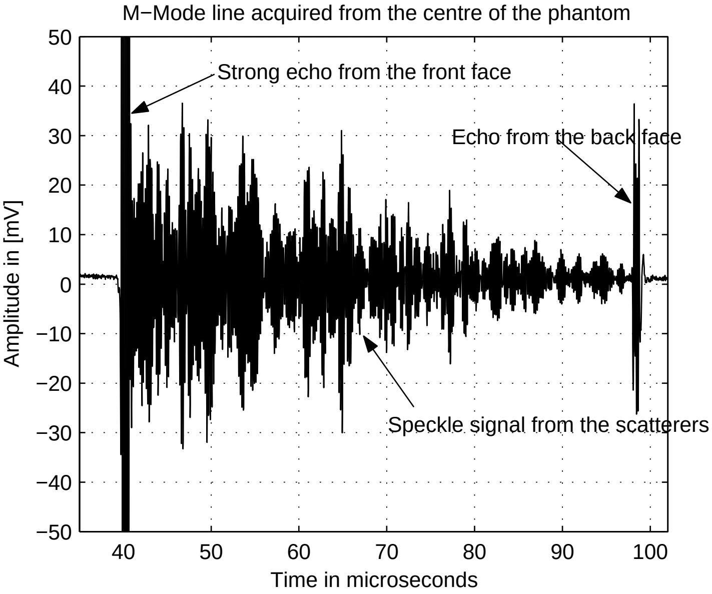

Figure 6.6: Signal acquired from the centre of the phantom, the focus (two way travel time of 69 μs) was set at the centre of rotation. The two echoes from the front face and back face of the phantom are clearly visible.

with the choice made for D, and thus the approximation of Eq.6.7 is amply justified. It is also interesting to have an order of magnitude for the displacement dispersion probed in the sample volume close to focus. Using the result of Chapter 2 concerning the lateral beam width ($BW =$ 1.1 mm), we find:

$$\text{Dispersion} = \frac{BW}{D} \approx 7.3\%, \tag{6.10}$$

which is a small, yet non negligible value in terms of its impact on the statistical performance, according to results presented in [11].

6.2.3 Experimental protocol

All the velocity data were acquired in the preceding position ($D =$ 15 mm), for two different axial displacements, and different excitation pulses. Table 6.2 reports the different number of steps moved by the phantom for each set of data, the angle increments ϕ and the corresponding axial shifts. LFM chirps were chosen as an example of coded excitation in this study. For each waveform tested, 1000 signals were acquired, corresponding to 1000 rotations of the rotating phantom for either 2 steps or 8 steps. The transducer was excited with a voltage of $V_{exc} = 150V$ yielding a MI of approximately 0.3 (see Chapter 2).

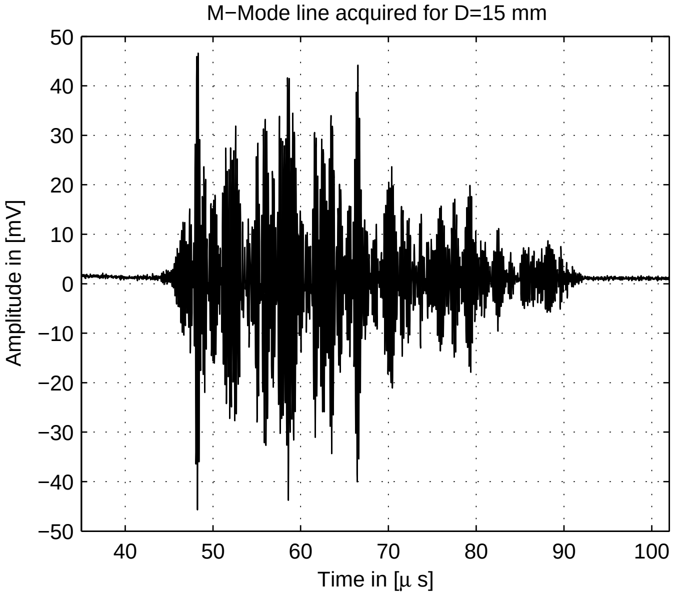

Figure 6.7: Signal acquired from the phantom in position with an offset from the centre $D =$ 15 mm.

# steps	ϕ(degrees)	δ_{axial} (μm)	δ_{axial}/λ
2	0.12	31.4	0.12
8	0.48	125.2	0.48

Table 6.2: Number of steps and the corresponding angle increment and axial displacement of scatterers

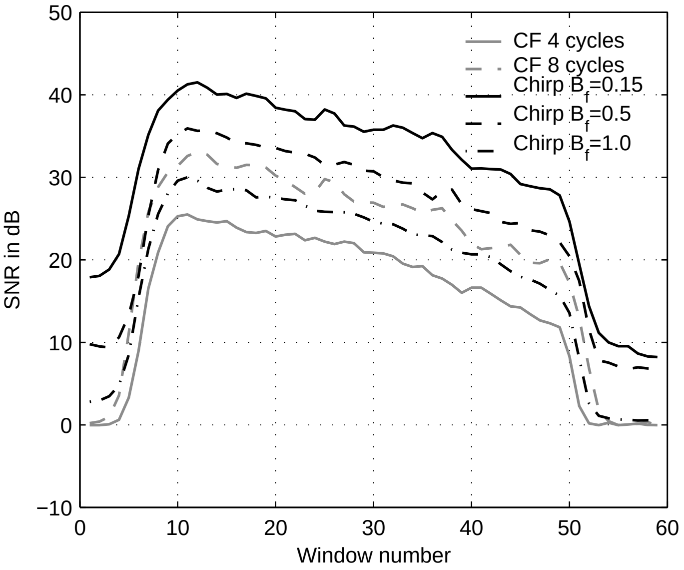

Figure 6.8: Experimental SNR values measured in each gated range window, of duration 1 μs, for different excitation signals.

6.3 Results

6.3.1 SNR gains

For each acquisition with 2 steps rotations, the signals were matched filtered and range gated (duration 1μs), and the power received in the different range gate was averaged over the 1000 acquisitions. Individual SNR values were then computed for each range window using an average noise power of the system after the same matched filter was applied to 1000 noise acquisitions of the system (that is, with the transmit off). The SNR values obtained were then plotted for the different windows. The result is reported in Fig.6.8, with SNR values in dB. Note that average signal power computed in each window is actually the sum of the signal and noise powers during the acquisition, that is if S is the backscattered signal power alone and N the noise power of the system, the $\mathrm{SNR}_{experimental}$ measured experimentally is in fact:

$$\mathrm{SNR}_{experimental} = \frac{S+N}{N} = 1 + \mathrm{SNR} \tag{6.11}$$

However this doesn't differ too much from the theoretical SNR provided SNR $\gg 1$.

Several features can be highlighted from fig.6.8. First, it can be noticed that the SNR conditions decrease steadily (approximately linearly) with depth for range windows corresponding to signals returned from the backscattering material of the phantom (approximately between window number 10 and window number 48). Second, the SNR conditions clearly fall-off down to 0 dB outside of the scattering region of the phantom for the CF pulses. Only noise signals are recorded in these range windows since ultrasound propagates freely in water and no backscattering occurs (Note that in theory the SNR in dB should go toward minus infinity since $S = 0$ in these range windows, however, with the experimentally measured SNR, the ratio measured is $\mathrm{SNR}_{experimental} = \frac{N}{N} = 1$ and logically, a value of 0 dB is found). On the contrary, for LFM chirps, the level of signal measured is non-null close to the phantom wall because of the range sidelobes introduced after the matched filter. The level of these signals is approximately 25 dB lower than the signal received from the TMM. This means that the range sidelobes introduced after compression clearly limit the dynamic range of the useful signals for displacement estimation if no specific attention is taken to reduce their level in the design of the coded waveform. Finally, the gains in SNR achieved by coded excitation over conventional pulses are relatively constant with the increasing range window number (with depth). The gains in SNR were plotted between windows 15 and 45, chosen as representative range windows of the backscattered signal from the inner TMM of the rotating phantom.

The obtained values were reported in the case of the 4 cycles CF pulse as a reference (Fig.6.9) and the 8 cycles CF pulse as a reference (Fig.6.10). The mean values were also reported in these figures as a solid grey line. Table 6.3 also reports these values and compare them with the theoretical values obtained with the simulations in Chapter 3. Although a direct comparison cannot be made, because the centre frequency used is different (respectively 5 MHz for simulations and 5.6 MHz for the experiments), and the spectral properties are different (idealised Gaussian-shaped spectral response with 50 % fractional bandwidth in the case of simulations, 80 % fractional bandwidth for the transducer used in the experiments), the results do not differ much. The relatively high bandwidth of the transducer used for the experiments, and the higher centre frequency only result in a slight improvement in the gains in SNR measured for chirps of fractional bandwidth B_f = 0.15 and B_f = 0.5, compared with simulations. A noticeable aspect however, is that for a relatively wide bandwidth B_f = 1.0 the gains in SNR observed are significantly lower than predicted by simulations. This suggests that frequency dependent attenuation may play a significant role in the sensitivity/ resolution trade-off in practical simulations for wideband coded waveforms. Overall, the results however demonstrate the validity of the theoretical approach taken in Chapter 3 to analyse the resolution / sensitivity trade-off with coded excitation.

	GSNR in dB (ref. 4 cycles)		GSNR in dB (ref. 8 cycles)	
	Experimental	Simulation	Experimental	Simulation
$B_f = 0.15$	15.5	14.5	8.9	8.5
$B_f = 0.5$	9.9	8.9	3.3	2.9
$B_f = 1.0$	4.1	4.4	-2.5	-1.6

Table 6.3: Comparison between experimental values and simulations of the gains in SNR provided by different LFM chirps (duration 10 μs, and different fractional bandwidths B_f) over CF pulses of length 4 cycles and 8 cycles.

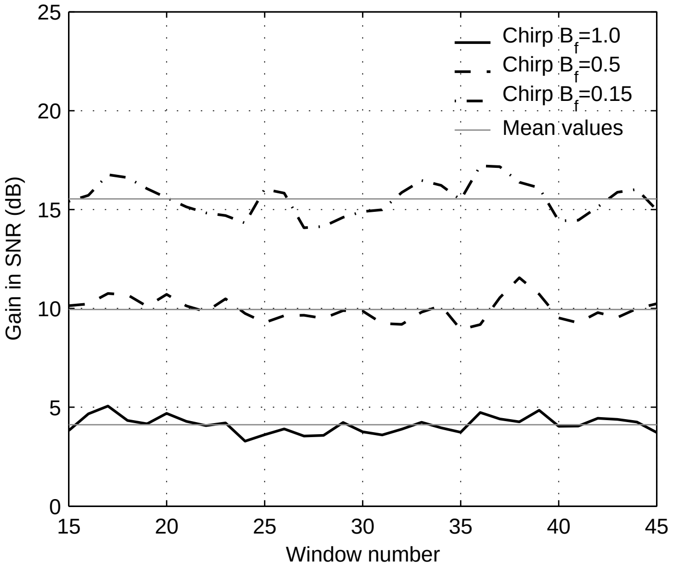

Figure 6.9: Experimental gains in SNR measured with the CF 4 cycles pulse as a reference, the grey solid lines indicate the mean value, for each of the LFM chirp waveforms.

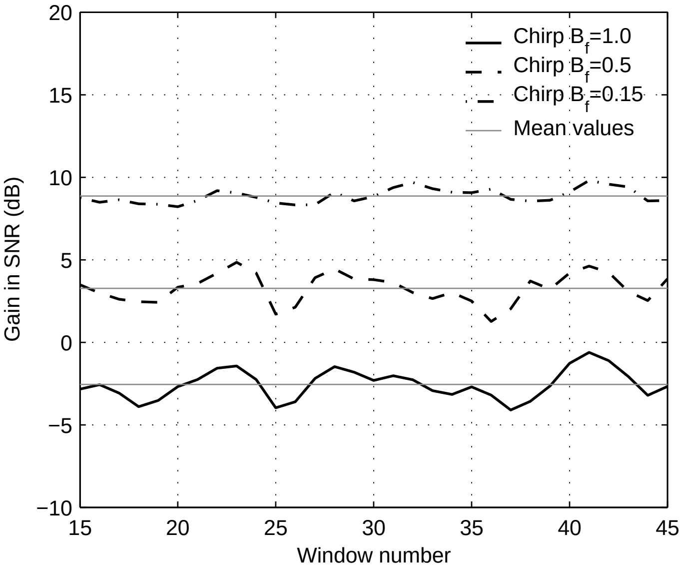

Figure 6.10: Experimental gains in SNR measured with the CF 8 cycles pulse as a reference, the grey solid lines indicate the mean value, for each of the LFM chirp waveforms.

6.3.2 Time shift based estimation

This subsection presents the results of velocity estimation performed on the collected data. After a matched filter, the signals were range gated (range gated window duration of 1 μs) and the SAD algorithm with the linear interpolation scheme described in Chapter 5 was applied. The interval of search was limited to plus or minus 5 lags of at the sampling rate (50 MHz), which corresponds to an interval of search in terms of displacements of [-0.28 λ, +0.28 λ] . An additional threshold was applied so that no velocity estimation is performed when the signals are too weak or nonexistent (in the windows of signals corresponding to depths of return from which no backscattering occurs, the estimation would otherwise be performed on noise signals). The threshold is specified as a dynamic range DR, which is defined here as the ratio between the threshold power level $\sigma^2_{threshold}$ to the max power level measured in a range gated window σ^2_{max}:

$$\mathrm{DR} = 10.\log\left(\frac{\sigma^2_{max}}{\sigma^2_{threshold}}\right) \tag{6.12}$$

Fig.6.11 shows the result obtained. Fig.6.11(a) shows the displacement profile obtained with the 4 cycles CF pulse, each point corresponds to the estimated displacement in a given range window, averaged over 1000 realisations, and the error bar corresponds to plus or minus one standard deviation of the estimates over the same 1000 realisations. Since the SNR conditions were limited to a maximum of 25 dB in the case of the 4 cycles excitation signal (Fig.6.8), the threshold was chosen to be set to obtain a dynamic range of 20 dB. The obtained velocity profile Fig.6.11(a) shows that the standard deviations of the estimates is relatively constant with an increasing range but the estimation process is visibly degraded after window number 40, which coincides with the SNR conditions becoming lower than 15 dB (Fig.6.8). To obtain quantitative figures for comparison, a relative error and relative bias were computed for each range window and averaged over window number 15 to 45 (chosen as representative of the estimation process for signals coming from the interior of the rotating phantom). This yields a relative error of 17 % and relative bias of less than 1 %. These values are reported in Table (6.4). Fig.6.11(b) reports the results for a chirp of fractional bandwidth B_f = 1.0. An overall increased robustness of the estimation process can be observed in the displacement profile, especially for the range windows between 35 and 45. The relative error is constant at around 12 %, which is only a small improvement compared to the 4 cycles CF pulse, but the relative error is more steady, and only starts to degrade after window number 45, which corresponds to SNR conditions at around 15 dB (Fig.6.8). This result illustrates the potential of coded excitation to increase the robustness of estimation at large depths when the SNR conditions deteriorate below 20 dB.

Fig.6.11(c) and 6.11(d) show the same results when rotations of 8 steps were performed. These correspond to relatively large displacements of 0.48 λ, beyond the Nyquist limit (Table 6.2), the interval of search was restricted, in this case, to 10 lags ([-0.50 λ, +0.50 λ]). The profile and statistical performance achieved in the case of the 4 cycles CF pulse shows that a robust estimation can not be performed in this case. This can be explained by the fact the estimator operates in a large error regime with false peak detection. In these conditions, the performance improvement achieved by the LFM chirp B_f = 1.0 is massive, with a steady displacement profile and a relative error of 5.2 %, although this performance visibly slightly degrades after window 45. This is well illustrated by the histogram of the estimated displacements for window number 30 in Fig.6.12 and Fig.6.13. A probability of correct detection was defined as the ratio between the number of estimates lying in the interval [0.43 λ, 0.53 λ] and the total number of estimates. The probability of correct detection is only of 0.77 in the case of the 4 cycles CF pulse and is of 0.96 in the case of the LFM chirp B_f = 1.0.

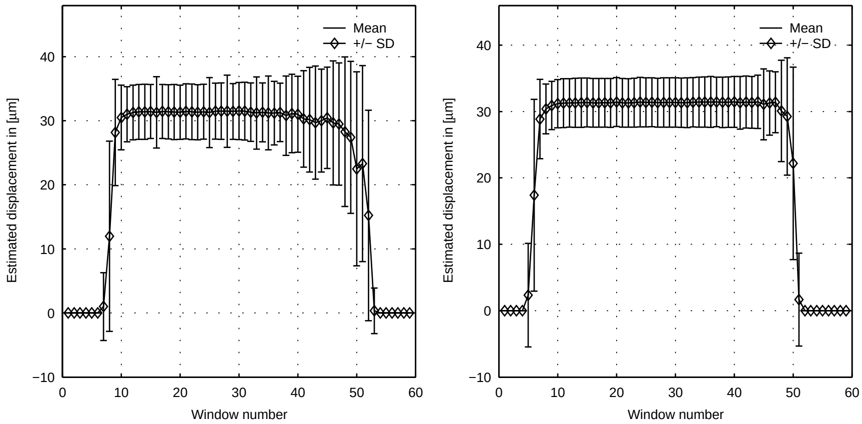

(a) CF 4 cycles, 2 steps

(b) Chirp $B_f = 1.0$, 2 steps

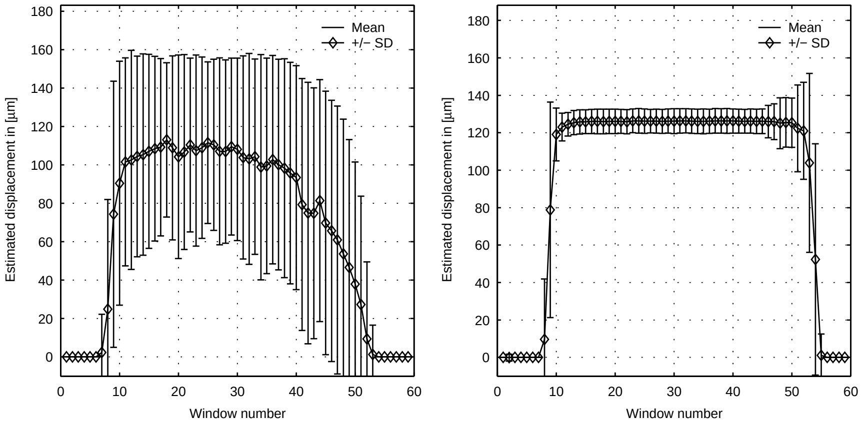

(c) CF 4 cycles, 8 steps

(d) Chirp $B_f = 1.0$, 8 steps

Figure 6.11: Estimated displacement profile with the time-shift based SAD estimator, DR= 20 dB.

	2 steps rotations		8 steps rotations	
	Bias (%)	Error (%)	Bias (%)	Error (%)
4 cycles CF	-0.9	17.0	-20.0	42.1
Chirp $B_f = 1.0$	-0.15	11.9	0.4	5.16

Table 6.4: Performance comparison for time shift based estimation between a 4 cycles CF pulse excitation signals and an LFM chirp $B_f = 1.0$.

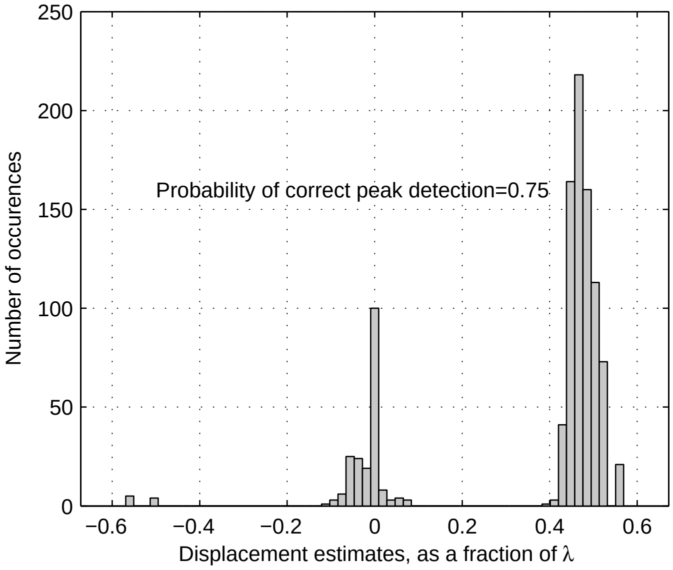

Figure 6.12: Histogram of the experimental displacement estimates obtained for the range window number 30, for a 4 cycles CF excitation pulse, and 8 steps rotations. The probability of correct detection was measured as the ratio between the number of displacements estimates lying in the interval [0.43 λ, 0.53 λ] and the total number of estimates.

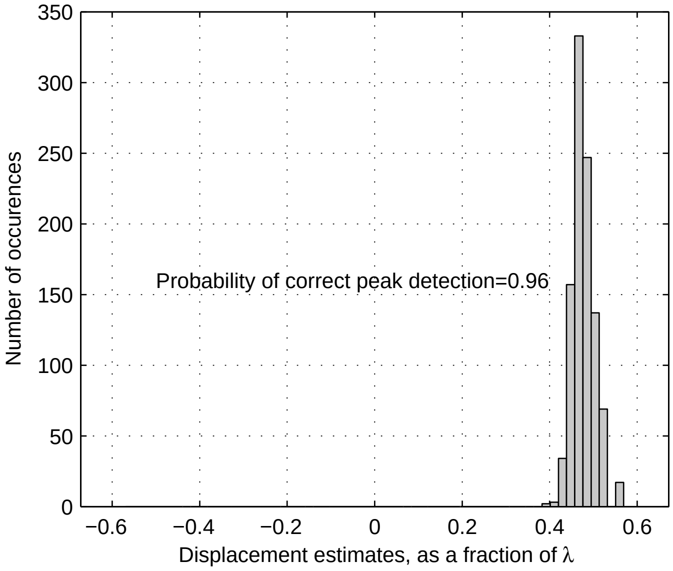

Figure 6.13: Histogram of the experimental displacement estimates obtained for the range window number 30, for an LFM chirp $B_f = 1.0$, and 8 steps rotations. The probability of correct detection was measured as the ratio between the number of displacements estimates lying in the interval [0.43 λ, 0.53 λ] and the total number of estimates.

6.3.3 Phase shift based estimation

This subsection reports the results obtained when phase shift based estimators were applied to the collected data. The same range gated window duration was used (1 μs). Fig. 6.14 reports the displacement profiles obtained. Table 6.5 reports the results in terms of relative error and bias, computed, as in the previous subsection, by averaging the individual relative error and bias from window number 15 to 45. Fig.6.14(a) and 6.14(b) reports the results obtained when applying the 1D autocorrelator respectively for an 8 cycles CF pulse and for an LFM chirp of fractional bandwidth $B_f = 0.5$. The SNR conditions for the 8 cycles CF pulse reach a level 35 dB (Fig.6.8), the DR was thus extended to 26 dB, to set the threshold. The packet size used was $N_p = 4$ transmit/receive cycles. Note, as a consequence, that the statistics in this case are only made using only 250 estimates for each window (since a total of 1000 signals were acquired). A relative performance of 10.3 % is achieved for the CF 8 cycles pulse and slightly degrades for the last windows, the bias is relatively small (1.7 %, on average). The performance achieved with the chirp is more steady across the profile, but yet significantly worse than for the 8 cycles pulse (relative error of approximately 15 %). Interestingly, however, the bias is actually better (-0.25 %, on average). It can be noticed as well that the first displacement estimates in the windows 1 to 5 are non-null, which means that some signal is detected in this region, as a consequence of the presence of the signals introduced by the range sidelobes, and the higher DR (26 dB). These results confirm that in the region of SNR tested, and with a small limited packet size ($N_p = 4$), the performance of estimation with the 1D autocorrelator is not improved with coded excitation, even when using a moderatly wideband coded waveform.

The next figures Fig.6.14(c) and 6.14(d) show the same results when the 2D modified autocorrelation instead of the 1D autocorrelator is applied to the data (the full estimator was applied, including the RF centre frequency estimation part, see Chapter 4). The performance observed is significantly better than with the 1D autocorrelator. A similar trend is observed when comparing the 8 cycles CF pulse and the LFM chirp, except that this time, the performance difference between the CF pulse and the chirp is very small (respectively 7.9 % and 8.4 % for the CF pulse and chirp). Finally, a last set of results is presented in Fig. 6.14(e) and 6.14(f) with the modified autocorrelator and a packet size limited to $N_p = 2$. The performance is logically deteriorated compared to the case $N_p = 4$, but this time, the performance obtained in terms of relative error is better in the case of the LFM chirp (approximately 11 % against 16 % for the CF 8 cycles pulse). Note as well that the relative bias is increased in the case of the chirp (2.3 %).

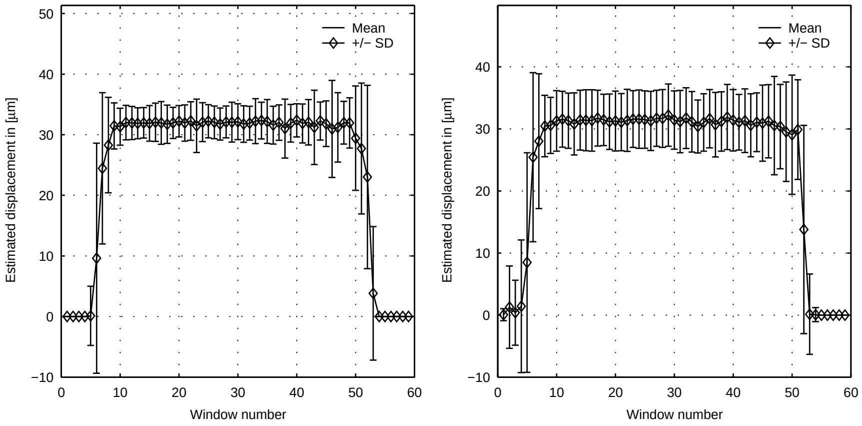

(a) 1D autocorr., CF 8 cycles, $N_p = 4$

(b) 1D autocorr., chirp $B_f = 0.5$, $N_p = 4$

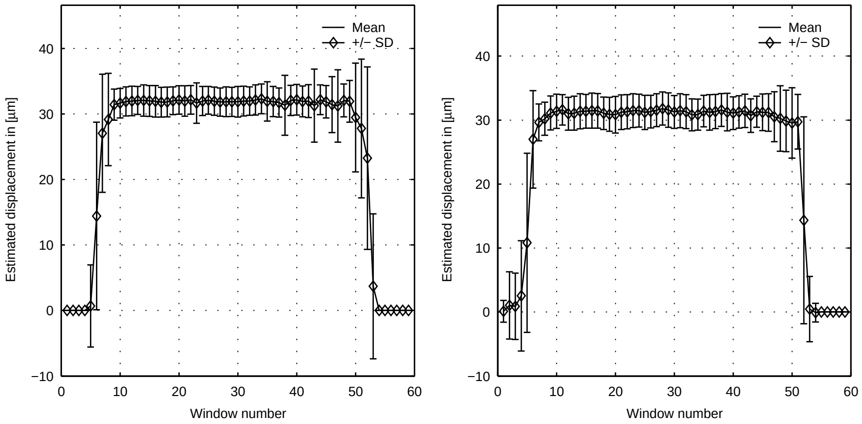

(c) Mod. autocorr., CF 8 cycles, $N_p = 4$

(d) Mod. autocorr., chirp $B_f = 0.5$, $N_p = 4$

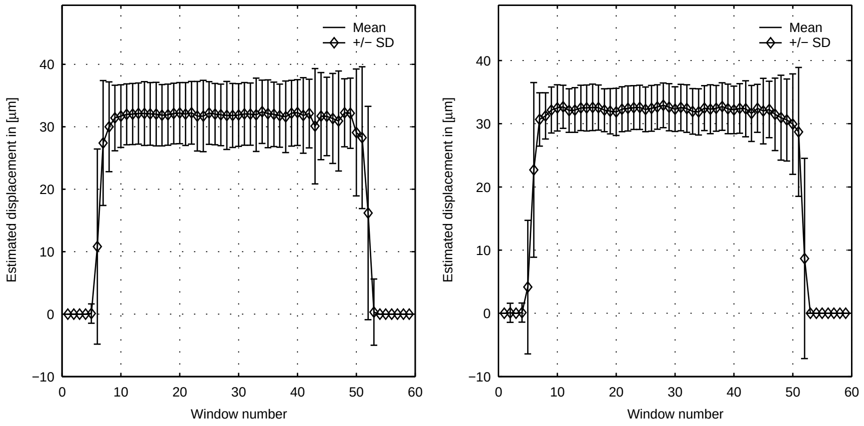

(e) Mod. autocorr., CF 8 cycles, $N_p = 2$

(f) Mod. autocorr., chirp $B_f = 0.5$, $N_p = 2$

Figure 6.14: Estimated displacement profile for 2 steps rotations, with the phase-shift based estimators, DR= 26 dB.

	1D autocorr, $N_p = 4$		Mod. autocorr, $N_p = 4$		Mod. autocorr, $N_p = 2$	
	Bias (%)	Error (%)	Bias (%)	Error (%)	Bias (%)	Error (%)
CF 8 cycles	1.7	10.3	1.6	7.9	1.6	17.3
Chirp $B_f = 0.5$	-0.25	15.3	-0.45	8.4	2.9	11.9

Table 6.5: Average performance comparison for phase shift based estimation between a CF pulse 8 cycles excitation signals and an LFM chirp $B_f = 0.5$.

6.4 Discussion and conclusion

The SNR analysis showed that the experiments were performed in moderate to good SNR conditions (between 10 and 40 dB) depending on the waveform. This experiment has confirmed the simulation results on the general trade-offs in sensitivity and resolution offered by coded excitation waveforms compared to typical CF conventional pulses (4 cycles chosen as a reference for wideband estimation techniques and 8 cycles chosen as a reference for narrowband techniques). Although the parameters used in the experiments and simulations were slightly different, the figures obtained experimentally are in qualitative agreement. The gains obtained experimentally with a high bandwidth transducer (80 % fractional bandwidth) and at a slightly higher centre frequency (5.6 MHz,instead of 5 MHz in the simulations) were observed to be higher than the simulation gains, except for the wideband chirps ($B_f = 1.0$). The significantly smaller values in this latter case suggests that frequency dependant attenuation puts a more severe constraint on the resolution/sensitivity trade-off.

The experimental displacement estimations have proved the feasibility of velocity estimation with coded waveforms, both with narrowband and wideband methods and confirmed some aspects of the statistical performance obtained with coded excitation, compared to conventional pulses. The limitations in terms of dynamic range, if no specific measures are taken to reduce the range sidelobes was also demonstrated. In general, the experiments performed showed that for a medium range of SNR (above 15 dB), the performance is hardly affected by the SNR conditions, a fact that was pointed out in the previous chapters with theoretical and simulations approaches. As a consequence, relatively steady profiles were obtained with range in these experiments. The performance in terms of relative error was however bounded around 10 %, which is significantly higher than the figures obtained with simulations (for SNR above 20 dB, relative errors below 5 % were obtained, even for displacements within the Nyquist range). It is not clear whether decorrelation of signals or the displacement dispersion is the source of this limitation in the perfomance observed experimentally. Further studies could be carried out to assess the relative contribution of these factors to the limitations in performance.

The improvements in performance with coded excitation were relatively modest in the range of SNR tested, for a displacement in the Nyquist range. It should be noticed, however, that improvements in spatial resolution are still possible with coded excitation. Indeed in each of the comparisons made, the coded pulse had a better spatial resolution than the reference CF pulse. Moreover, it was shown that coded excitation had the ability to enhance the performance for long ranges when the SNR conditions drop below 15 dB with wideband strategies. The most striking improvement, as predicted with simulations in the previous chapter, and well confirmed by the experiments, is the ability to perform robust estimation beyond the Nyquist limit with chirps and a relatively small range gate duration (1 μs). For narrowband strategies, the benefits of coded excitation in terms of relative error are limited if the packet size is superior or equal to 4, but a reduction in the relative error is always possible even above 15 dB if the packet size is reduced to 2.

Finally, in terms of practical applications, it is difficult to infer any definitive conclusion from these results for any clinical situations. This was not the intent of the study, as clearly stated in the introduction. Some elements need to be pointed out to put these results in perspective:

- The MI used in this experiment was quite low, and it is likely that with careful electronic design, scanners are able to achieve much better SNR than the relatively high bandwidth custom receiver used in the experiment. On the other hand, the depth of penetration was quite limited (approximately 3 cm) and the centre frequency used (5.6 MHz) is probably at the high-end of the usual range of frequencies used in practice, which maximises attenuation in tissue.
- No specific attention was paid to range sidelobes level in this study. It is not sure what the needs are in terms of dynamic range in practical situations but if sidelobes reduction needs to be achieved, this may well impact the achieved resolution / sensitivity trade-off (Chapter 3).
- The complexity of movements and the possible resulting large decorrelation of signals in real situations probably needs to be taken into account for its impact on the performance, even in relatively high SNR conditions.

Finally, a similar study could have been done with flow phantoms, to check the performance obtained with coded excitation in lower SNR conditions. Particular attention could be paid to the impact of range sidelobes, with clutter rejection filters.

Chapter 7
Conclusion

This chapter presents an organised synthesis of the results obtained in this thesis, and suggests future directions of work. The first section concludes on the potential improvements in sensitivity and resolution offered by coded waveforms for velocity estimation applications. The second section develops the aspects of statistical performance improvement and the choice of velocity estimation strategy with coded excitation. Finally, the last section gives an overview of the possible future directions of work and future applications.

7.1 Improvement in sensitivity and resolution

Coded excitation techniques were introduced in the 50's in the context of radar applications, where the ideal situation of reference consists of an echo signal from a single target, embedded in the white thermal noise of the receiver. This approach was used in Chapter 2 to study experimentally the echoes generated by a wire target, with an single element ultrasonic transducer. Due to the relatively limited bandwidth available with an ultrasonic transducer, the experimental SNR improvements measured after compression by a matched filter were shown to differ from the expected theoretical values by up to 5 dB in the case of very wideband waveforms. This was simply explained by the fact that as the bandwidth of the coded excitation signal is increased, a smaller fraction of the signal energy is transmitted. After compression of the signals using a matched filter, experimental point spread functions were obtained when the wire target was positioned at the focus. Inspection of the results showed that the obtained axial resolutions were in agreement with the bandwidth of the waveforms (the more wideband the waveform, the better the axial resolution). It was observed that the sample volumes hardly differed from the ones obtained with CF conventional pulses after compression. In particular, the obtained lateral resolution was very similar. The essential difference is a perturbation in the axial direction due to the introduction of range sidelobes. The 2D range sidelobes patterns were also also observed to be different for the two types of coded waveforms investigated (LFM chirps and Barker codes).

A single target echo signal is a good model to study the axial resolution of a pulse Doppler system. This model is however not very adapted to discuss the potential improvement in sensitivity with the "multi-target" speckle signals encountered in velocity estimation applications. A model of signal was introduced in Chapter 3 to develop expressions of the SNR conditions adapted to this situation. From these expressions, the potential improvements in sensitivity and resolution offered by coded excitation techniques could be studied. CFI applications were chosen as the application of reference for the discussion. It was shown theoretically that the ability to improve the sensitivity/resolution trade-off relies on the possibility to increase the average transmitted intensity. Specific limitations in terms of intensity limits were also pointed out in the discussion. In velocity estimation applications, the relatively high frequency repetition rate used (up to 10kHz), and potentially the type of waveform used (long narrowband CF pulses in the case of CFI applications) lead to relatively high average (temporal average) transmitted intensity. As a consequence, in many situations of practical relevance, this parameter may be the fundamental limitation in improving the sensitivity. This differs significantly from the case of B-mode imaging applications, for which the peak intensity is the limiting factor (more exactly the rarefation peak pressure, associated with cavitation effects).

In the cases where some headroom for increasing the average transmitted intensity exists, some simulations were performed to assess quantitatively the potential improvements in axial resolution and the SNR conditions. It was shown that an improvement in both sensitivity and axial resolution required an increase of the transmitted intensity by a factor of five (the reference CF pulse was 8 cycles long, chosen as a representative of narrowband pulses used in CFI applications), with coded waveforms of a few microseconds in duration. The gains in SNR in these cases were moderate (2-3 dB at the most), yet the obtained gains in resolution could potentially be interesting in the context of visualising small vessels.

Some further considerations for a practical implementation of coded excitation in a CFI system were mentioned. A brief comparison of LFM chirps and Barker codes as coded excitation candidates was made. Barker codes are easier to implement in terms of hardware, especially for a solution involving baseband decoding, but since the time-bandwidth product of these waveforms is fixed, the sensitivity/resolution trade-off appeared in turn to be less flexible than in the case of chirps. The ultimate sensitivity/resolution trade-off may also depend on factors like frequency-dependent attenuation and possible requirements in terms of sidelobe levels, due for instance to clutter signals. These effects were not taken into account by the simple model adopted in the simulations. In spite of the simplicity of the model used, experimental data obtained in Chapter 6 gave a good support to the analysis performed for the derivation of the SNR conditions. Furthermore, experimental results have clearly presented the limitations in terms of the dynamic range of signals imposed by the range sidelobes level of the compressed waveforms in practice.

Thus, this work has highlighted and demonstrated some essential trade-offs and considerations to be taken into account for the implementation of coded excitation for velocity estimation applications. It is worth mentioning here as well, as a conclusion of this section, that although specific attention was paid to CFI applications, the analysis of the sensitivity/axial resolution performed applies in general to incoherent scattering situations, and some of the results could easily be applied to other imaging modalities, like power colour imaging, for instance. The next section reviews the results concerning potential improvements in statistical performance, and concludes on the choice of a strategy of estimation with coded excitation.

7.2 Improvement in statistical performance and choice of a velocity estimation strategy with coded excitation

In line with the objectives of this thesis, the potential improvements in the statistical performance of velocity estimators with the use of coded excitation were also studied. The importance of the statistical performance was emphasised in the introduction chapter (Chapter 1) in relation to providing reliable quantitative values for good diagnosis. This may even become more important in the future as new advanced applications rely on accurate velocity or displacement estimates to infer more complex parameters (for instance strain, strain rate or even wall shear stress in arteries). If these estimates are not reliable, these new methods may suffer from a lack of reproducibility. A broad classification of velocity estimators was made in this thesis as phase shift based narrowband estimators and time-shift based wideband estimators.

The possibility of using coded waveforms with the long used, computationally efficient 1D autocorrelator was demonstrated first in Chapter 4 with simulations and then experimentally in Chapter 6. A theoretical expression was first proposed for the analysis of the performance of the 1D autocorrelator, which was adapted from previous works [79, 74, 11]. Some limitations were pointed out in the use of narrowband estimators with coded excitation. First, due to the narrowband approximation, the performance of these estimators in medium SNR conditions (15 dB) is dominated by the bandwidth of the transmitted pulse (the more narrowband, the better performance). The use of relatively wideband coded waveforms in this case is then detrimental to the statistical performance of the estimator. As noted in the previous section, long narrowband pulses used with this type of estimator already provide a good sensitivity, which means that the margin of improvement in SNR is limited. Moreover, for a packet size above 10, these estimators provide very robust estimates (relative error of 10%) even in degraded SNR (10 dB and less). These aspects were confirmed with a simulation study. The simulations also showed, however, that some potential may exist with low SNR conditions, and with a moderate packet size (below 10 pulse transmit/receive cycles), velocity estimation could then for instance be performed faster with coded excitation (increase in the frame rate), for an equivalent statistical performance and increased axial resolution. In particular, very good results were obtained with the 2D modifided autocorrelation algorithm [11], with a very small packet size (4 pulse transmit/receive cycles). In all these simualtions, however, the hypothesis that an increase in the average transmitted intensity is permitted was made.

The situation is quite different in the case of wideband time-shift based estimation schemes. In this case, the use of wideband coded waveforms is a winning situation both in terms of sensitivity (the margin of improvement in sensitivity over a relatively wideband 4 cycles CF pulse can be realistically of 10 dB as shown in the curves obtained in Chapter 3) and in terms of statistical performance. Chapter 5 has focused in depth on the statistical performance of these estimators, which is quite complex. The analysis framework of the Cramer-Rao Lower Bound (CRLB) is an effective tool to predict the performance of time-shift based estimators in relative high SNR conditions, or more precisely, when a high T_pBSNR' can be achieved (SNR' only depends on the SNR, and was defined in Chapter 5). The product of these values determines if the estimator operate in a low regime of error (CRLB), or in a large error regime with false peak detections. A potential benefit of using coded excitation appears in the situations when false peak detection occurs with conventional pulses, the T_pBSNR' product can then be increased with coded waveforms to operate in a small error regime. This was shown to be interesting in the context of medical ultrasound, when displacements or velocities above the Nyquist limit need to be estimated. The simulations tested velocity estimation with a packet size of 2 and different time shift based estimation schemes. It was shown that the Sum of Absolute Difference algorithm offered very similar performance to the gold standard of crosscorrelation in terms of relative error and bias, provided a specific interpolation scheme is chosen. A simple interpolation algorithm was proposed taking into account the shape of the curve at its minimum (sharp peak with a discontinuity in the first derivative). Due to its simplicity of implementation, this combination of estimator/interpolation method was chosen in both simulations and experiments. The results obtained (in Chapter 5 for the simulations and in Chapter 6, for the experimental data with a stepping rotating phantom) confirmed the potential of coded excitation to estimate displacements above the Nyquist limit with a dramatic improvement in statistical performance compared to conventional pulses.

Finally, to conclude this section, it appears that wideband estimation techniques are the method of preference to be used with coded excitation. Although this result might appear trivial, this an interesting point to make at this stage of the development of coded excitation techniques, as recent papers have discussed implementations of coded excitation systems for CFI, without specifically discussing the type of estimation strategy (and implying the use of the standard 1D autocorrelator). As mentioned in Chapter 5, the uptake of wideband estimation techniques, although superior in terms of performance, has been very slow in scanners for CFI techniques. It is not clear how many scanners use these techniques nowadays. The hypothesised reasons for this situation are the good robustness of the 1D autocorrelator in poor SNR conditions (for a packet size of 10 or more) , and the good sensitivity of narrowband CF pulses, which provide a better sensitivity than wideband waveforms. The hypothesis is made in this conclusion that coded excitation may trigger the shift to wideband excitation techniques for CFI in the coming years, providing a better performance, the possibility to operate beyond the Nyquist limit, increased frame rates (possibility of using only 2 pulse transmit/receive cycles), and an equivalent sensitivity to conventional narrowband methods. This thesis should provide a good framework to understand the motivations and the quantitative trade-offs in this choice of implementation. In terms of technology, this also means that a significant additional constraint is put on the complexity and computational power requirement of scanners, but it is very likely that modern technologies can handle these challenges within reasonable costs.

7.3 Future works and potential applications

In the light of the previous conclusion, future work could focus on comparing conventional CFI implementations, with an implementation based on a wideband estimation technique and coded excitation. A significant effort also has to be made in terms of acoustical dosage, to clearly identify specific practical applications for which headrooms exist to increase the average transmitted intensity. This will clearly influence the potential margins of improvement with coded excitation techniques. The benefits of coded excitation could also be quantified more precisely with a prototype implementation in a scanner. Existing measurement techniques and sensitivity indices [118] developed in the past to benchmark scanners could be very useful in this matter to help comparing systems with conventional excitation and coded excitation. Some specific aspects need also to be studied with a scanner implementation, like the influence of clutter signals, the level of sidelobes required, and frequency dependent attenuation. All these aspects may limit significantly the sensivity/axial resolution trade-off offered by coded excitation in practical situations.

The possibility of estimating displacements and velocities beyond the Nyquist limit may be very interesting to study high velocities, especially when the PRF cannot be increased at high depths. This may also be interesting in some other situations, for which large displacements have to be estimated, like in elastography. In this case, the benefits of using coded excitation have already been demonstrated in a study [113]. More generally, coded excitation could also be applied to increase the centre frequency of operation in some applications (if the centre frequency is doubled the Nyquist limit is then correspondingly halved), this would yield an increased axial resolution (for a constant fractional bandwidth), while coded excitation could compensate for the excess attenuation due to frequency-dependent attenuation, and enable reliable velocity estimation beyond the Nyquist limit. Finally, applications based on synthetic aperture imaging for blood flows could also be very interesting. These techniques suffer from relatively poor SNR because only a few elements from an array transducer are used on transmit, but could in turn increase the frame rates. Promising developments of synthetic aperture techniques for CFI using coded excitation combined with a crosscorrelation estimation technique were demonstrated [48]. Ultimately, fast and accurate 2D images of blood flows using coded excitation seem to be in sight for the future scanners.

Appendix A
List of publications

Phase Domain Velocity Estimation in Medical Ultrasound with Linear Frequency Modulated Chirps: A Simulation Study. Lamboul B., Bennett, M.J., Anderson, T., McDicken, N.W., IEEE Ultrasonics Symposium, p1251-1254, New-York, NY, 28-31 Oct. 2007.

Basic Considerations In the Use of Coded Excitation For Colour Flow Imaging Applications. Lamboul B., Bennett, M.J., Anderson, T., McDicken, N.W., IEEE Trans. Ultrason. Ferr. Freq. Contr., vol.56, no.4, pp 727-737, April 2009.

Bibliography

[1] C.Teirlink, R. Bezemer, C.Kollman, J.Lubbers, P. Hoskins, K. Ramnarine, P.Fish, K. Fredelt, and U. Schaarschmidt, “Development of an example flow test object and comparison of five test objects, constructed in various laboratories,” *Ultrasonics*, vol. 36, pp. 653–660, 1998.

[2] S. Satomura, “Ultrasonic doppler method for the inspection of cardiac functions,” *J. Acoust. Soc. Am*, vol. 29, pp. 1181–1185, 1957.

[3] Z. Kaneko, “First steps in the development of the doppler flowmeter,” *Ultrasound in Med. & Biol.*, vol. 12, no. 3, pp. 187–195, 1986.

[4] R. D. Franklin, W.Schlegel, “Blood flow measured by doppler frequency shift of backscattered ultrasound,” *Science*, vol. 134, pp. 465–11 564, 1961.

[5] W.N.McDicken, G. Sutherland, C. Moran, and L.N.Gordon, “Colour doppler velocity imaging of the myocardium,” *Ultrasound in Med. & Biol.*, vol. 18, pp. 651–654, 1992.

[6] J. D’hooge, E. Konofagou, F. Jamal, A. Heimdal, L. Barrios, B. Bijnens, J. Thoen, F. V. de Werf, G. Sutherland, and P. Suetens, “Two-dimensional ultrasonic strain rate measurement of the human heart in vivo,” *IEEE Transactions on Ultrasonics, Ferroelectrics and Frequency Control*, vol. 49, pp. 281–286, 2002.

[7] J. Ophir, I.Cespedes, H. Ponnekanti, and a. X. Y. Yazdi, “Elastography : a qunatitative method for imaging th elasticity of biological tissues,” *Ultrasonic Imag.*, vol. 13, pp. 111–134, 1991.

[8] P. Peronneau and F. Leger, “Doppler ultrasonic pulsed blood flowmeters,” in *8th International Conference on Medical and Biomedical Engineering*, Chicago, 1969.

[9] D. Baker, “Pulsed ultrasonic doppler blood-flow sensing,” *IEEE Trans. Sonics Ultrason.*, vol. 29, pp. 1181–1185, July 1970.

[10] P. Embree and W. O’Brien, “Pulsed doppler accuracy assessment due to frequency-dependent attenuation and rayleigh scattering error sources,” *IEEE Trans. Biomed.Eng.*, vol. 37, no. 3, pp. 322 – 326, 1990.

[11] T. Loupas, J. Powers, and R. Gill, “An axial velocity estimator for ultrasound blood flow imaging based on a full evaluation of the doppler equation by means of a 2-dimensional autocorrelation approach,” *IEEE Transactions on Ultrasonics, Ferroelectrics and Frequency Control*, vol. 42, pp. 672–688, 1995.

[12] D. Evans and W. McDicken, *Doppler ultrasound: Physics, Instrumentation, and Signal Processing*, 2nd ed. Wiley, 2000.

[13] J. A. Jensen, *Estimation of blood velocities using ultrasound*. Cambridge University Press, 1996.

[14] P. Vaitkus, “A new time-domain narrowband velocity estimation technique for doppler ultrasound imaging,” Ph.D. dissertation, Univ. of Toronto, Toronto, ON, Canada, 1995.

[15] C. Cook and W. Siebert, “The early history of pulse compression radar,” *IEEE Trans. Aerosp., Elec.Syst.*, Nov. 1988.

[16] A. Rihaczek, *Radar signals*. New York: McGraw-Hill, 1969.

[17] R. Chiao and X. Hao, “Coded excitation for diagnostic ultrasound: A system’s developper’s perspective,” *IEEE Trans. Ultrason., Ferroelect.,Freq.Contr.*, vol. 52, no. 2, pp. 160–170, Feb. 2005.

[18] Y. Takeuchi, “An investigation of a spread energy method for medical ultrasound systems-part one: Theory and investigation,” *Ultrasonics*, pp. 175–182, 1979.

[19] ——, “An investigation of a spread energy method for medical ultrasound systems-part two: proposed system and possible problems,” *Ultrasonics*, pp. 219–224, 1979.

[20] M.O’Donnell, “Coded excitation system for improving the penetration of real-time phased-array imaging systems,” *IEEE Transactions on Ultrasonics, Ferroelectrics and Frequency Control*, vol. 39, no. 3, pp. 341 – 351, May 1992.

[21] N. Rao and S. Mehra, “Medical ultrasound imaging using pulse compression,” *Electronics Letters*, vol. 29, no. 8, pp. 649 – 651, 1993.

[22] T. Misaridis, K. Gammelmark, C. Jorgensen, N. Lindberg, A. Thomsen, M. Pedersen, and J.Jensen, “Potential of coded excitation in medical ultrasound imaging,” *Ultrason. Imaging.*, vol. 38, pp. 183–184, 2000.

[23] T. Misaridis and J. Jensen, “Use of modulated excitation signals in medical ultrasound. Part I: Basic concepts and expected benefits,” *IEEE Transactions on Ultrasonics, Ferroelectrics and Frequency Control*, vol. 52, pp. 177–191, 2005.

[24] ——, “Use of modulated excitation signals in medical ultrasound. Part II: Design and performance for medical imaging applications,” *IEEE Transactions on Ultrasonics, Ferroelectrics and Frequency Control*, vol. 52, pp. 192–206, 2005.

[25] M. Pedersen, T.X.Misaridis, and J.A.Jensen, “Clinical evaluation of chirp-coded excitation in medical ulatrsound,” *Ultrasound in Med. & Biol.*, vol. 29, no. 6, pp. 895–905, 2003.

[26] H. Zhao, L. Mo, and S. Gao, “Barker-coded ultrasound color flow imaging: Theoretical and practical design considerations,” *IEEE Trans. Ultrason., Ferroelect.,Freq.Contr.*, vol. 54, no. 2, p. 319, Feb. 2007.

[27] *Standard Guide for Evaluating Characteristics of Ultrasonic Search Units*, ASTM Int’l Std. E1065-99, 2003.

[28] R. Cobbold, *Foundations of Biomedical Ultrasound*. Oxford University Press, Inc., 2007.

[29] F. Kremkau, *Diagnostic Ultrasound : Principles and Instruments*, 6th ed. W.B Saunders Company, 2002.

[30] A.Nowicki, Z.Kliomonda, M. Lewandowski, J.Litniewski, P. Lewin, and I. Trots, “Comparison of sound fields generated by different coded excitations - experimental results,” *Ultrasonics*, vol. 44, pp. 121–129, 2005.

[31] J.Litniewski, A.Nowicki, Z.Kliomonda, and M. Lewandowski, “Sound fields for coded excitations in water and tissues: experimental approach,” *Ultrasonics*, vol. 33, pp. 601–607, 2007.

[32] M. Okujima and S. Ohtsuki, “M-sequence modulated ultrasonic doppler velocity meter for measurement of velocity distribution,” in *18th conf. Jap. Soc. Ultras. Med.*, no. 18-27, Oct. 1970.

[33] ——, “An example of velocity distribution of the heart by using m-sequence modulated ultrasonic doppler velocity meter,” in *18th conf. Jap. Soc. Ultras. Med.*, no. 18-28, Oct. 1970, in Japan.

[34] S. Ohtsuki and M. Okujima, “Ultrasonic doppler velocity meter by m-sequence modulation method,” *J.Acoust. Soc.Japan*, vol. 29, pp. 347–355, 1973, in Japan.

[35] V. L. Newhouse and P. J. Bendick, “Analysis of random signal blood flow measurement,” in *IEEE Ultrasonics Symp. Proc.*, 1973, pp. 94–97.

[36] P. J. Bendick and V. L. Newhouse, “Ultrasonic random-signal flow measurement system,” *J.Acoust.Soc.Am.*, vol. 56, pp. 860–865–36, Sept. 1974.

[37] C. Jethwa, M. Kaveh, G.Cooper, and F. Sagio, “Blood flow measurements using ultrasonic pulsed random signal doppler system,” *IEEE Trans. Sonics Ultrason.*, vol. 22, pp. 1–11, Jan 1975.

[38] A. Hoeks, R. Reneman, and P. A. Peronneau, “A multigate pulsed doppler system with serial data processing.” *IEEE Trans. Son. Ultrason.*, vol. SU-28, pp. 242–247, 1981.

[39] C. Kasai, K.Namekawa, A. Koyano, and R. Omoto, “Real-time two-dimensional blood flow imaging using an autocorrelation technique,” *IEEE Transactions on Sonics and Ultrasonics*, vol. 32, pp. 458–463, 1985.

[40] D. J. Cathignol, C. Fourcade, and J. Y. Chapelon, “Transcutaneous blood flow measurements using pseudorandom noise doppler system,” *IEEE Trans. Biomed. Eng.*, pp. 30–36, 1980.

[41] D. J. Cathignol, “Signal-to-clutter ratio in pseudo random doppler flowmeter,” *Ultrasonic Imaging*, pp. 272–284, 1986.

[42] K. McCarty and J. Woodcock, “Frequency modulated ultrasonic doppler flowmeter,” *Med. Biolog.Eng.*, vol. 13, pp. 59–64, 1975.

[43] J. E. Wilhjelm and P. C. Perdersen, “Target velocity estimation with fm and pw echo ranging doppler systems. part i: Signal analysis,” *IEEE Trans. Ultrason. Ferroelect. Freq. Contr.*, vol. 40, pp. 366–372, 1993.

[44] ——, “Target velocity estimation with fm and pw echo ranging doppler systems. part ii: System analysis,” *IEEE Trans. Ultrason. Ferroelect. Freq. Contr.*, vol. 40, pp. 373–380, 1993.

[45] D. Muzilla, R. Chiao, and A. Hall, “Method and apparatus for color flow imaging using coded exciation with single codes,” U.S Patent 5,938,611, 1999.

[46] A. Hall, R. Chiao, and D. Muzilla, "Method and apparatus for color flow imaging using golay-coded excitation on transmit and pulse compression on receive," U.S Patent 6,095,977, 2000.

[47] L. Y. L. Mo, T.-L. Ji, C. Chou, D. Napolitano, G. McLaughin, and D.DeBusschere, "Zone-based color flow imaging," *Proc. IEEE Ultrason. Symp.*, pp. 29–32, Oct. 2004.

[48] J. Jensen and S. I. Nikolov, "Directional synthetic aperture flow imaging," *IEEE Transactions on Ultrasonics, Ferroelectrics and Frequency Control*, vol. 51, no. 9, pp. 1107–1117, 2004.

[49] J. Cowe, J. Gittins, and D. H. Evans, "Coded excitation in tcd ultrasound system to improve axial resolution," *Ultrasound in Med. & Biol.*, vol. 33, no. 8, pp. 1296–1308, Aug. 2007.

[50] ——, "Improving performance of pulse compression in a doppler ultrasound system using amplitude modulation chirps and wiener filtering," *Ultrasound in Med. & Biol.*, vol. 34, no. 2, pp. 326–333, Feb. 2008.

[51] R. Chiao, "Method and apparatus for color flow imaging using golay-codes," U.S Patent 6,312,384, 2001.

[52] L.-L. Mo and R. Cobbold, "A unified approach to modelling the backscattered doppler ultrasound from blood," *IEEE Trans. Biomed. Eng.*, vol. 39, pp. 650–661, 1992.

[53] L. Mo and S. Cobbold, "A stochastic model of the backscattered doppler ultrasound from blood," *IEEE Trans. Biomed. Eng.*, vol. 33, no. 1, pp. 20–27, Jan. 1986.

[54] K. Ferrara and V. Algazi, "A statistical analysis of the received signal from blood during laminar flow," *IEEE Trans. Ultrason., Ferroelect.,Freq.Contr.*, vol. 41, no. 2, 1994.

[55] B. Angeslen, "A theoretical study of the scattering of ultrasound from blood," *IEEE Trans. Biomed. Eng.*, vol. BME-27, no. 2, pp. 61–67, Feb. 1980.

[56] H. Torp, K. Kristoffersen, and B. A. J. Angelsen, "Autocorrelation techniques in color flow imaging: Signal model and statistical properties of the autocorrelation estimates," *IEEE Trans. Ultrason., Ferroelect.,Freq.Contr.*, vol. 41, no. 5, pp. 604–612, Sept. 1994.

[57] K. Kristoffersen, “Optimal receiver filtering in pulsed doppler ultrasound blood velocity measurements,” *IEEE Trans. Ultrason., Ferroelect.,Freq.Contr.*, vol. 33, pp. 51–58, Jan 1986.

[58] S.-W. Huang and P.-C. Li, “Arbitrary waveform code excitation using bipolar square wave pulsers in medical ultrasound,” *IEEE Transactions on Ultrasonics, Ferroelectrics and Frequency Control*, vol. 53, no. 1, pp. 106–116, 2006.

[59] P.-C. Li, E. Ebbini, and M. O’Donnell, “A new filter design technique for coded excitation systems,” *IEEE Transactions on Ultrasonics, Ferroelectrics and Frequency Control*, vol. 39, no. 6, pp. 805–821, Nov. 1992.

[60] L. Welch and M. Fox, “Practical spread spectrum pulse compression for ultrasonic tissue imaging,” *IEEE Transactions on Ultrasonics, Ferroelectrics and Frequency Control*, vol. 45, no. 2, pp. 349–355, March 1998.

[61] Y. Wang, K. Metzger, D. Stephens, G. Williams, S. Brownlie, and M. O’Donnell, “Coded excitation with spectrum inversion (cexsi) for ultrasound array imaging,” *IEEE Transactions on Ultrasonics, Ferroelectrics and Frequency Control*, vol. 50, no. 7, pp. 805–821, 2003.

[62] S. Treitel and E. Robinson, “The design of high resolution digital filters,” *IEEE Trans. Geosci. Electron.*, vol. 4, no. 1, pp. 25–38, 1966.

[63] M. Ackroyd and F. Ghani, “Optimum mismatched filters for sidelobes suppression,” *IEEE Trans. Aerops. Electron. Syst.*, vol. 9, no. 2, pp. 214–218, 1972.

[64] C. Cook and M. Bernfeld, *Radar signals*. Boston: Artech House, 1993.

[65] T. Misaridis and J. Jensen, “An effective coded excitation scheme based on a predistorted fm signal and an optimized digital filter,” *IEEE Ultrason. Symp.*, pp. 1589–1593, 1999.

[66] K. Eck, R. Schwann, A. Brenner, and T. Noll, “Depth-dependent mismatched filtering using ultrasonic attenuation as a filter design parameter,” *Proc. IEEE Ultrason. Symposium*, pp. 1639–1644, 1998.

[67] P. Embree and W. O’Brien, “Volumetric blood flow via time-domain correlation: Experimental verification,” *IEEE Transactions on Ultrasonics, Ferroelectrics and Frequency Control*, vol. 37, no. 2, pp. 176 – 189, 1990.

[68] S. Holland, S. Orphanoudakis, and C. Jaffe, “Frequency-dependent attenuation effects in pulsed doppler ultrasound: Experimental results,” *IEEE Trans. Biomed Eng.*, vol. BME-31, no. 9, pp. 626–631, Sept. 1984.

[69] A. Papoulis, *Probability, Random Variables and Stochastic Processes*, 3rd ed. McGraw-Hill, 1991.

[70] D.Sirmans and B.Bumgarner, “Numerical comparison of five mean frequency estimators,” *J. of Appl. Meteorology*, vol. 14, p. 991, 1975.

[71] P. Grandchamp, “A novel pulsed directional doppler velocimeter: The phase detection profilometer,” in *Proc. 2nd Eur. Congr. Ultrasonics. Med.* Amsterdam, the Netherlands: Exerpta Medica, 1975.

[72] M.Brandestini, “Applications of the phase detection principle in a transcutaneous velocity profilometer,” in *Proc. 2nd Eur. Congr. Ultrasonics. Med.* Amsterdam, the Netherlands: Exerpta Medica, 1975.

[73] D. Zrnic, “Spectral moment estimates from correlated pulse pairs,” *IEEE Trans. Aerosp. Elec. Sys.*, vol. AES-13, no. 4, pp. 344–354, July 1977.

[74] ——, “Estimation of spectral moments for weather echoes,” *IEEE Trans. Geosc. Elec.*, vol. GE-17, no. 4, pp. 113–128, Oct. 1979.

[75] P. Vaitkus and S. Cobbold, “A new time-domain narrowband velocity estimation technique for doppler ultrasound flow imaging.part i: Theory,” *IEEE Trans. Ultrason., Ferroelect.,Freq.Contr.*, vol. 45, no. 4, pp. 939–954, July 1998.

[76] P. J. Brands, A. P. Hoeks, L. A. Ledoux, and R. S. Reneman, “A radio frequency domain complex cross-correlation model to estimate blood flow velocity and tissue motion by means of ultrasound,” *Ultrasound Med Biol*, vol. 23, pp. 911–920, 1997.

[77] K. Kristoffersen, “Time-domain estimation of the center frequency and spread of doppler spectra in diagnostic ultrasound,” *IEEE Trans. Ultrason., Ferroelect.,Freq.Contr.*, vol. 35, no. 6, Nov. 1988.

[78] K. K. H. Torp and B. A. J. Angelsen, “On the joint probability density function for the autocorrelation estimates in ultrasound color flow imaging,” *IEEE Trans. Ultrason., Ferroelect.,Freq.Contr.*, vol. 42, no. 5, pp. 899–906, Sept. 1995.

[79] K. Miller and M. Rochwarger, “A covariance approach to spectral moment estimation,” *IEEE Transactions on Information Theory*, vol. 18, no. 5, pp. 588–596, September 1972.

[80] T.Berger and H. Groginsky, “Estimation of the spectral moments of pulse trains,” in *Int. Conf. on Information Theory*, Tel Aviv, Israel, 1973.

[81] D. Dotti, E. Gatti, and V. Svelto, “Blood flow measurements by ultrasound correlation techniques,” *Energia Nucleare*, vol. 23, pp. 571–575, 1976.

[82] J. Dickinson and C. Hill, “Measurement of soft tissue motion using correlation between a-scans.” *Ultrasound Med. Biol.*, vol. 8, pp. 263–271, 1982.

[83] O. Bonnefous and P. Pesque, “Time domain formulation of pulse doppler ultrasound and blood velocity estimation by cross-correlation,” *Ultrasonic Imaging*, vol. 8, pp. 73–85, 1986.

[84] O. Bonnefous, “Statistical and time correlation processes applied to velocity measurement,” in *Proc. IEEE*, vol. 75, no. 2, 1989, pp. 236–255.

[85] I. Hein, J. Chen, W. Jenkins, and W.D.O’Brien, “A real-time ultrasound time-domain correlation blood flowmeter: Part i-theory and design,” *IEEE Trans. Ultrason., Ferroelect.,Freq.Contr.*, vol. 41, no. 6, pp. 768–775, 1993.

[86] ——, “A real-time ultrasound time-domain correlation blood flowmeter: Part ii-performance and experimental verification,” *IEEE Trans. Ultrason., Ferroelect.,Freq.Contr.*, vol. 41, no. 6, pp. 776–785, 1993.

[87] H.Torp and K.Kristoffersen, “Comparison between cross-correlation and autocorrelation technique in color flow imaging,” in *Proc. IEEE*, 1993, pp. 1039–1042.

[88] A. Hoeks, T. Arts, P. Brands, and R.S.Reneman, “Comparison of the rf crosscorrelation technique and doppler autocorrelation technique to estimate the mean velocity of simulated ultrasound signals,” *Ultrasound in Med. and Biol.*, vol. 19, no. 9, pp. 727–740, June 1993.

[89] G. Pinton, J. Dahl, and G. E. Trahey, “Rapid tracking of small displacments eith ultrasound,” *IEEE Trans. Ultrason., Ferroelect.,Freq.Contr.*, vol. 53, no. 6, pp. 1103–1117, June 2006.

[90] P. M. de Jong, T. Arts, A. Hoeks, and R. Reneman, "Determination of tissue motion velocity by correlation interpolation of pulsed ultrasonic echo signals," *Ultrason. Imaging*, vol. 12, pp. 84–98, 1990.

[91] ——, "Experimental evaluation of the correlation interpolation technique to measure regional tissue velocity," *Ultrason. Imaging*, vol. 13, pp. 145–161, 1991.

[92] S. Langeland, J. D'hooge, T. Claessens, P. Claus, P. Verdonck, P. Suetens, G. Sutherland, and B.Bijnens, "RF-based two-dimensional cardiac strain estimation: a validation study in a tissue-mimicking phantom," *IEEE Transactions on Ultrasonics, Ferroelectrics and Frequency Control*, vol. 51, pp. 1537–1546, 2004.

[93] A. Fertner and A. SjÃűlund, "Comparison of various time delay estimation methods by computer simulations," *IEEE Trans. Acoust., Speech, Sig. Proc.*, vol. ASSP-34, no. 5, pp. 1329–1330, 1986.

[94] F. Viola and W. Walker, "A comparison of time-delay estimators in medical ultrasound," *IEEE Trans. Ultrason., Ferroelect.,Freq.Contr.*, vol. 50, no. 4, pp. 392–401, 2003.

[95] S. Langeland, J. D'hooge, H. Torp, B. Bijnens, and P. Suetens, "Comparison of time-domain displacement estimators for two-dimensional rf tracking," *Ultrasound Med Biol*, vol. 29, pp. 1177–1186, 2003.

[96] W. Walker and G. Trahey, "A fundamental limit on delay estimation using partially correlated speckle signals," *IEEE Transactions on Ultrasonics, Ferroelectrics and Frequency Control*, vol. 42, pp. 301–308, 1995.

[97] R. Moddemeijer, "On the determination of position of extrema of sampled correlators," *IEEE Trans. Signal Processing*, vol. 39, pp. 217–219, 1991.

[98] G. Carter, "Coherence and time delay estimation," in *Proc. IEEE*, vol. 75, no. 2, 1987, pp. 236–255.

[99] A.M.Quazi, "Fundamental limitations in passive time delay estimation- part ii: Wideband systems," *IEEE Trans. Acoust., Speech, Sig. Proc.*, vol. ASSP-29, no. 3, pp. 527–533, June 1981.

[100] M.Azaria and D.Hertz, "Time delay etsimation by generalized cross correlation methods," *IEEE Trans. Acoust., Speech, Sig. Proc.*, vol. ASSP-32, no. 2, pp. 280–285, 1984.

[101] A. Weiss and E.Weinstein, “Fundamental limitations in passive time delay estimation-part i: Narrow-band systems,” *IEEE Trans. Acoust., Speech, Sig. Proc.*, vol. ASSP-31, no. 2, pp. 472–486, April 1983.

[102] ——, “Fundamental limitations in passive time delay estimation- part ii: Wide-band systems,” *IEEE Trans. Acoust., Speech, Sig. Proc.*, vol. ASSP-32, no. 2, pp. 1064–1078, Oct. 1984.

[103] G. S. G. Jacovitti, “Discrete time techniques for time delay estimation,” *IEEE Trans. Sig. Proc.*, 1993.

[104] S. Foster, P. Embree, and W. O’Brian, “Flow velocity profile via time-domain correlation:error analysis and computer simulation,” *IEEE Transactions on Ultrasonics, Ferroelectrics and Frequency Control*, vol. 37, no. 2, pp. 164 – 175, 1990.

[105] J. Bendat and A. Piersol, *Random Data: Analysis and Measurement Procedures*, 2nd ed. Wiley: Chichester, 1986.

[106] I. Cespedes, J. Ophir, and S. K. Alam, “The combined effect of signal decorrelation and random noise on the variance of time delay estimation,” *IEEE Transactions on Ultrasonics, Ferroelectrics and Frequency Control*, vol. 44, pp. 220–225, 1997.

[107] J. A. Jensen, “Range/velocity limitations for time-domain blood velocity estimation,” *Ultrasound Med Biol*, vol. 19, pp. 741–749, 1993.

[108] J. Ianniello, “Time delay estimation via cross-correlation in the presence of large estimation errors,” *IEEE Trans. Acoust., Speech, Sig. Proc.*, vol. ASSP-30, no. 6, pp. 998–1003, 1982.

[109] T. Varghese and J. Ophir, “A theoretical framework for performance characterization of elastography: The strain filter,” *IEEE Trans. Ultrason., Ferroelect.,Freq.Contr.*, vol. 44, no. 1, Jan 1997.

[110] I. Cespedes, Y. Huang, J. Ophir, , and S. Pratt, “Method for estimation of subsample time delays of digitized echo signals,” *Ultrason. Imaging*, vol. 17, pp. 142–171, 1995.

[111] X.Lai and H.Torp, “Interpolation methods for time-delay estimation using cross-correlation method for blood velocity,” *IEEE Transactions on Ultrasonics, Ferroelectrics and Frequency Control*, vol. 46, pp. 277–290, 1999.

[112] S. Alam and J. Ophir, “The effect of nonlinear signal transformations on bias errors in elastography,” *IEEE Trans. Ultrason., Ferroelect., Freq.Contr.*, vol. 47, no. 1, Jan 2000.

[113] J. Liu and M. F. Insana, “Coded pulse excitation for ultrasonic strain imaging,” *IEEE Transactions on Ultrasonics, Ferroelectrics and Frequency Control*, vol. 52, pp. 231–240, 2005.

[114] P.R.Hoskins, “Simulation and validation of arterial ultrasound imaging and blood flow,” *Ultrasound in Med. and Biol.*, vol. 34, no. 5, pp. 673–717, 2008.

[115] A. Fleming, W. N. McDicken, G. Sutherland, and P. Hoskins, “Asssessment of colour doppler tissue imaging using test-phantoms,” *Ultrasound in Med. and Biol.*, vol. 20, no. 9, pp. 937–7951, 1994.

[116] K.Myitake, M.Yamagishi, N.Takaneda, M.Uematus, N. Yamazaki, Y. Mine, A. Sano, and M.Hirama, “New method for evaluating left ventricular wall motion by color-coded tissue doppler imaging: in-vitro and in-vivo studies,” *J. Am. Coll. Cardiol*, vol. 25, no. 3, pp. 717–724, 1995.

[117] M. Bennett, S.McLauglin, T. Anderson, and W.N.McDicken, “Error analysis of ultrasonic tissue doppler velocity estimation techniques for quantification of velocity and strain,” *Ultrasound in Med and Biol.*, vol. 33, no. 1, pp. 74–81, 2007.

[118] J. Browne, A.J.Watson, P. Hoskins, and A. Elliott, “Validation of as sensitivity performance index test protocol and evaluation of colour doppler sensitivity for a range of ultrasound scanners.” *Ultrasound in Med and Biol.*, vol. 30, no. 11, pp. 1475–1483, 2004.